

Università degli Studi di Bologna

FACOLTÀ DI INGEGNERIA

Dottorato di Ricerca in Ingegneria Elettronica,
Informatica e delle Telecomunicazioni

XVII Ciclo

**CMOS Lab-on-a-Chip Devices for
Individual Cell Biology**

Tesi di Dottorato di

Aldo Romani

Relatore

Chiar. mo Prof. **Roberto Guerrieri**

Coordinatore

Chiar. mo Prof. **Paolo Bassi**

Anno Accademico 2003-2004

Contents

Contents	I
Introduction	1
1 Lab-on-a-Chip Devices	3
1.1 Introduction	3
1.2 Why smaller is better (even in bioanalysis)	4
1.3 The pursuit of functional integration	7
1.4 What microelectronics has to offer	8
1.4.1 Advantages of silicon	9
1.4.2 Limitations	10
1.4.3 The key building blocks	11
1.5 Challenges	14
1.6 The state of the art	15
1.6.1 Biosensing in lab-on-a-chip devices	17
1.7 The MeDICS project	27
2 A CMOS Chip for Single Cell Biology	29
2.1 Why integrating sensing and actuation in a lab-on-a-chip . .	30
2.2 An introduction to dielectrophoresis	30
2.3 Dielectrophoresis and living cells	33
2.4 Design objectives and specifications	36
2.4.1 Design approach	36
2.4.2 Examples of applications	39
2.4.3 Design constraints and specifications	40

Contents

2.5	Chip architecture	42
2.5.1	Micro-site circuit with optical sensors	45
2.5.2	Micro-site circuit with capacitive sensors	46
2.5.3	Read-out circuit	50
2.6	Preliminary test results	52
2.7	Summary	60
3	A Programmable Architecture for Lab-on-a-chip Control	63
3.1	System specifications	64
3.2	Design approach	66
3.3	System architecture description	68
3.3.1	The XiRisc microprocessor	70
3.3.2	The Programmable Waveform Generator	71
3.3.3	The Bridge	72
3.3.4	Software	72
3.4	System implementation	74
3.5	Summary	76
4	Experimental Results	77
4.1	Experimental setup	78
4.2	Biological validation of the device	79
4.2.1	Description of the particles	79
4.2.2	Manipulation of blood cells	81
4.2.3	Effect of DEP on cell viability and proliferation	83
4.2.4	Characterization of motion	83
4.2.5	Routing of particles	85
4.3	Optical sensing	86
4.3.1	Optical detection of bioparticles	86
4.3.2	Spectral response of the photodiodes	86
4.4	Capacitive Sensing	90
4.4.1	Equivalent circuit model for capacitive sensing	91
4.4.2	Characterization of particles	97
4.4.3	Effect of the sampling time	99
4.4.4	Fitting experimental data	100

4.4.5	Matching data and models	101
4.5	Quantitation of particles	103
4.6	Noise analysis	105
4.6.1	Noise on optical sensors	107
4.6.2	Noise on capacitive sensors	107
4.6.3	Fixed pattern noise	109
4.7	Analysis of sensing limits	110
	Conclusions	116
	List of Figures	119
	List of Tables	125
	Bibliography	126

Contents

Introduction

Biological and pharmaceutical research are experiencing significant advances thanks to the benefits introduced by the integration of complex functionalities offered by silicon technology. Geometry scaling, the introduction of integrated smart sensors and the evolution of microfabrication techniques are pushing the so called “lab-on-a-chip” technology towards implementations of highly integrated microsystems. Driven by the need of cost and size reduction, for example for disposable biomedical smart devices, this technology is making feasible the replacement of bulky and expensive traditional laboratory equipment with cheap, smaller, faster microsystems. It is our belief that CMOS technology has the potential to integrate such low-cost complex devices composed of sensors, actuators and data processing circuits.

This thesis describes the design, testing and validation phases of a CMOS lab-on-a-chip prototype able to individually manipulate and detect living cells by exploiting the superficial electric field generated by the device. This perspective may open new fields in individual cell biology and rare cell population analysis. The project was carried out in an international and multidisciplinary research team composed of both academic and industrial members. In addition, the activity focused on different topics, ranging from silicon and system design to software development, from experimental prototype characterization to biological experiments.

In the first chapter a review of current technologies in the field of CMOS lab-on-a-chip devices for cell biology applications will introduce the reader to the actual state-of-the-art in this area. The following chapters will describe in detail the implemented device, system and technology. In

Introduction

the last chapter, the main results of the experimental activity will be presented and discussed, with special care to cell manipulation and detection by means of embedded sensors.

Chapter 1

Lab-on-a-Chip Devices

1.1 Introduction

Analytical methods are critical to a wide range of industry sectors, from pharmaceutical research to the agrifood business, from environmental control to diagnostics, to name a few. In the last ten years, the field of laboratory methods for biology and chemistry has been shaken by a revolution which is reshaping the way research and analyses are carried out. This revolution is based on the miniaturization and integration of analytical protocols.

Micro Total Analysis Systems (μ TAS) were envisioned in the late 80's [3], as miniaturized, highly integrated chemical analysis systems. The early efforts regarded the microfluidic problems related to the motion of liquid samples in micromachined channels, which built on the experience of capillary electrophoresis. In the late 90's, the advent of DNA microarrays, propelled by genomic research captured the attention of researchers and investors alike.

Although the field was generally indicated as that of *biochips*, the word "lab-on-a-chip" entered the jargon to differentiate between passive microarrays and micro analytical systems sporting some degree of integration, programmability, or microfluidic capabilities. Many technologies for fluid motion, DNA amplification, detection and other analytical techniques have been miniaturized. Although the current systems are useful

under many aspects, as they improve the performance of analytical procedures, there has been a notable lack from the stand point of functional integration, intended as the possibility of combining the analytical protocols. The purpose of this thesis is to explore the possibilities for bioanalysis offered by CMOS platforms, and to evaluate the degree of integration of lab-on-a-chip devices in such technology.

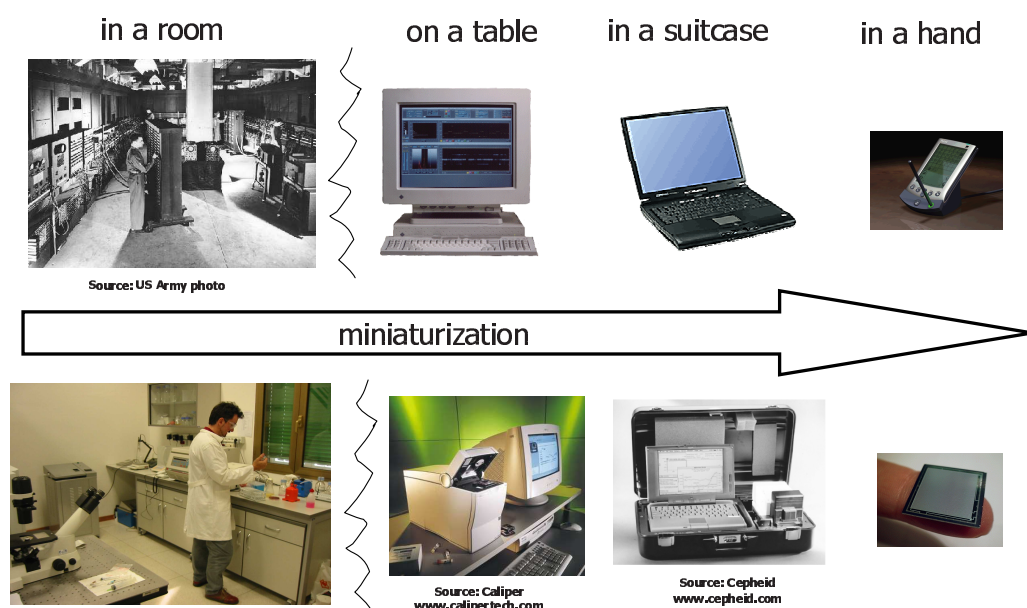


Figure 1.1: Lab-on-a-chip: a parallel with computer systems evolution

1.2 Why smaller is better (even in bioanalysis)

The advantages of miniaturization in bioanalysis are mainly bound to the following points.

Parallelism. As it has been learnt from the microelectronic industry, miniaturization can lead to massive parallelism. For decades, test tubes, small flasks of glass with a volume of a few mL, have been the standard tools for handling biochemical samples. The need to carry out

1.2. Why smaller is better (even in bioanalysis)

reactions in a parallel fashion, e.g. for screening compounds of potential pharmaceutical activities, has progressively led to the development of standard plates with an increasing number of smaller and smaller wells, as a substitute for the test tubes.

The major driving force for miniaturization has been the need to increase parallelism, in the rush to discover genomic information. In this area, two kinds of techniques have been developed, to arrange a large number of test sites on a glass slide. The first approach has been direct parallel synthesis of oligonucleotides, through lithographic techniques borrowed from the microelectronic industry. This approach [4], allows the synthesis of more than 500k DNA probes on a single chip. The superior density of this technique is offset by the fact that mask level synthesis of the probes brings in a high overhead for chips fabrication and long turnaround times. A second, more flexible approach, albeit with lower densities, is that of spotted arrays. In this case, the probes are printed on the slides by ink-jet or other similar techniques, so that researchers can quickly build an array according to their own interests. A drop of sample including the DNA to be analyzed is then applied to the chip and incubated, whereby DNA molecules bind to the probes on the chip surface with matching oligonucleotide sequence (hybridization). Detecting, by fluorescent labels attached to the analyte, the molecules at a given position, allows one to determine the sequence of the unknown analyte.

Reduced reagent consumption. Another major benefit of miniaturization is the cost reduction for screening the compound libraries, which pharmaceutical company systematically test to establish their potential activity in a given cell-biology problem. These compounds are often very expensive and reducing the volume of the reaction vessel of orders of magnitude was immediately perceived as an important benefit.

Speed. It turns out that shrinking dimensions not only can improve the above performance parameters, but it has additional advantages

which are bound to the physics of the experiment itself, when heat or mass transfer are involved. As an example, DNA amplification by Polymerase Chain Reaction (PCR) [5] requires the cycling of the sample through three different temperatures (denaturation at 94°C, annealing at 50-60°C, depending on the primers, and extension at 72°C). In this case, smaller volumes lead to faster heating and cooling cycles, thus shortening the time to accomplish the required number of cycles (20-40), from several hours to few minutes.

Similarly, for miniaturized molecular assays, smaller dimensions help in reducing the incubation time due to the fact that diffusion of molecules on a microscopic scale is achieved in a shorter time. On the other hand, since only laminar flow is possible at very small geometries, mixing should be achieved by diffusion only

Functional Integration. Although the above points are important, the most exciting opportunity from miniaturization will be in functional integration, which will allow one to quickly and cheaply perform complex multi-step analytical protocols, which traditionally require a host of different machines. This will be similar to what microelectronics brought to the computer industry, which evolved from large, expensive mainframes to cheap, ubiquitous personal computers with an exponential increase in computing power at affordable costs. For microelectronics, the reduction in cost and increase in capabilities translated to a pervasive deployment of the technology, which is why today we have electronic devices not only in computers, but also in washing machines, toys, post-cards. So why shouldn't this happen to labs-on-a-chip?

To continue the parallel with computer industry, we can assess where we stand now with a reference to the form factor scale (Fig. 1.1). Traditional analytical techniques could fit in a room (like the early mainframes). The disruptive technology of ICs led to the PC era of desktop systems, which fit on a table. Labs-on-a-chip can be imagined as the ICs equivalent in analytical laboratories. Although some of the

1.3. The pursuit of functional integration

early lab-on-a-chip products currently available are actually bench-top instruments, one cannot say we are already at the PC equivalent stage. The missing key features are functional integration and the general purpose capability.

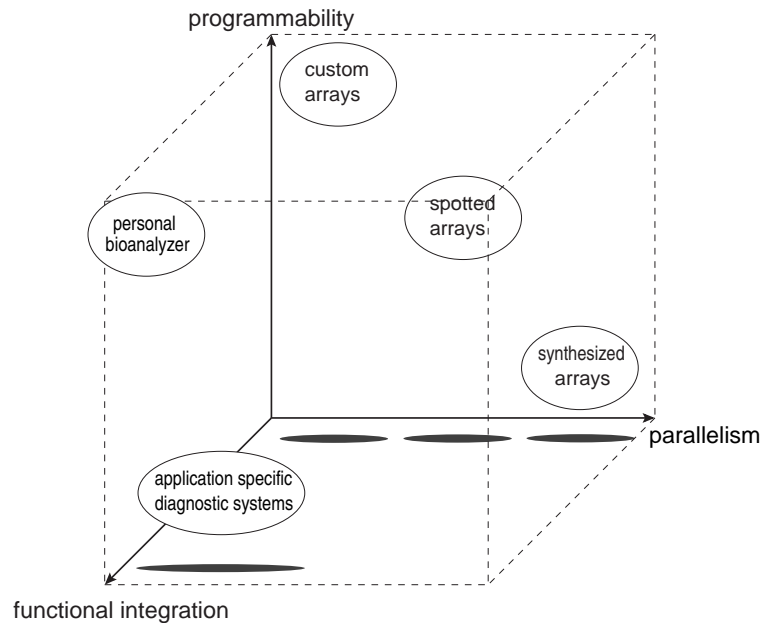


Figure 1.2: The lab-on-a-chip performance cube

1.3 The pursuit of functional integration

The integration of functions into a single programmable system is a goal that has not yet been achieved. The lab-on-a-chip systems developed so far demonstrated superior performance, but this has normally been just a small step of a complete analytical protocol. One of the few exceptions is found in [6], a system originally developed under US-DARPA funding to detect airborne biowarfare agents in the battlefield. That demonstrated an instrument fitting in a suitcase able to detect pathogens within 30 minutes.

Although one of the main drivers for this effort will be again the pharmaceutical research market, great opportunities exist for systems which

could carry out a full analytical protocol, from sample-to-answer, in real-time and at a low cost.

Even for medium-cost systems, a lot of applications exist, which would benefit from the real-time feature afforded by miniaturized microbiological analysis. Just as an example, an antibiotic susceptibility test could allow savings in both drug and hospitalization through a more effective treatment of disease. Prenatal diagnosis is another example. It is known that fetal cells can be found in maternal blood, albeit as few as one per mL of blood [7] (as compared to 10^9 red blood cells and 10^7 white blood cells). Considering the non-negligible miscarriage risks of current practices such as amniocentesis, benefits from a non-invasive test protocol could relax cost constraints.

As biological research emphasis shifts from the decoding of genomic information to the understanding of protein interactions and to the cell-level understanding of biosystems, there is a need for more complete systems which not only can handle molecule, but which can also deal with cells.

Up to now, lab-on-a-chip emphasis has been on molecular analysis. However many analytical protocols require the handling of living cells. As an example, testing of blood, food or water supplies require the measurement of the living microorganisms only, because dead cells, although detectable with DNA analysis, would not be contaminants.

1.4 What microelectronics has to offer

There are a number of materials which are currently being used for labs-on-a-chip. Glass or plastic (e.g. polycarbonate) and polydimethylsiloxane (PDMS) elastomer have been used for microfluidic devices. These are built by microfabrication of a first slide, which is then sealed to a second flat slide, pierced in correspondence of the fluidic I/Os. The main advantage of these materials is low cost and optical transparency.

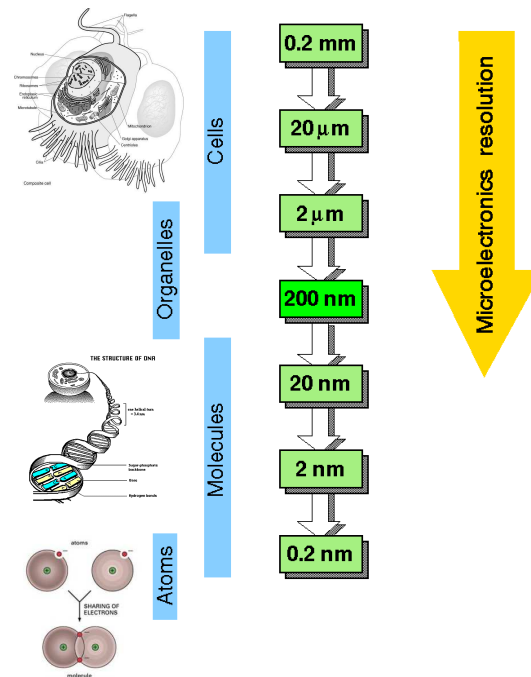


Figure 1.3: Comparison of microelectronics minimum feature sizes and biological characteristic dimensions

1.4.1 Advantages of silicon

Silicon has also been used, but mainly because of its excellent thermal conductivity and, with few notable exceptions, microelectronic potential has remained relatively untapped.

Active circuits. As shown in Fig. 1.3, due to the exponential shrinkage of minimum feature sizes, today it is possible to design complex integrated circuits the size of a cell. This is a key strength, from which further advantages are derived. In fact, this can be used to design complex multiplexing schemes, to create programmable surface electric fields for sample actuation and to embed optical or impedance sensors.

Embedded sensing. Optical, impedance or chemical sensors can be easily integrated, along with signal conditioning circuits.

Embedded actuators. Controlled heating or electric fields can be easily

generated in the sample microchamber for various purposes.

Programmability. The circuits embedded in a CMOS-based lab-on-a-chip allow one to dramatically increase programmability. As an example, the number of I/O needed to directly address an array of electrodes limits its size to few hundreds, in a passive chip. Multiplexing the access like in semiconductor memories allows an increase of 3-5 orders of magnitude.

Established manufacturing technology. The wide availability of micro-electronic technologies from competing foundries means that high-volumes could be reached without substantial investments in production facilities.

Structured design methodologies. Using silicon means that electronic design automation tools can be readily inserted in the design-flow methodology for labs-on-a-chip, although effective interfacing with multi-physics simulation packages is still an unmet need.

1.4.2 Limitations

Besides this, some limitations exist and are summarized below.

Chip size. The cost of active silicon circuits per unit area is much higher than the cost of relatively inexpensive substrates such as glass or plastic. Under these circumstances, the chip area will probably be limited to about 1cm^2 , which is comparably smaller in size, with respect to capillary electrophoresis chips currently used, which can be an order of magnitude larger.

Non transparent substrate. This rules out the possibility of using certain types of microscopes. On the other hand, this should not be a major problem, since under specific conditions embedded sensing may allow to dispose of bulky and expensive external microscopes.

Low voltage supply. Electro-osmotic and capillary electrophoresis techniques used in glass chips require voltage supplies in excess of hundreds or even thousands of volts. Thus, new techniques are needed to replace them with voltages compatible with mainstream microelectronic circuits. As technology scales down, supply voltages get reduced as well. On the other hand, microelectronics offers the possibility of having high electric fields even with moderate voltages, which could then be used to work around the problem. One could deal with this issue by reducing the involved geometries (e.g. dimensions of the microchamber containing the samples to be inspected or manipulated.)

1.4.3 The key building blocks

Many of the key building blocks for labs-on-a-chip have already been demonstrated. While most of them have been implemented on passive substrates, many could be integrated on an active silicon chip.

Fluid handling. Several approaches have been demonstrated for motion of liquids in microchannels. In [8], a thermocapillary pump was implemented on silicon. A droplet of liquid was propelled in a microchannel by differences in surface tension stemming from local heating at the droplet meniscus.

Electro-hydrodynamic pumps, based on traveling-waves orthogonal to thermal gradients in the liquid, constitute another approach for microfabricated pumps without moving parts [9], [10]. However, significant velocities require voltages in excess of 20V.

Another approach to fluid motion is based on the integration of pressure driven pumps. Overlays of micromachined silicon elastomer layers can be used to build microscopic peristaltic pumps [11].

Cell handling. Because cells do not have, in general, an electric charge, the approaches to cell manipulation inside lab-on-a-chip have been based on two main techniques: fluid motion and dielectrophoresis.

Fluid motion has been used in the miniaturization of conventional Fluorescence Activated Cell Sorters (FACS). In [12], cells move in a microchannel flowing with the solution pumped with electro-osmosis. An external detector in correspondence of a T junction is used to divert the flow to either the left or right reservoir according to their fluorescence emission.

Dielectrophoresis (DEP) [13] can be used to move neutral particles, such as cells. When subject to a spatially non-uniform electric field they experience a net force directed towards locations with increasing (pDEP) or decreasing (nDEP) field intensity.

In [14], both pDEP and nDEP are used to displace cells in a microchamber formed between two facing glass chips with elongated electrodes. However, cells in contact with device surfaces tend to stick to them. A solution is to levitate cells while manipulating them. In this case, the use of nDEP is mandatory, since only local minima of the electric field can be established in the suspending medium.

Hence, the use of closed nDEP cages has been proposed. In [15] and [16], 3D structures of electrodes located at the vertexes of a cube are used for this purpose. The main drawback is that an alignment at the micron scale is required to handle single cells.

A microelectronic-friendly technique overcoming the above limitations is the moving-cages approach, first proposed in [24]. A programmable array of electrodes, amenable to standard CMOS fabrication, can be used to create DEP cages which can be moved independently, dragging along the trapped particles without the need for fluid flow (Fig. 1.4). This approach, when combined with integrated impedance sensing as already demonstrated in an up-scaled format [25], will enable the development of elaborated analytical procedures such as separation, counting, and high-throughput screening of compounds at individual-cell level. As a rule of thumb, electrode pitch is best set equal to the cell diameter [26]. Thus, considering for example $10\mu\text{m}$ cells, in a single 1cm^2 chip one could embed up to 1M

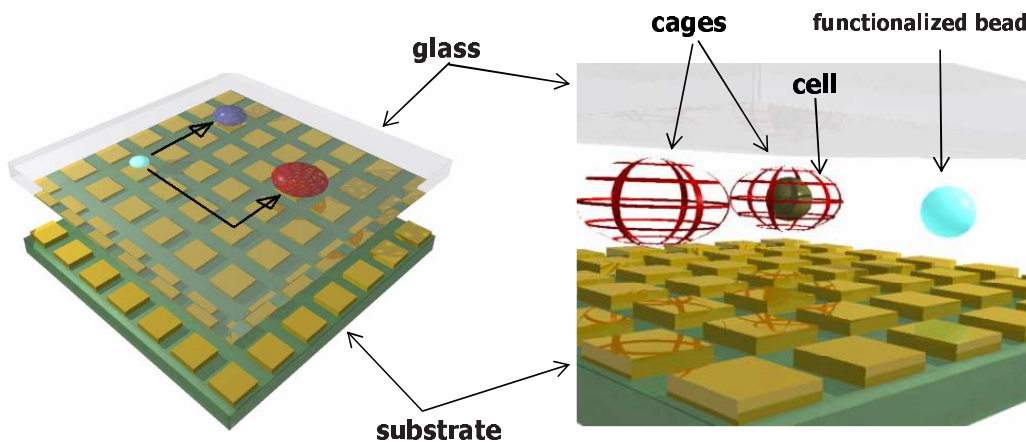


Figure 1.4: Programmable cell-handling device.

electrodes to create more than 100k independent DEP cages.

DNA amplification, handling and detection. As described before, a common tool for analysis is the PCR reaction, which is based on thermal cycling. This can be readily achieved with integrated heaters and thermal sensors [8], [28].

Electronic assembly of DNA microarrays on active silicon chips has been demonstrated by several groups [29], [30]. Since DNA molecules are negatively charged, they can be attracted to positively biased test sites. This approach can be used to both build the array of probes and to accelerate hybridization, shortening the incubation time. In [30], electronics is further leveraged to achieve a stringency control. After hybridization, a repulsive force is applied by negatively biasing the test site, so that only strands which perfectly matches with the local probe are retained. This enables detection of single nucleotide polymorphisms (SNPs), i.e. single base variations which may be associated with certain genetic diseases.

DNA detection. The most common DNA detection technique today is optical detection with external microscopes by fluorescent labeling of

DNA. In order to integrate electronic DNA detection, different approaches have been recently investigated. In [8], radiolabeled DNA is detected by embedded diodes. In [31], DNA probes replacing the gate electrode of a depletion FET have been used for label-free detection of hybridization. In [32], a modified CMOS process with gold electrodes is used for electronic DNA detection mediated by redox cycling.

1.5 Challenges

Despite the remarkable achievements in miniaturization outlined before, the implementation of programmable lab-on-a-chip with a high degree of functional integration is challenged by both technical and business issues.

How small is too small? Depending on applications, the number of cells of interest per unit volume can vary by many orders of magnitude. From this point of view, the trend in miniaturization must cope with the need of maintaining the statistical significance of the sample. As in the example of fetal cells in maternal blood (1 per mL), it is clear that a drop of sample (i.e. few μL) would hardly have any cell of interest. The same holds true for water supply testing tasks.

Possible solutions to these divergent needs will include cascading of coarse grain and fine grain systems built with heterogeneous technologies, such as CMOS, MEMS, plastic, glass etc.

Another reason which will favor heterogeneous systems is functional integration. Not all the building blocks will be available in a single technology or, even if available, other reasons such as cost may favor less integrated solutions.

Beyond the technical aspects, intellectual property (IP) issues will play a role. In fact, the current industrial landscape is characterized by start-ups developing their own proprietary technologies. System integration will either involve joint ventures between the owners of these technologies, either the consolidation of this industry sectors, with emerging players

eating smaller companies with complementary know-how and IP assets, or finally the development of interoperability between the building blocks of the various companies, through the development of standards.

1.6 The state of the art

Many analysis protocols in cell biology need to extract selected samples from cell populations, or consist in isolating specific histotypes, or require to quantitate and count specific individuals. These kinds of analyses are usually carried out by using traditional biological laboratory equipment and conventional techniques and protocols, but new technologies based on miniaturization and strong functional integration are now emerging. The so-called lab-on-a-chip (LOAC) systems, as already discussed in previous sections, greatly take advantage from miniaturization, and potentially integrate in a single chip all the necessary features for a specific task, thus requiring just a drop of sample to carry out the job. This approach would bring great advantages in terms of reduction of sample volumes and thus of processing time and reagent cost. Elements such as actuators, microchannels, heaters, sensors and active circuits can be embedded in a single integrated device.

In this scenario, CMOS technology can play a key role. Active circuits and enhanced routing capabilities can further increase parallelism and functional integration by embedding sensors, signal processing capabilities, and complex control units. Sub-micron resolutions make it now possible to implement complex circuits composed of tens of transistors, including sensors and actuators with sizes comparable with those of cells. Thus, interactions with individual cells can be monitored and controlled by integrating sensors and actuators. For example, in this application field, detection, extraction or stimulation of few selected or individual cells is an essential feature to carry out specific biological analyses such as extracting fetal cells from maternal blood, biopsies, or non-invasive neural cell monitoring.

LOAC technology has been dealing with these issues with several ap-

proaches, like for example with microfabricated fluidic structures, electrochemical reactions [32], or by exploiting physical phenomena such as for example dielectrophoresis (DEP). Among these, DEP is well suitable for integration in electronic devices with standard CMOS technologies, as it will be shown in this thesis [51] or as it was shown for example in [33] or in [34]. Besides manipulation capabilities, the ability of detecting and characterizing cells and microparticles plays a key role in analytical protocols, and in order to pursue an automation of processes, and to carry out complex tasks in an automated way. Integrated detection and the ability of manipulating and displacing the sample within the device let us foresee autonomous LOAC systems. Among biosensors, detecting electrical signals of cells (currents from ion channels through membrane) is another interesting field of application in bioelectronics. In this area important contributions have recently emerged [40], [41]. Cells can be stimulated and their response monitored so as to allow a valuable instrument for researching further comprehension of cellular interactions. Besides this, accurate quantitation or localization of cells or particles could enhance applications like counting cells of a specific type (e.g. red blood cells) in a sample or help isolating rare or different kinds of cells like fetal cells from maternal blood. Thus, one of the actual real challenges is to achieve embedded sensors with single cell resolutions.

CMOS has the potential to exploit well-established industrial processes and foundries, with the advantage of low-cost, stable technologies. Moreover, complex sensing and actuation circuits can be integrated on the same device. The following sub-section will review some state-of-the-art designs of CMOS or *CMOS-friendly* lab-on-a-chip devices, where the *CMOS-friendly* term refers to technologies which are compatible and easily portable onto CMOS.

The shown applications will range from molecular biology (e.g. DNA detection), up to cellular biology (e.g. integrated sensors for living cells). The works will be described and analyzed in view of their application field. A quite exhaustive review of these and other topics is presented in [35]. Anyway, this discussion will focus on two major areas:

- detection of cells or biological particles
- manipulation of cells or biological particles.

1.6.1 Biosensing in lab-on-a-chip devices

For this task, different approaches have been proposed in literature and industry. CMOS technology showed to be a suitable platform for lab-on-a-chip integrated detection. Besides this, other notable techniques show to be implementable in such process.

Integrated DNA detection

For example, in many fields of biotechnology, tools are required to detect the presence or absence of specific DNA sequences in a given sample. The development of DNA microarrays in recent years has opened the way to high parallelism and high throughput [36] [37] [32]. The most widely known applications are genome research and drug development. The realization of fully electronic medium-density DNA sensor array chips [38] [39] is attracting increasing interest for diagnostic purposes. Such electronic approaches avoid expensive optical set-ups used in today's commercially available systems based on optical readout methods; they promise ease of use and robust applicability. However, the status of development of today's electronic systems is lower compared to optical systems.

Recently, a CMOS fully electronic DNA sensor array with 128 sensor positions was presented based on an electrochemical detection principle [32]. From a technological point of view, it was fabricated with an extended CMOS $0.5\mu m$ process, with gold as the highest metal level. There, each sensor pixel consists of a circuit which controls the electrode voltages and provides a 100-fold value of the sensor currents at the pixel output. Analog data transmission within the whole array circuit is required. Using the same detection principle, a DNA sensor array chip with analog-to-digital (A/D) conversion realized within each pixel [42]. This approach

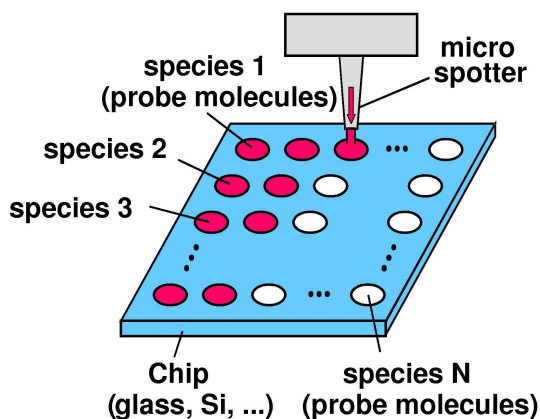


Figure 1.5: Schematic plot of a DNA-microarray chip.

provides a high dynamic range of five decades and is well suited as a robust platform to measure transducer-generated currents within a wide range of applications.

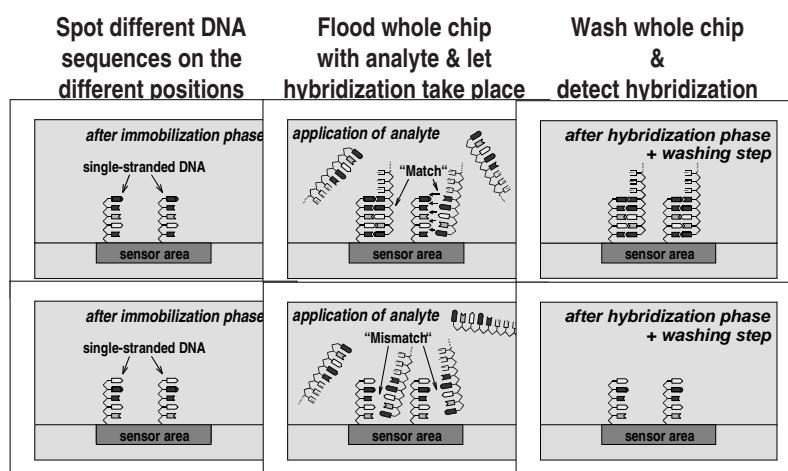


Figure 1.6: Schematic consideration of two test sites.

In general, a DNA microarray chip is a slide made of glass, a polymer

material, silicon, etc. On the surface of such a chip, single-stranded DNA receptor molecules (probes) are immobilized at predefined positions, as shown in Fig. 1.5. These probe molecules consist of different DNA sequences of typically 20 to 40 bases. Whereas a number of different techniques are known to functionalize the chips, in our case off-chip synthesized probe molecules are deposited on the surface of the chips using a microspotter [13].

In Fig. 1.6, two different sites within an array are considered after the immobilization phase. For simplicity, only five bases are drawn in this schematic illustration. Then, the whole chip is flooded with a sample containing the target molecules. In case of complementary DNA sequences of probe and target molecules, their match leads to hybridization. If probe and target molecules mismatch, this chemical binding process does not occur. After a washing step, double-stranded DNA is obtained only at the matching positions. At the mismatch sites single-stranded DNA molecules remain, and the same situation as in the initial case is reached again. Since the receptor molecules are known, the information, whether double- or single-stranded DNA is found at different test sites, reveals the composition of the sample. Thus, the requirement remains to identify the sites with double-stranded DNA. In today's commercially available systems, the target molecules are usually labeled with fluorescence markers molecules and an optical image of the array chip reveals the positions with double-stranded DNA.

The sensors presented in [42] are based on an electrochemical redox-cycling technique. Each sensor site (Fig. 1.7) consists of interdigitated gold electrodes (generator and collector electrode) with width and spacing equal to $1\mu\text{m}$. Probe molecules are immobilized on the gold surface (e.g., by thiol coupling). The target molecules in the sample are tagged by an enzyme label (alkaline phosphatase). After hybridization and washing phases, a chemical substrate (para-aminophenylphosphate) is applied to the chip. At the position with matching DNA strands the enzyme label cleaves the phosphate group and generates an electrochemically active compound (para-aminophenol). Applying simultaneously an oxida-

tion and a reduction potential to the sensor electrodes (V_{gen} and V_{col} , e.g. $+200mV$ and $-200mV$ with respect to the on-chip reference potential), para-aminophenol is oxidized to quinoneimine at the generator electrode, and quinoneimine is reduced to para-aminophenol at the collector electrode. In this way currents are generated at the electrodes (I_{gen} and I_{col}). Since not all particles oxidized at the generator reach the collector electrode, a regulated four electrode system is used. A potentiostat, whose input and output are connected to a reference and to a counter electrode, respectively, provides the difference current to the electrolyte and regulates the potential of the electrolyte to a constant value. The current flow at the sensor electrodes has two contributions, firstly the current initially generated by the enzyme label, and secondly the current of the redox-cycling at the sensor electrodes. Moreover, due to electrochemical artifacts an offset current may contribute to the detection current as well, so that usually the derivatives of the sensor current with respect to the measurement time, $\partial I_{col}/\partial t$ and $\partial I_{col}/\partial t$, are evaluated instead of the absolute values.

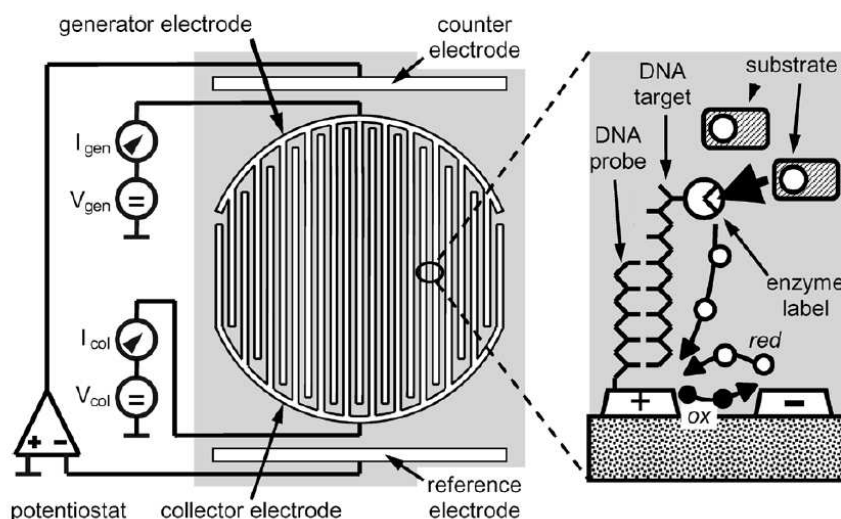


Figure 1.7: Schematic plot of the electrode configuration and of the redox-cycling process.

Recording and stimulation of cell activity

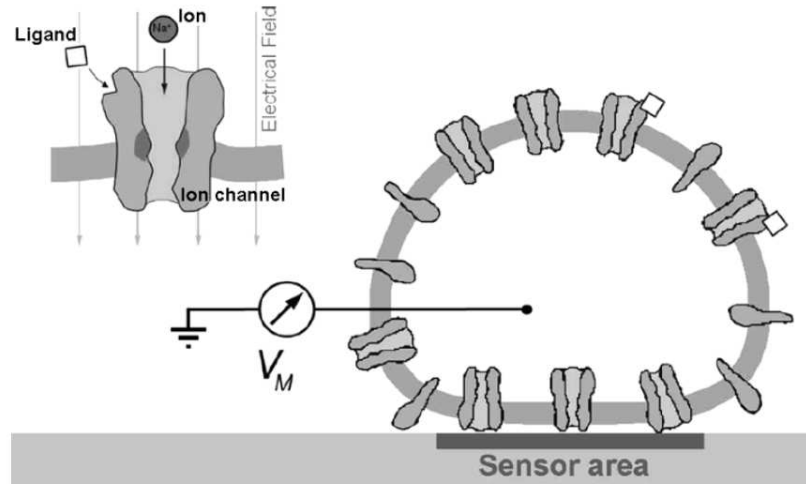


Figure 1.8: Schematic representation of a cell-based sensor

In recent years, increasing knowledge about *in vitro* cell handling and culturing has encouraged a variety of CMOS-based approaches to stimulate and detect electrical activity of biological cells. Ion channels are an important species of proteins as they are responsible for the generation and propagation of electrical signals in biological systems. They reside in the cell membrane, where they control the ionic flux across the cell membrane. The ion permeability of these protein pores can be gated by:

1. the electrical field along the channel
2. the binding of a ligand to the channel protein

Ion channels, therefore, constitute the interface between electrical and biochemical signaling in biological systems. The ion channel of, e.g., neurons are ideally suited for detecting neuro-active substances, as they translate the presence of neuro-active substances into measurable changes of electrical signals. Ion channels, however, have to be embedded into a membrane which is, in the best case, provided by cells to ensure their proper functioning. Figure 1.8 shows the structure of a sensor that make

use of an attached electrogenic cell to provide the desired ion-channels. Such devices are usually called “cell-based biosensors”.

Electrogenic cells such as neurons contain ion channels, which selectively enable the permeation of certain ions such as sodium or potassium. In a transient change of conductivity, the overall ion flux generates an action potential, which is the elementary electrical signal in biological systems. During an action potential, the dc-voltage drop across the cell membrane, which ranges between $-50mV$ to $-70mV$, decreases, and the membrane depolarizes for some milliseconds, after which the intracellular resting potential is reestablished [43]. In neural networks, where neurons are densely packed and interconnected by synapses, the transmembrane currents invoked by action potentials are superimposed with synaptic and extracellular currents. Altogether they generate a transient change in the extracellular potential, the so-called “field potential”.

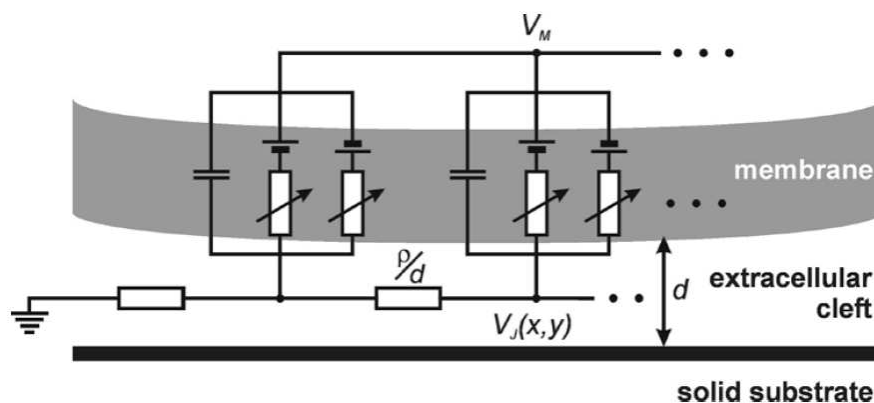


Figure 1.9: Contact model of extracellular recording. The intracellular voltage V_M is represented as voltage V_J in the cleft between cell membrane and substrate.

Cell-based biosensors record current or voltage changes that are induced by the presence of bioactive sample molecules. Electrical activity of single cells can be recorded by glass pipettes that are used to establish an intracellular contact by disrupting the cell membrane. The patch clamp technique is considered to be the gold standard of intracellular recording. A patch pipette forms a tight seal with the cell membrane allowing for

low-resistance probing at low leakage currents. A huge effort is required to mechanically stabilize this delicate contact, so that the number of cells which can be simultaneously recorded from is limited.

The electrical activity of cells can also be recorded without disrupting their membranes. In the following, the principle of extracellular recording is outlined for single cells.

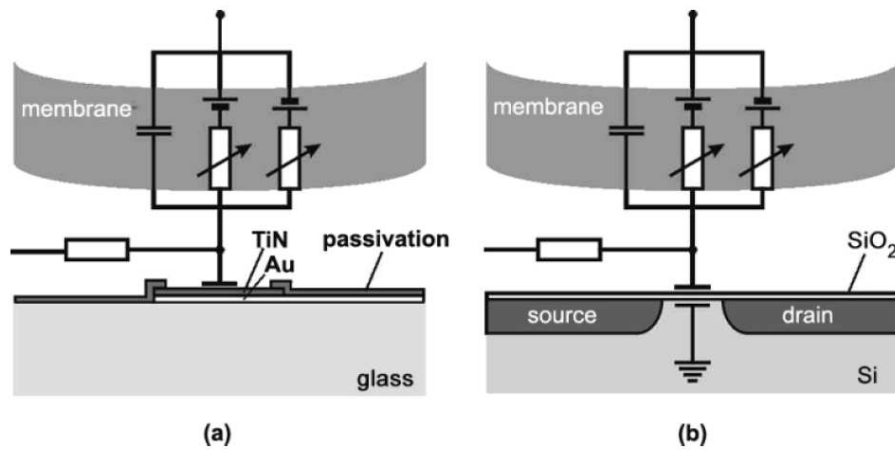


Figure 1.10: Devices for extracellular recording. (a) Metal electrode. (b) Open field-effect transistor.

As shown in Fig. 1.9, the intracellular potential V_M of a surface-attached cell is represented in the cleft as the extracellular potential V_J between the membrane and the supporting surface. The equivalent circuit in Fig. 1.9 shows that V_J depends on a voltage divider, which includes the nonlinear, complex impedance of the attached cell membrane in series with the resistance ρ/d , where ρ is the specific resistance of the electrolyte and d the width of the cleft. Ion channels are modeled by voltage-dependent resistors, the cell membrane can be considered as a capacitor. The difference in ion concentrations between intracellular and extracellular environment appears as voltage source. Upon eliciting an action potential, the currents passing through the attached cell membrane have to flow through the electrolyte in the cleft. As a result, these currents cause a voltage drop along the cleft. Consequently, extracellular recordings are very efficient in the case of large contact areas of neural tissue and tight

attachment of the cells to the sensing surface. This model can also be used for estimating the signal amplitudes in cell clusters and larger tissue fragments. Extracellular recordings from single cells show signals which can largely differ in sign and shape from intracellular signals as recorded by classical microelectrodes. A better understanding of the signals is obtained by considering those ion channels which reside in the part of the cell membrane, which is not attached to the surface. Any device that can be used to measure the electrical potential on its surface is suitable for extracellular recordings. Integration of extracellular sensors into planar structures is preferred as planar surfaces are the most versatile substrates for *in vitro* cell cultures.

Planar metal electrodes are widely used. As illustrated in Fig. 1.10(a), isolated metal lines are used to connect the electrode area, which is open to the solution containing the cells. Metal electrodes are processed on insulating substrates, such as glass, using lithographic processes. The charge transfer between ionic and electronic conduction takes place at the interface between metal and electrolyte. The metal-electrolyte interface is commonly modeled by a resistor and a capacitor in parallel, where the resistive part represents possible electrochemical reactions and the capacitance stands for the double layer of ions at the interface. Fig. 1.10(b) shows a modified version of a field-effect transistor, which can also be used to record electrical surface potentials. If the fabrication process of a field-effect transistor is stopped before the deposition of the gate material, an open-gate field-effect transistor is created. Changes in the electrical surface potential above the channel area modulate the current between drain and source. This transistor-based electrical interface is of purely capacitive nature and prohibits faradaic currents and related unwanted electrochemical effects.

In [41] a biosensor array chip based on an extended 5V 0.5 μm CMOS process has been presented for high resolution imaging of extracellular signals from neural cells, cultured on the chip surface (Fig. 1.11). The chip provides 128 \times 128 capacitive sensors on an area of 1 mm². A mismatch-canceling calibration circuitry with current mode signal representation is

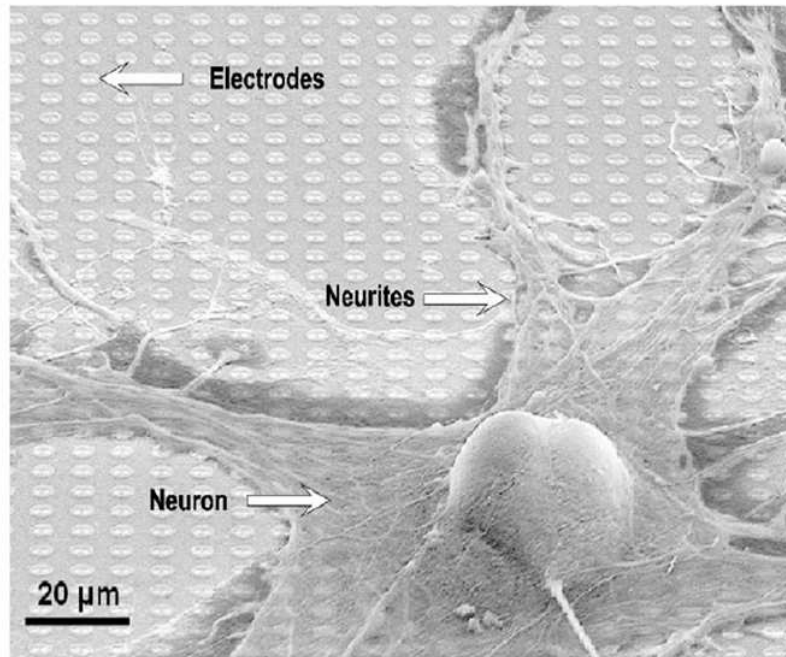


Figure 1.11: Snail neurons cultured on chip surface.

used. Currents from cell ion channels modulate the drain current of an integrated MOS transistor, as illustrated in Fig. 1.12. Results proved full functionality of the chip.

In [40], a CMOS-based 4×4 metal electrode array for stimulation and recording is described. It provides a pitch of $250 \mu\text{m}$ and electrode size of $40 \times 40 \mu\text{m}^2$ (Fig. 1.13). The device hosts active circuitry for stimulating and reading out cell signals. Signal processing and conditioning is performed on-chip.

Detecting and characterizing cells

For this purpose, capacitive and impedance sensing have demonstrated to be suitable techniques for compact and fully-electronic implementations. However, at present, CMOS implementations to our knowledge have not been reported yet.

In [44],[45] and [46], accurate analysis of individual cells and particles is performed in specific sensing sites while the sample is flowing in micro-

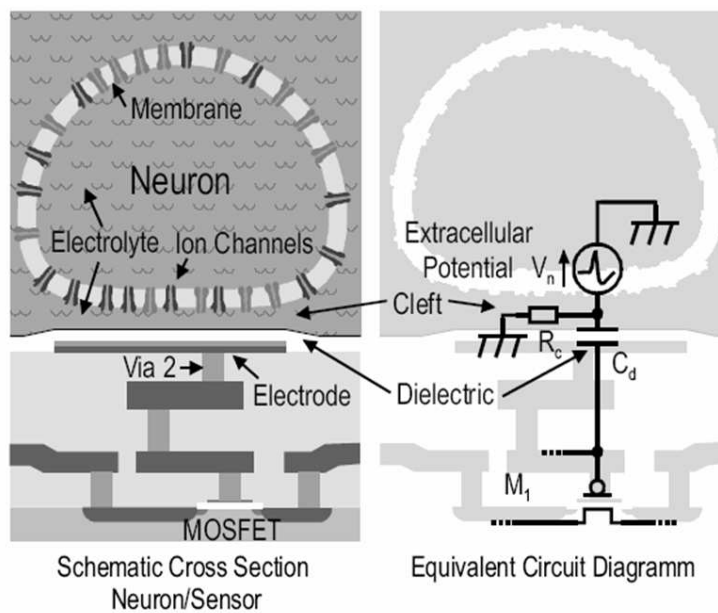


Figure 1.12: Sensor principle, based on the modulation of the drain current of a MOS transistor

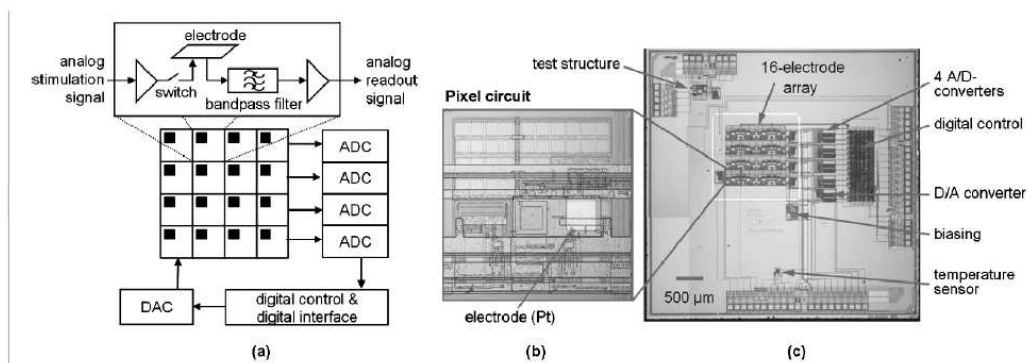


Figure 1.13: Metal electrode array with active CMOS circuitry for stimulation and recording. (a) Schematic of the chip architecture. (b) Photograph of an active pixel with a shifted metal electrode. (c) Photograph of the entire chip featuring a 4×4 pixels and peripheral circuitry.

fabricated channels. Size of cells can be compared with that of channels, so that they can be characterized one by one while flowing. The electrode size ranged from $20\ \mu\text{m}$ to $70\ \mu\text{m}$. Even in this case, external equipment or instrumentation is required for proper operation of the devices and for carrying out the desired measurements. Moreover, microfabrication techniques or microfluidic add-ons were necessary for proper operation. Besides this, the above devices rely on serial processing of cells, which could represent a limiting factor in order to extract rare cells, whose concentration are, for example, 2-6 individuals in 1 ml of blood [7]. Though implemented as discrete components systems, the proposed approaches are well suitable for CMOS integrated implementations. This would increase compactness, reduce large scale fabrication costs and, most of all, allow for a strong functional integration with other units.

In [52], a dielectrophoretic manipulator of clusters of particles also performs impedance measurements. However, due to geometrical limitations in the size of electrodes ($100\ \mu\text{m}$ wide), the device only deals with cluster of cells or particles, so that only detection of local concentrations of cells suspended in the sample may be performed. Anyway the device was low cost, as it relies on standard PCB technology with no microfluidic add-ons nor micromachining.

1.7 The MeDICS project

Beginning from 2001, the European Community funded the MeDICS project (Microelectronic Devices for Individual Cell Sorting, IST-2001-32437, 5th FP) [1] which included among the participants the University of Bologna, with the specific task of the electronic design at device and system level. The aim was to develop a technology, based on dielectrophoresis and conventional CMOS processes, which allowed to manipulate and detect single cells. The participants of the project, concluded in July 2004, were:

- University of Bologna, for silicon and system design, testing and

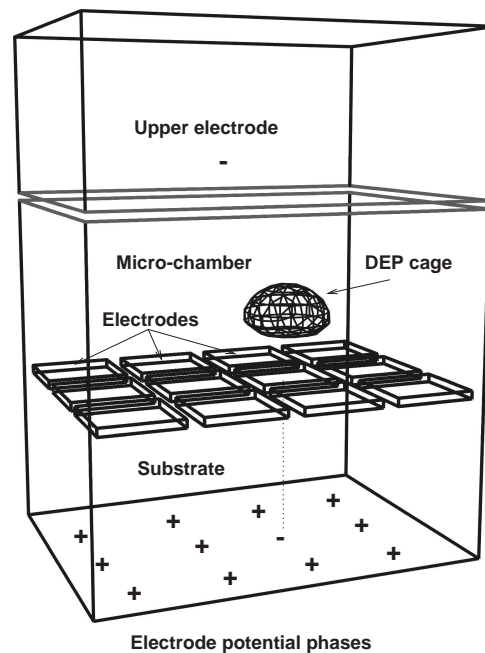


Figure 1.14: Structure of the designed cellular micro-manipulator

physical modeling.

- Silicon Biosystems, Bologna (I), for coordination and silicon design
- Commissariat à l’Energie Atomique (CEA), Grenoble (F), for biological validation (CEA-DSV) and fluidic packaging (CEA-LETI)
- Institut National de la Santé et de la Recherche Médicale (INSERM), Grenoble (F) for clinical testing and biological validation

The prototypal devices and system developed at University of Bologna represent the work presented in this thesis within the following chapters. This task involved a multidisciplinary approach, where traditional microelectronics had to deal with problems typical of biology and chemistry. The experimental part, once the devices have been realized and tested, played an important role in order to evaluate the effectiveness of the proposed technology. Other project partners provided complementary knowledge for biological validation of the devices, packaging and microfluidics in perspective of industrial exploitation of the proposed technology [2].

Chapter 2

A CMOS Chip for Single Cell Biology

Manipulation of populations of living cells on an individual basis is essential for the investigation of complex interactions among cells. In this chapter a new approach is presented for the integration on silicon of dielectrophoretic (DEP) actuators and embedded sensors that allow us to carry out this task. A prototypal device was realized, featuring a 8×8 mm² size, and implemented in a standard $0.35\mu\text{m}$ CMOS technology with 2 poly-silicon and 3 metal layers, featuring 102,400 actuation electrodes, arranged in an array of 320×320 , $20 \times 20\mu\text{m}^2$ micro-sites each comprising addressing logic, an embedded memory for electrode-programming and a sensor. This chip enables software-controlled displacement of more than 10k individual living-cells in a parallel fashion, allowing biologists to devise complex interaction protocols that are impossible to manage otherwise. The manipulation does not damage the viability of the cells, so that this approach could be a unique extension to the techniques already available to biologists.

2.1 Why integrating sensing and actuation in a lab-on-a-chip

As already mentioned in chapter 1, lab-on-a-chip technology has mainly aimed to speed-up DNA amplification and detection or other molecular analyses from preprocessed samples. Many technologies for fluid motion, DNA amplification, detection and other analytical functions have been miniaturized and have become mainstream techniques in biological laboratories.

Beside these advances on molecular analysis, there has been an emerging and still unmet need for lab-on-a-chip which are able to deal with cells. In fact, cell-analysis protocols must be carried out in a number of fields, from the sample preparation for biomolecular analysis, to drug screening. Few notable exceptions [41] [40] of lab-on-a-chip devices dealing with cells have been reported, but nevertheless these systems only deal with cells cultured on the chip surface. Although stimulated or analyzed, these cells cannot be displaced nor manipulated.

The problem of contactless, non-invasive, viable, automated manipulation techniques is still unmet, especially concerning applications for single cell biology. Dielectrophoresis showed to be a suitable technique [52] to be implemented in standard electronic technologies (PCB in this case). Our device aims to implement a CMOS cellular micromanipulator, in order to overcome the geometrical and functional limitations of the PCB device.

2.2 An introduction to dielectrophoresis

Dielectrophoresis has been employed for developing micro-fabricated devices for selective separation of cells [17, 9, 52, 14]. It is the physical phenomenon whereby uncharged particles, when subject to a non-uniform, time stationary (DC) or time varying (AC) electric field \mathbf{E} , experience a net force which is directed towards locations with increasing or decreasing field intensity according to the polarization properties of the matter.

The calculation of DEP forces, however, is a difficult task unless simplifying assumptions and simple geometries are taken into account [54, 13, 18]. Many theoretical and experimental works on dielectrophoresis [9, 16, 19, 20] have used the simplified force expression introduced by Pohl [13] for an infinitesimal particle of dipole moment \mathbf{p} immersed in an electric field \mathbf{E} :

$$\mathbf{F} = (\mathbf{p} \cdot \nabla)\mathbf{E}. \quad (2.1)$$

For particles of finite dimensions one can introduce an effective dipole moment term \mathbf{p}_{eff} producing an equivalent dipolar electrostatic field [18] so that (2.1) becomes:

$$\mathbf{F} = (\mathbf{p}_{\text{eff}} \cdot \nabla)\mathbf{E}_0 = K\nabla(E_0^2),$$

where \mathbf{E}_0 is the original electric field of intensity E_0 and K is a constant depending on the particle geometry. The above equation is correct under a first-order dipole approximation, which holds true only if the dimensions of the particle are very small compared to the dimensions of the energizing electrodes.

The force can be computed in a closed form for simple particle geometries like spheres, shelled spheres or ellipsoids. Considering a sinusoidal electric field where the electric field magnitude can be written as:

$$E_0(t) = E_0 \sin(\omega t)$$

the natural extension of analysis given by (2.1) allows one to calculate the time-averaged DEP forces exerted on a dielectric sphere immersed into a dielectric medium, where T is the signal period, $f = 1/T$ is the signal frequency and $\omega = 2\pi f$ the angular frequency, respectively.

Whenever the energizing signals are composed of sinusoidal in-phase and counter-phase voltage signals, a particle experiences time-averaged

DEP forces given by:

$$\begin{aligned}
 \langle \mathbf{F}(t) \rangle &= \frac{1}{T} \int_0^T K \nabla (E_0^2(t)) dt = \\
 &= \frac{1}{T} \int_0^T 2\pi \varepsilon_0 \varepsilon_e r^3 \operatorname{Re} [f_{\text{CM}}] \nabla (E_0)^2 \sin^2(\omega t) dt = \\
 &= \pi \varepsilon_0 \varepsilon_e r^3 \operatorname{Re} [f_{\text{CM}}] \nabla (E_0)^2, \tag{2.2}
 \end{aligned}$$

where ε_0 is the vacuum dielectric constant, ε_e is the dielectric constant of the suspending medium, r is the particle radius, and f_{CM} is the Clausius-Mossotti factor, a function of the medium and particle electric permittivities [21] given by:

$$f_{\text{CM}} = \frac{\varepsilon_p^* - \varepsilon_e^*}{\varepsilon_p^* + 2\varepsilon_e^*}, \tag{2.3}$$

where ε_p^* and ε_e^* are the complex permittivities of the particle and the suspending medium, respectively. The generic relative complex permittivity terms can be expressed as:

$$\varepsilon^* = \varepsilon - j \frac{\sigma}{\omega},$$

where ε, σ are the permittivity and the conductivity of the matter, respectively. Under the hypothesis that $\varepsilon \gg \sigma/\omega$, often verified in practice at relatively high frequencies, one can consider only the real part of the complex permittivity parameter of the matter ($\varepsilon^* \simeq \varepsilon$). Thus, under the above assumption the Clausius-Mossotti's factor becomes equal to its real part given by:

$$\operatorname{Re} [f_{\text{CM}}] = \frac{\varepsilon_p - \varepsilon_e}{\varepsilon_p + 2\varepsilon_e}.$$

Use of (2.2) for DEP forces calculation has serious drawbacks. Microelectronics miniaturization allows one to implement electrodes generating electric field into labs-on-a-chip (tiny devices where physical and chemical microreactions are performed in parallel fashion) whose dimensions are comparable with particle radius. In this case, the first-order dipole approximation cannot be employed, since the dielectrophoretic potential

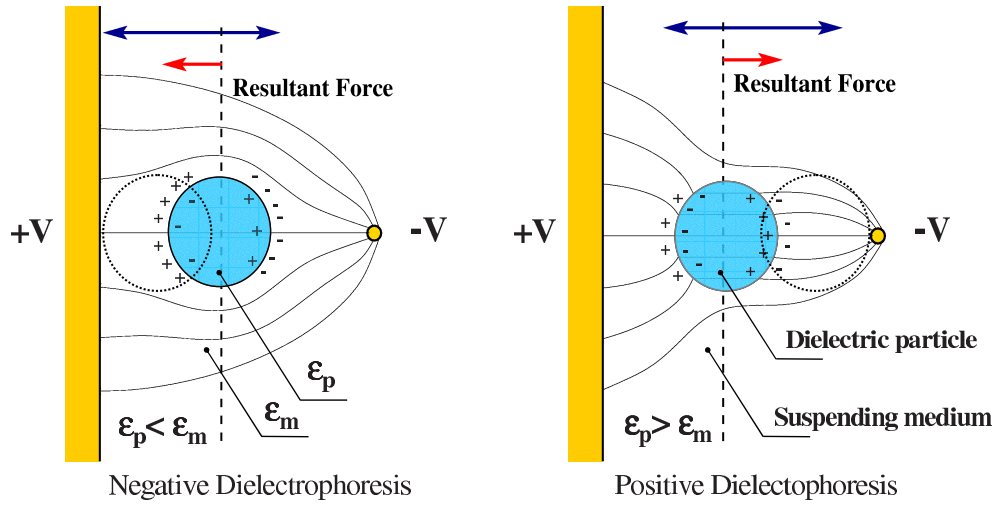


Figure 2.1: Positive and negative dielectrophoresis.

determined by using equation (2.2) is not correct unless $r \ll l$, where l is the electrode width. This may cause errors in the estimation of DEP forces acting on large particles, as well as their position and motion.

When this limit is overcome, the approximation is not suitable and a more precise evaluation of DEP forces is necessary. In literature there are many works where the multipolar theory has been formalized and employed for DEP forces evaluation and particle motion prediction [21, 67, 22, 23]. However, the presented approaches are related to closed form solutions in simple geometries.

A more exhaustive review of dielectrophoresis and related techniques has recently been published in [53].

2.3 Dielectrophoresis and living cells

Since microorganisms and cells are mostly electrically neutral, dielectrophoresis (DEP), is well suited to their manipulation. Dielectrophoresis [54] is the physical phenomenon whereby neutral particles, in response to a spatially non-uniform electric field E , experience a net force directed toward locations with increasing or decreasing field intensity according to the physical properties of particles and medium. In the first case, the force

is called positive dielectrophoresis (pDEP), while in the second case it is called negative dielectrophoresis (nDEP).

Several approaches for microorganism manipulation have been developed based on dielectrophoresis. In [14], both pDEP and nDEP are used to precisely displace cells in a microchamber formed between two facing glass chips with elongated electrodes. However, cells get in contact with device surfaces and tend to stick to them.

A solution is to levitate cells while manipulating them. Since maxima of the electric field can not be established away from the electrodes, stable levitation is possible only with nDEP force.

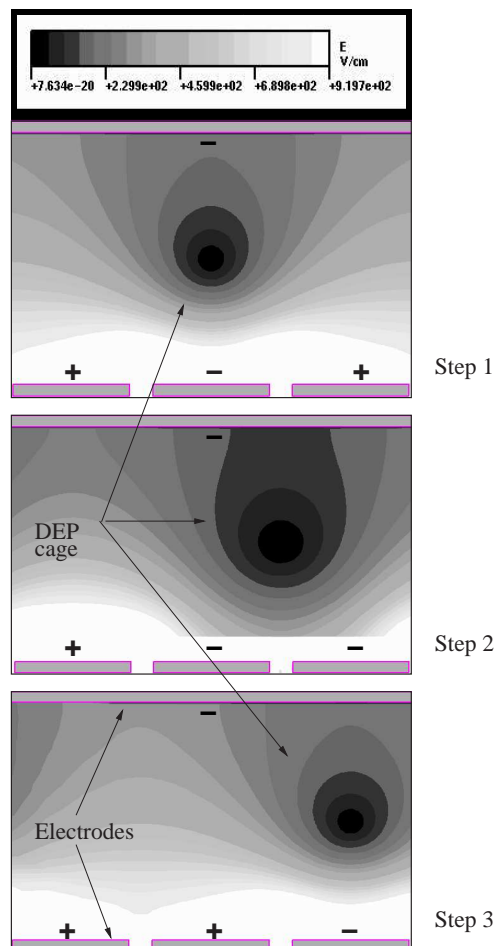


Figure 2.2: The moving DEP cages approach for cell manipulation. Electromagnetic simulations show how closed cages can be dragged along the chip surface just by changing polarization of the electrode array.

Hence, the use of closed nDEP cages has been proposed. In [16], 3D structures of electrodes located at the vertexes of a cube are used for such purpose. The main drawback is that fluid flow is required to lead cells into and out of the DEP cage and electrode alignment in three dimensions is necessary.

In [55], traveling waves are combined with nDEP to move cells in a microchamber without fluid flow. However, it is difficult to precisely position cells, as needed by multi-step experimental protocols, due to the fact that the cell speed depends on the type of cell.

As far as sensing is concerned, approaches such as optical [56] or fluorescent labeling (e.g. as used in μ FACS) have been proposed. Their main drawbacks are that they normally require bulky and expensive equipment [12], are characterized by complex sample preparations and are thus not suited to miniaturization.

This explains the emerging interest in electrical sensing approaches such as those based on impedance measurement [45].

The possibility of investigating *individual* cell interactions on a large scale would open up great possibilities for tasks such as drug screening, cell separation and analysis.

The standard CMOS microsystem which will be described in the following sections and first introduced in [57], implements the moving DEP-cages approach (envisaged in [24] and [62]), in order to *individually* detect and manipulate more than 10K cells in a parallel fashion. To the best of our knowledge, this is the first device that allows programmable manipulation of individual particles with no need for fluid flow nor micromachining, combined with embedded optical detection.

2.4 Design objectives and specifications

2.4.1 Design approach

The approach followed in the development of this microsystem for cell analysis was based on the following points:

Platform Approach - The objective was to create a flexible platform which could be used to carry out various different analytical protocols by just changing the software and reagents. Although this is a well established concept in electronic design, it is an innovative and challenging feature to implement in lab-on-a-chip.

Smart Chips by Active Substrates - Although the fabrication process of active silicon chips is much more complex than the microfabrication processes commonly used for passive biochips (e.g. with simple microchannels etched in glass), the availability of transistors affords massive parallelism, enabled by I/O multiplexing, and integrated detection.

Use of Standard CMOS - The use of commonly available fabrication processes without micromachining options has several advantages. It is possible to vary the shape, connection and number of microchambers of the device by simply changing the microfluidic packaging on top of the silicon chip, instead of requiring a new mask set. The availability of numerous foundries means the possibility of choosing the best trade off between minimum resolution and fabrication cost in a wide range of processes.

Scalability - while it is possible to handle cells with this prototype, more advanced technologies would enable the design of chips to handle individual bacteria or viruses. A more detailed analysis of scaling effects is presented in [47] and [48].

A sketch of the device is shown in Fig. 2.3. A micro-chamber is defined by the chip surface and a conductive glass lid. The chip surface

implements a two-dimensional array of micro-sites, each consisting of a superficial electrode, embedded sensors and logic. The electrode array is actually implemented with CMOS top-metal and protected from the liquid by the standard CMOS passivation, not shown in the figure. Since the chip is disposable, we are not concerned with long-term reliability issues, so that standard passivation is good enough in this perspective.

A closed DEP cage in the spatial region above a micro-site can be created by connecting the associated electrode and the microchamber lid to a counter-phase (V_{phim}) sinusoidal voltage, while the electrodes of the neighboring micro-sites are connected to an in-phase sinusoidal voltage (V_{phip}) [24]. A field minimum is thus created in the liquid, corresponding to a DEP cage in which, depending on its size, one or more particles can be trapped and levitated.

By changing, under software control, the pattern of voltages applied to the electrodes, DEP cages can be independently moved around the device plane, thus grabbing and dragging cells and/or microbeads across the chip.

Particles in the sample can be detected by the changes in optical radiation impinging on the photodiode associated with each micro-site.

Implementation of the moving DEP-cages approach with the proposed CMOS chip enables one to achieve the key features which are summarized in the following:

Single Cell Addressing and Selection. Thanks to the small pitch of the electrodes, single cells can be individually trapped in separate cages and independently moved on the device.

Grab-and-Drag Motion. Particle position is digitally controlled step-by-step in a deterministic way, by applying the corresponding pattern of voltages to the array which sets the position of the DEP cages. This feature is difficult to achieve with motion techniques based on fluid flows or on traveling-wave dielectrophoresis [55]. This difference

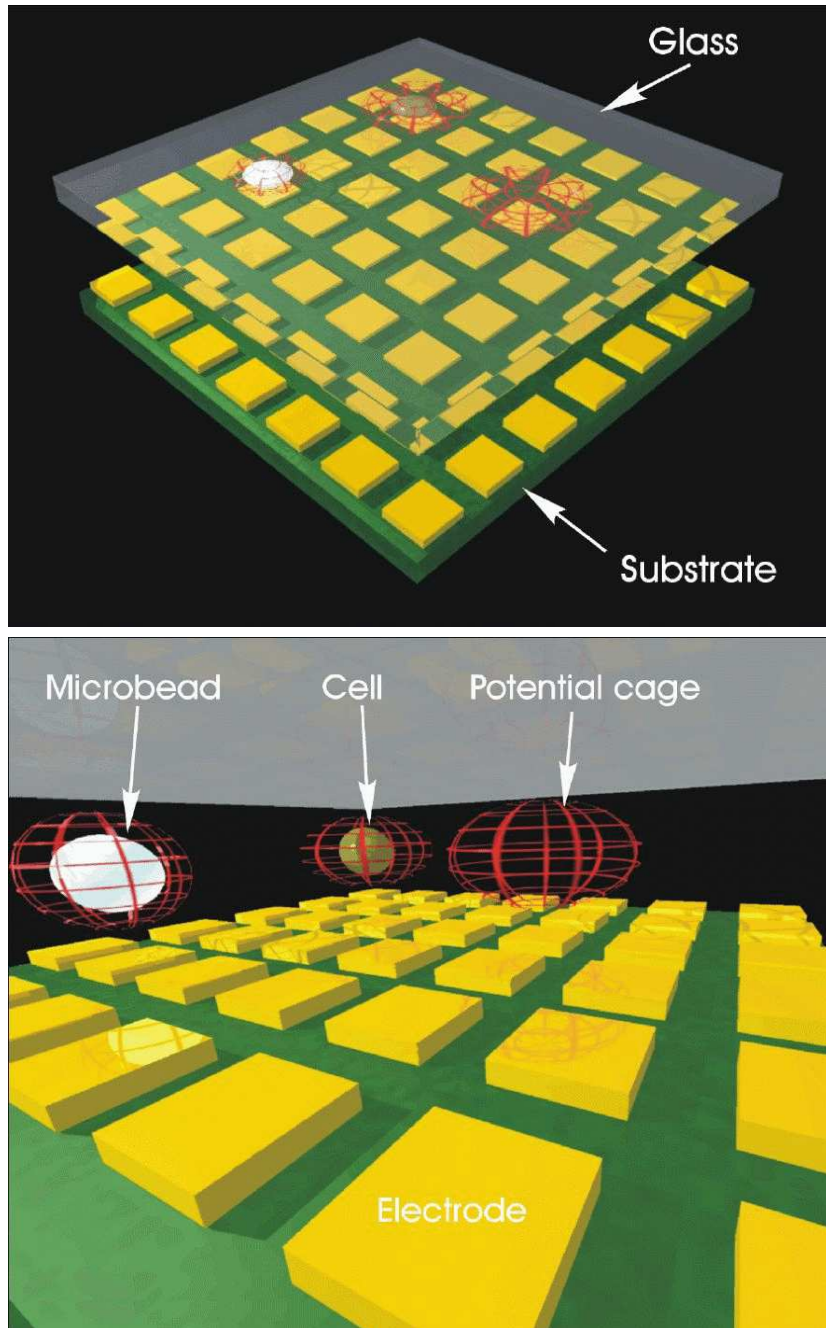


Figure 2.3: Sketch of the biochip section

may be compared to that existing between step-motors and asynchronous electric motors.

Embedded Monitoring. Use of an active substrate implemented with microelectronic semiconductor technology allows us to integrate an array of optical or capacitive sensors to detect the position and possibly the status of all particles inside the device. This information can be used to provide meaningful feedback on device operations. Thus, the device has the potential to be used without bulky and expensive external microscopes and cameras. This will be important, in perspective, for portable lab-on-a-chip.

Massive Parallelism. Thousands of cells can be concurrently and independently moved and detected thanks to the large number of electrodes.

Contactless Movement. The closed DEP cage allows particles to be suspended in a contactless manner thus helping the prevention of cell adhesion to sensor surfaces.

Robustness. Using an array instead of microchannels allows one to:

- (i) alleviate clogging problems that are common with cells in micro-channel devices;
- (ii) be fault tolerant with respect to cells that are stuck, so that new routing paths can be devised for other cells.

2.4.2 Examples of applications

This chip will enable several experiments unaffordable with existing techniques, with applications ranging from diagnostics to drug discovery.

For example, a microbead coated (according to known art) with antibodies for a known cell receptor, could be mated (by merging them in a cage) with an unknown cell. By pulling them apart with a controlled force (i.e. separating their cages) one may test whether the molecules coating the

bead match the receptors on the cell surface (they remain stuck together), thus identifying the cell itself (diagnosis).

On the other hand, using a known cell line and a large number of beads each coated with a different compound of uncertain activity, one may detect which of these compounds binds to the unknown receptors on the cell surface (drug screening).

Another protocol which could be implemented on this platform is cell-sorting by label-free separation. As it was demonstrated in [62], exploiting the differences of dielectrophoretic response as a function of the frequency of the applied AC electric field, it is possible to selectively move one population of cells. This approach may be of interest for example in the separation and fractionation of cell populations for which molecular markers are not available.

Another possibility is to tap the wide range of available fluorescent markers developed for established cell separation methods like fluorescent activated cell sorters (FACS). Using these legacy techniques, one may label cells with appropriate fluorescent molecular markers and use conventional fluorescence microscopes to identify and tag the cells on the array. Separation could then be carried out relying on the possibility to selectively move a set of cages (according to the marker of the trapped cell) toward a separate microchamber, where they could be flushed out and recovered or further analyzed. In this case the advantage on FACS machines would be the possibility to work on small cell loads. In fact FACS typically require few millions of cells as a minimum, while the proposed chip may start with samples of few thousands cells and still be able to recover a small percentage of cells of interest. This would be important for example in the analysis of small biopsies.

2.4.3 Design constraints and specifications

The device has been optimized for handling eukaryotic cells (such as the lymphocytes found in blood) in the range of $20 - 30\mu m$. A design guideline, derived from analysis of simulation results on the horizontal

DEP forces as a function of particle size with respect to the electrodes [26], suggests that the electrode pitch should be similar to the cell size. Since the counter-phase electrode must be surrounded by in-phase electrodes to create a DEP cage, the periodicity of the cages, as well as the attraction basin, is actually two electrodes. Accordingly, two cells may fit into one cage. Yet we are able to manipulate them individually since two cells originally in one cage can be segregated into two different cages by simply enlarging and then dividing the cage. Larger particles can also be handled by increasing the width of the cage to encompass more than one electrode.

Increasing the number of electrodes on the array one may increase capacity (number of cells in the input sample) and selectivity, i.e. possibility to select a smaller percentage of cells. However, silicon cost increases with chip size. Accordingly, the total number of cages was chosen to be greater than ten thousands. On one hand, this is satisfactory to recover a significant number of cells (10-100) which may be present in low percentage (0,1-1%) in the starting sample. On the other hand, chip size is thus still acceptable.

The time constants for cell motion due to DEP forces are relatively slow (about one second or more to make a $20\mu m$ step). This relaxes timing constraints for array programming, as well as for sensing frame rate.

For the choice of the most appropriate CMOS technology the following considerations were taken into account. Since DEP force is proportional, under certain assumptions, to the square of the applied voltages [26], the supply voltage should be as large as possible, as this will limit actuation voltages.

As opposed to conventional IC designs, the lower the resolution of the technology, the lower the cost of the chip, since die size is set from other specifications. Scaling beyond the point where the required number of transistors fits in the micro-site area does not improve neither cost nor performance [47].

In fact, scaling is just required if one wants to manipulate smaller cells, like individual bacteria (typically $1 - 3\mu m$) or viruses ($100 - 300nm$).

2.5 Chip architecture

The lab-on-a-chip architecture is based on a two-dimensional array of micro-sites whose purpose is to:

1. generate the electric field necessary to create dielectrophoretic cages,
2. detect the presence of single particles or clusters trapped in cages by using optical or capacitive sensing.

Each micro-site consists of an actuation electrode, implemented with a top metal plate, and underlying embedded circuitry for programming and detection. Micro-sites can be addressed in a random access mode by means of row and column decoders, for both actuation and sensing.

The presence of particles is detected by photodiodes, embedded in the substrate, that measure signal variations from uniform light impinging on

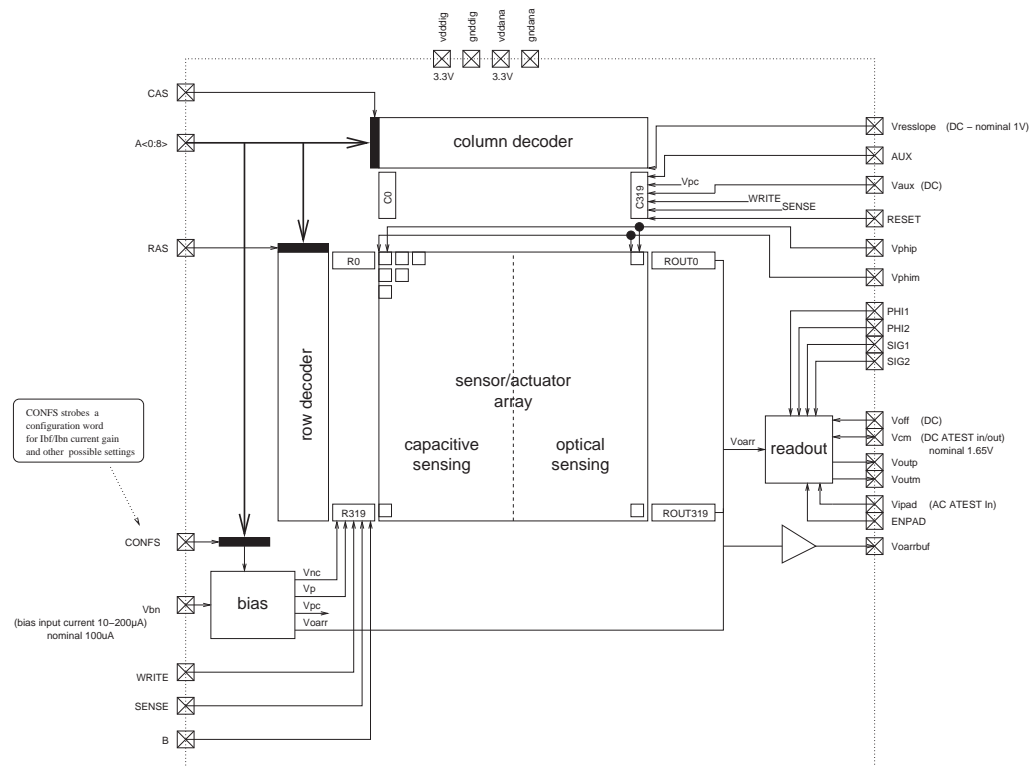


Figure 2.4: Chip Architecture

the chip surface. Another kind of sensor will be described and discussed later in this chapter, in section 2.5.2.

The mode of operation consists of three phases:

- programming,
- actuation
- sensing.

During *programming* the actuation pattern is stored into the micro-sites of the array to determine DEP cage number, displacement and shape.

In the *actuation* phase each electrode is energized by either an in-phase (V_{phip}) or counter-phase ($V_{\text{phim}} = -V_{\text{phip}}$) sinusoidal actuation voltage signal, according to the programmed patterns. More precisely, the two actuation voltages are centered around a bias voltage and defined as follows:

$$V_{\text{phip}} = \frac{V_{DD}}{2} + \frac{A}{2} \sin(\omega t)$$

$$V_{\text{phim}} = \frac{V_{DD}}{2} - \frac{A}{2} \sin(\omega t)$$

where A is the peak-to-peak amplitude of the AC stimuli.

During the *sensing* phase, the actuation voltages are halted, to avoid coupling to sensors and readout, and the corresponding image of the array is grabbed. Thus *actuation* and *sensing* phases are always kept non-overlapping. On the contrary, *programming* and *actuation* may be concurrent: *actuation* patterns can be changed in *real-time* while electrodes keep energizing the system.

The general architecture of the chip is sketched in Fig. 2.4 where the main blocks are:

- the array of micro-sites. It is composed of 320×320 elements of $20\mu\text{m}$ pitch.
- 9-bit static column/row decoders for random access.
- Bias generator block.

- Readout circuit block.

Referring to Fig.2.4, the row ($R[0:319]$) and column ($C[0:319]$) circuits provide the logic signals to program and read-out each micro-site. The $A<0:8>$ word is used for either addressing the microsites and setting the start-up configuration. The microsites addressing is performed by sampling the address $A<0:8>$ on the rising edge of the CAS and RAS signals for the column and row decoder, respectively. The configuration word is sampled on the rising edge of the “configuration strobe” CONF_S and is used to set the bias current for both readout block and cells, as well as the gain of the readout circuit.

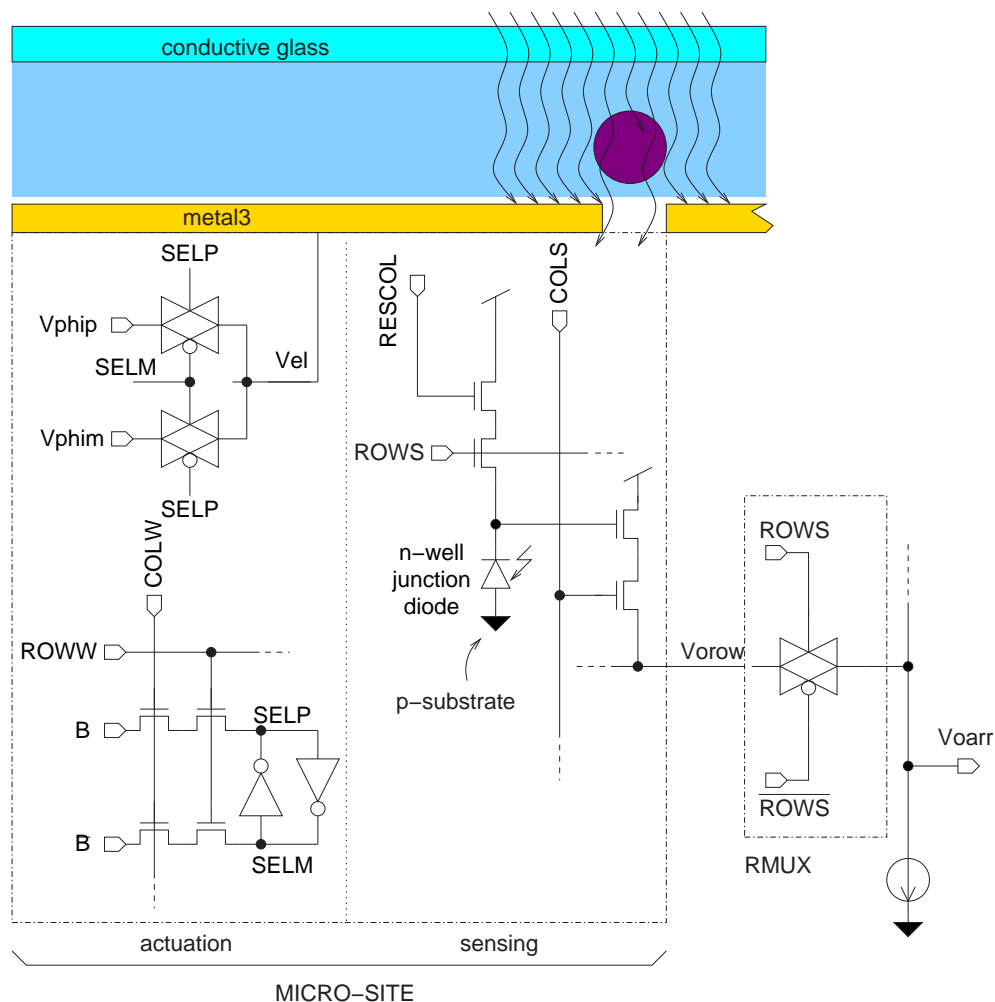


Figure 2.5: Micro-site circuit schematic

2.5.1 Micro-site circuit with optical sensors

The schematic of the micro-site circuit implementing optical sensing is reported in Fig.2.5. Vertical and horizontal labels refer to signals generated by the column and row decoders, respectively.

The actuation circuit is composed of two complementary pass-transistors controlled by a 1-bit memory element.

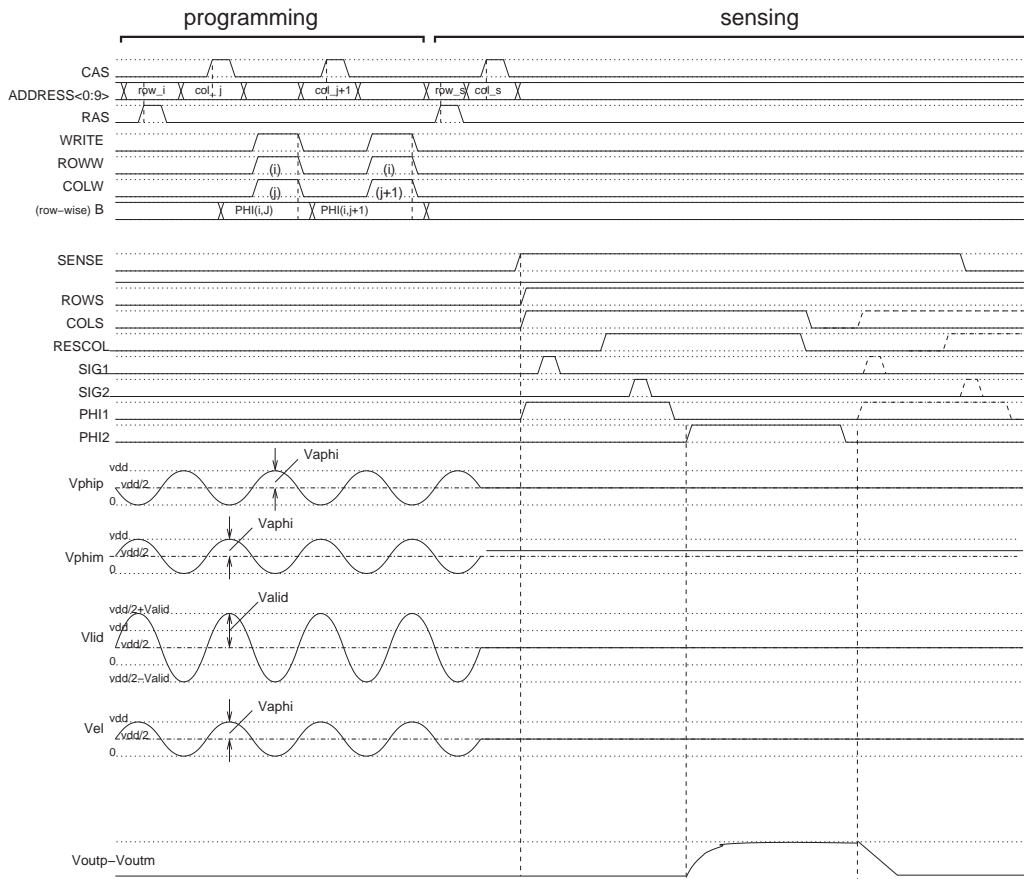


Figure 2.6: Representation of the waveforms used to control actuation and optical sensing

During the *programming* phase, the micro-site is addressed and WRITE is activated, thus the metal 3 electrode can be switched to either V_{phip} or V_{phim} by programming with the B signal the memory element addressed by ROWW and COLW. The metal plate setting is kept by the memory until a new programming phase occurs.

Electrode peak-current is due to capacitive coupling with neighboring electrodes and lid. In the worst case it is about $5\mu A$, for an electrode programmed at V_{phip} surrounded by V_{phim} electrodes and working at $10MHz$, and produces a negligible $10mV$ voltage drop through the pass transistors ($R_{\text{on}} = 2k\Omega$).

During the *sensing* phase the actuation signals are halted, avoiding spurious coupling with the pixel readout. Thanks to the particle inertia and fast readout, cells keep their position in levitation within the microchamber. The right side of the schematic of Fig.2.5 shows the sensing circuit, consisting of a CMOS active-pixel sensor (APS) [64], implemented with a $2 \times 17 \mu m^2$ well-junction photodiode placed underneath the $1.2\mu m$ -wide gap that separates each electrode with its right neighbor. The sensor array is read out row-wise by addressing each micro-site and asserting the SENSE signal so that ROWS and COLS are activated. The control waveforms are schematically shown in Fig. 2.6.

2.5.2 Micro-site circuit with capacitive sensors

In the same chip, a CMOS capacitive sensor array could also be implemented with the aim of detecting particles suspended in the microchamber delimited by the chip surface and a conductive lid. The capacitive microsite hosts the same circuits used in the optical version for DEP-based particle manipulation. Capacitive sensing might overcome the limits of optical detection (e.g. transparent particles) and does not rely on any external equipment. For instance, with optical sensors, lamps providing uniform illumination may be required as well as optical fibers, lenses, etc.

The CMOS chip is covered by a conductive glass lid spaced $100\mu m$ apart. A pierced piece of double adhesive tape acts as a gasket. As in the implementation with photodiodes, in the resulting closed micro-chamber particles and cells in their suspending medium can be injected through holes in the glass.

A closer view of each microsite with capacitive detection capabilities is shown in Fig. 2.7. Our aim is the detection of variations in dielectric per-

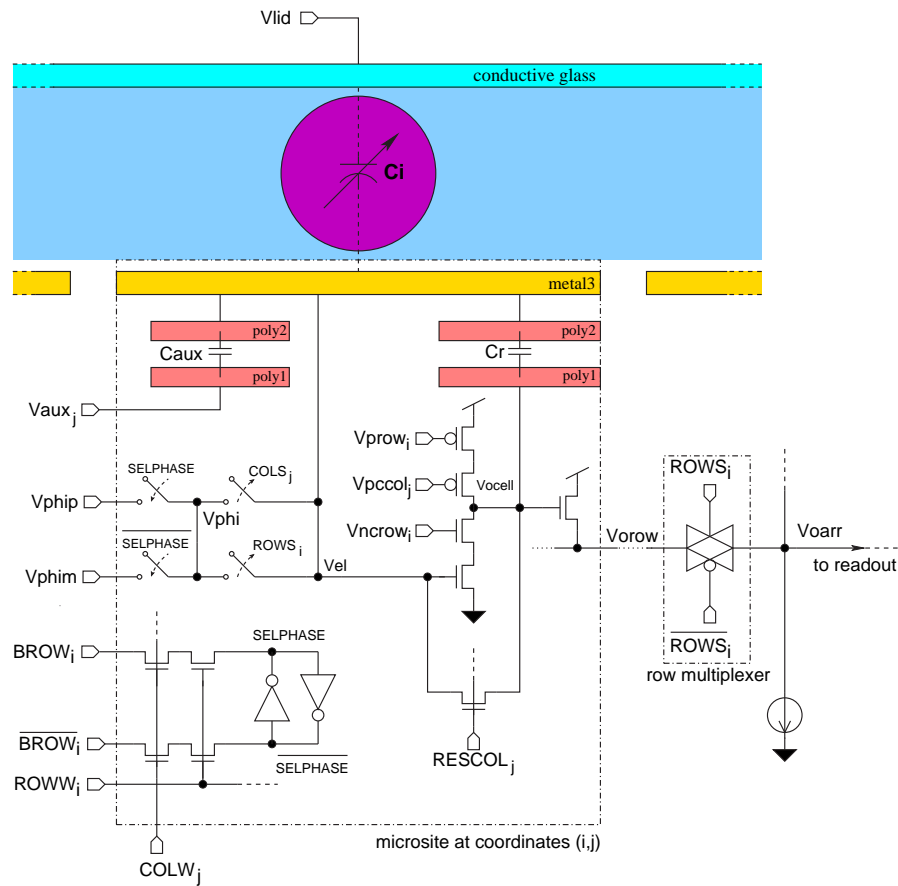


Figure 2.7: Schematic of the micro-site with embedded capacitive detectors

mittivity caused by the presence of particles in the region above the superficial electrodes, which affects the coupling capacitance with the lid. The circuit can operate as a sensor or as a DEP actuator, the electrode is time-multiplexed between actuation and sensing. During the actuation phase ROWS and COLS are inactive. The circuit generates the electric fields necessary to deploy DEP forces by connecting through CMOS transfer gates the superficial metal electrode to an in-phase (V_{phip}) or to a counter-phase sinusoidal voltage (V_{phim}), while the lid is connected to V_{phim} . Once a microsite at coordinates (i,j) is addressed, the selection is controlled by a memory element driven by ROWW, COLW and BROW.

During the sensing phase the sinusoidal voltages are halted and the electrode of the addressed cell is disconnected from V_{phip} and V_{phim} . Fig. 2.9 shows a schematic view of the featured sensing scheme. The input

Chapter 2. A CMOS Chip for Single Cell Biology

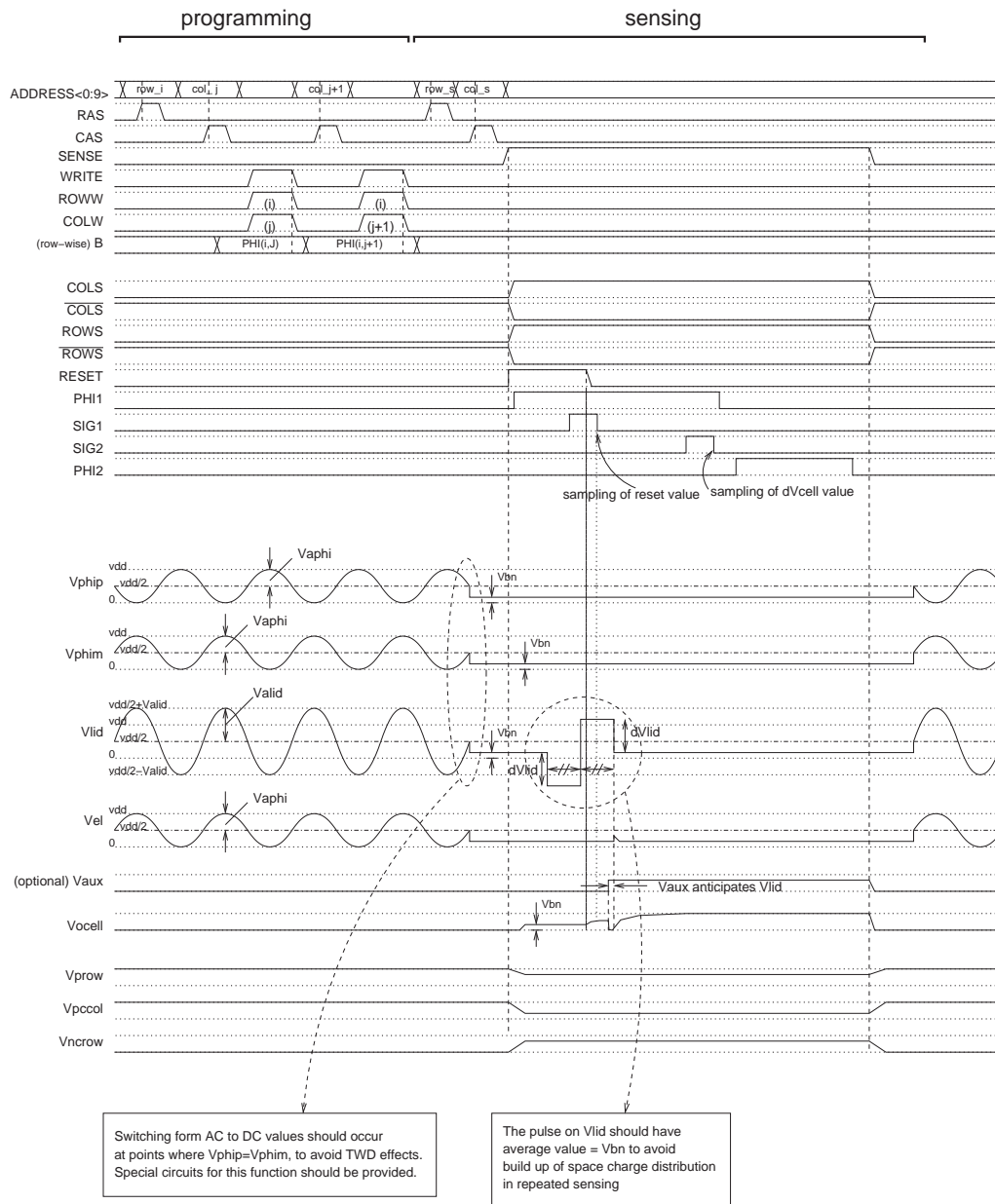


Figure 2.8: Operation of the device during actuation and capacitive sensing.

capacitance C_i can be thought of as the coupling capacitance between the lid and the microsite electrode. The cascode inverter implements a charge amplifier. The output of the sensor array V_{oarr} is generated by a source follower driving an active load through the addressed row multiplexer.

By activating RESCOL the output of the charge amplifier is brought to the reference value V_{bn} , corresponding to the threshold voltage of the cascode inverter. Then, RESCOL is deactivated and after charge injection the readout stage samples the reset voltage (t_1). A voltage step on the lid will induce in V_{ocell} a voltage variation which is proportional to the input and feedback capacitances C_i , C_F and to the step amplitude. In t_3 the output voltage is sampled again by the readout stage which amplifies and outputs the sensed variation. An equal duration opposite voltage pulse is

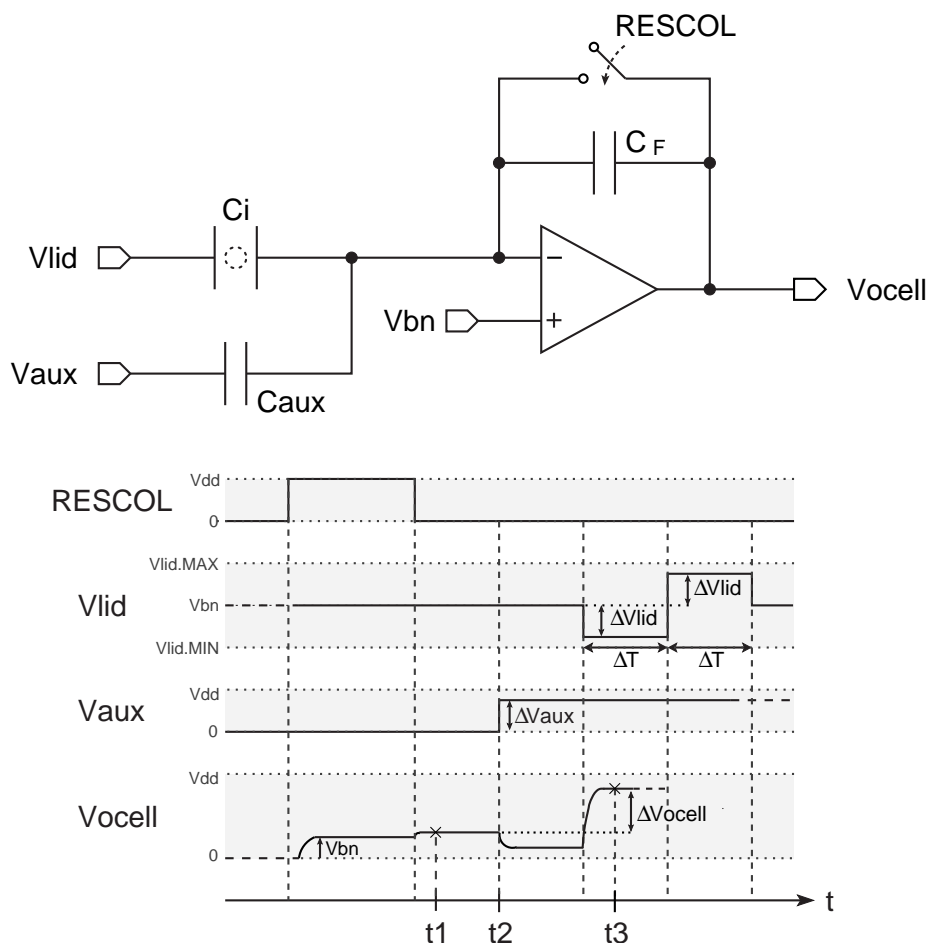


Figure 2.9: Capacitive sensing scheme and principle.

finally applied to the lid in order to prevent the build-up of a DC electric field in the liquid. Moreover, DEP forces must be restored before particles have significantly changed their position or have stuck to the surface.

An auxiliary capacitance C_{aux} has also been included to subtract a programmable offset charge (t_2) in order to avoid saturation of the charge amplifier when higher voltage pulses are applied on the lid so as to maximize the output voltage swing. The pitch of each site is also in this case $20\mu\text{m}$.

2.5.3 Read-out circuit

The readout amplifier, shown in Fig. 2.10, is a fully differential charge integrator implemented using a high-swing folded cascode switched capacitor (SC) operational amplifier with common mode feedback.

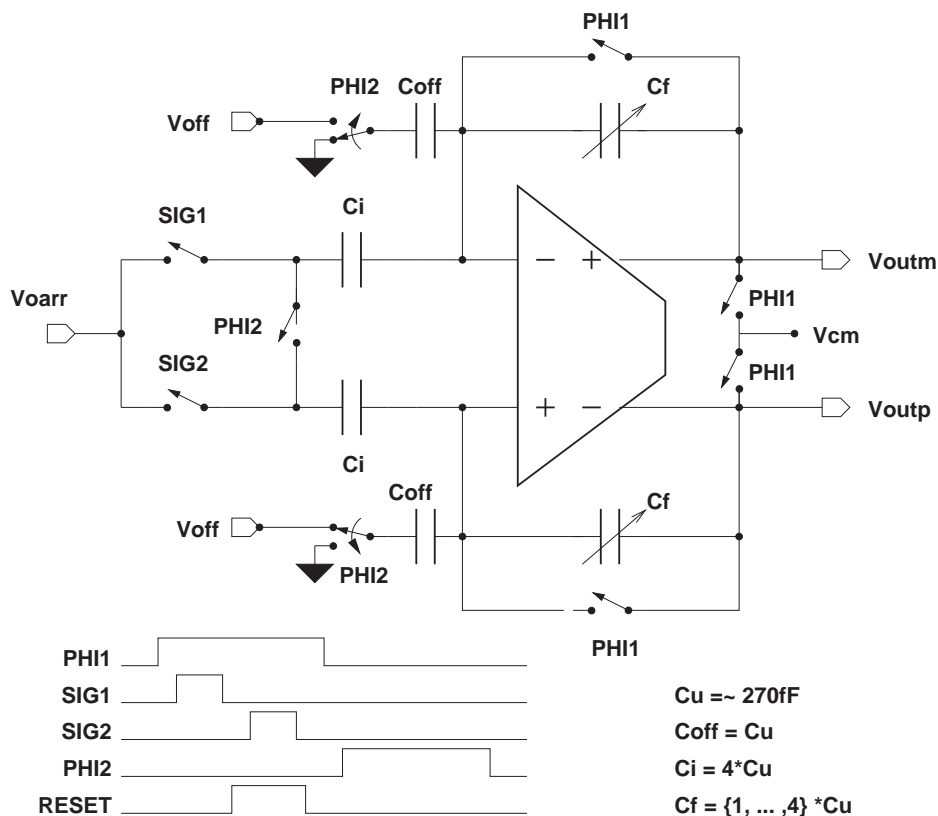
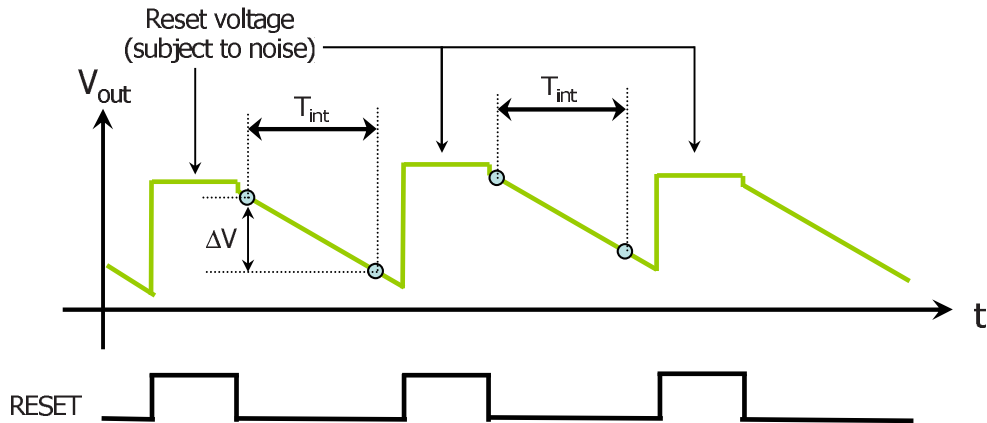


Figure 2.10: Readout circuit schematic



Reset noise: MOS channel charge injection, KTC noise, G-D G-S couplings, etc.

Figure 2.11: Correlated double sampling scheme (CDS). The waveforms are referred to the optical sensing scheme.

The input capacitance C_i is fixed to four times a unit capacitor $C_U \simeq 270\text{fF}$, while the feedback capacitance C_f is implemented as a bank of four unit capacitors each in series with CMOS switches. The switches are set by using the start-up configuration word so as to fix variable gains in the set of $\{1, 4/3, 2, 4\}$.

After the integration time, the APS output V_{oarr} of the selected microsite is sampled by SIG1 and is stored on the corresponding C_i . While PHI1 is still high, the RESET signal is activated, and the reset voltage is sampled during SIG2 on the other C_i . Subtracting the reset voltage allows us to compensate for $1/f$ and fixed pattern noise of photodiode and read-out follower transistor, with a correlated double sampling scheme (CDS) [65], as depicted in Fig. 2.11.

Since cells induce small perturbations, the signal is a small variation on top of a larger voltage swing. Thus, increasing charge amplifier gain in order to boost the sensitivity would take the output to saturation. To avoid this, a fixed charge is subtracted from the input by means of V_{off} to keep the output within the range. The output differential voltage is provided

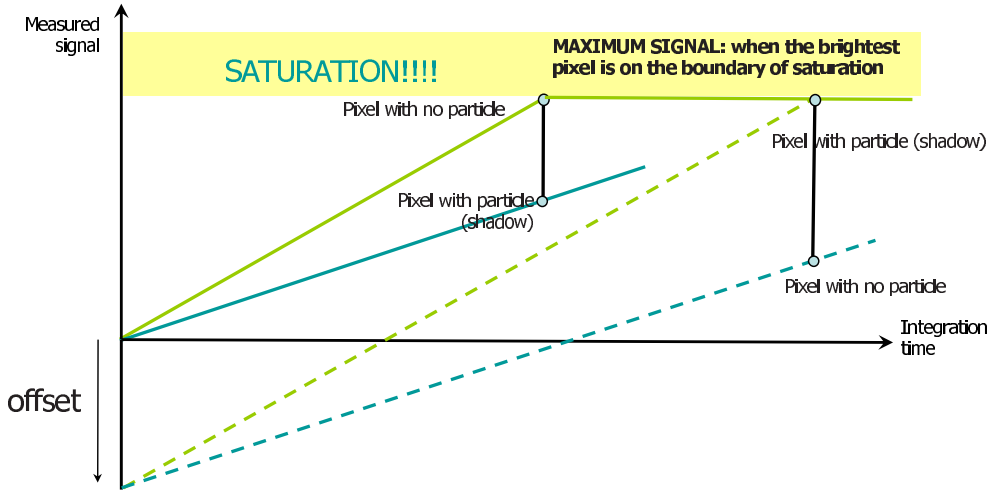


Figure 2.12: Signal boosting technique. Subtraction of an offset charge or voltage allows for a higher signal dynamic range.

during PHI2 according to the following relationship:

$$\begin{aligned}
 V_{\text{outp}} - V_{\text{outm}} &= \frac{C_i (V_{\text{oarr}}@SIG2 - V_{\text{oarr}}@SIG1) - 2C_{\text{off}}V_{\text{off}}}{C_f} = \\
 &= \frac{C_i}{C_f} \left(V_{\text{oarr}}@SIG2 - V_{\text{oarr}}@SIG1 - \frac{V_{\text{off}}}{2} \right)
 \end{aligned}$$

In other words, the use of V_{off} actually doubles the output range: the differential output voltage can then be even negative (which would otherwise be impossible since the pixel reset voltage $V_{\text{oarr}}@SIG2$ is always higher than the integrated voltage $V_{\text{oarr}}@SIG1$). The doubled output swing can thus be used to increase the charge integrator gain C_i/C_f . The principle used for signal boosting is summarized in Fig. 2.12.

2.6 Preliminary test results

Fig. 2.13 shows the chip in the microfluidic package, described in [66]. After a conductive-glass lid with SU8 walls is glued to the chip to define the microchamber, the die is mounted directly on the printed circuit board (PCB) with a chip-on-board technique.

The lid is spaced about $85\mu m$ from the chip surface. The strength of the DEP-cage mostly depends from its height above the array: since near the array field-gradients are stronger, the lower the cage the stronger the force. In turn, cage height increases with lid height and decreases with lid-voltage amplitude. For example, results from simulations show that increasing lid height from $50\mu m$ to $80\mu m$ while increasing lid-voltage amplitude from $3.3V_{pp}$ to $6.6V_{pp}$, cage height is approximately the same, i.e. about $15\mu m$. Considering a cell radius of about $10\mu m$ this is somewhat a lower-bound in order to prevent cell contact with the array. Also, for a given lid-voltage amplitude, DEP-force sensitivity to microchamber height is low. For example, keeping a $3.3V_{pp}$ lid-voltage, increasing lid-height as above from $50\mu m$ to $80\mu m$ (i.e. +60%), the horizontal DEP force decreases, due to the variation of cage height, of less than -50% only. It is thus apparent that inter-device variations of microchamber height (e.g. $\pm 10\%$ due to SU8 thickness variations), or intra-device non-planarity of the lid, have a negligible impact on DEP-cage strength.

Epoxy resin is used for protecting bonding-wires. The fluidic inlet is provided by a capillary connected to an opening in the microchamber lateral wall and sealed with a drop of insulating glue. A drop of conductive glue is used to electrically connect the lid electrode to the PCB.

The die photo is shown in Fig. 2.14, where the main blocks are identified.

After a sample ($50\mu m$ polystyrene beads in water) has been flushed into the microchamber, the beads are randomly distributed. Fig. 2.15 shows the corresponding image acquired with the embedded optical sensors.

Following the introduction of the sample, DEP cages are activated ($V_{p_{hip}}, V_{p_{him}}, 3.3V_{pp}$). Since in this case the bead diameter is more than twice the electrode pitch, the cage is set to 2×2 electrodes. Three snapshots of the selective motion of one bead are reported in Fig. 2.16 (i,ii,iii). The top line shows the images acquired by the microscope while the bottom line displays the corresponding programming pattern, where gray and white squares indicate the electrodes receiving $V_{p_{him}}$ and $V_{p_{hip}}$, respectively (the lid is always proportional to $V_{p_{him}}$). The time for particles to complete one

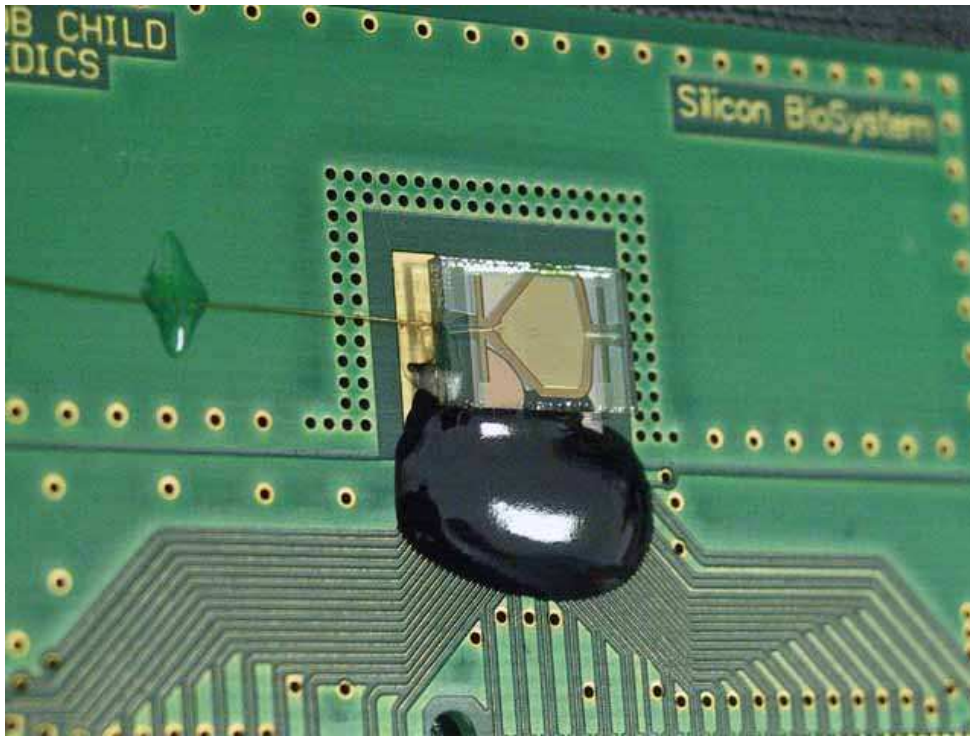


Figure 2.13: Chip in microfluidic packaging: the die is mounted directly on the PCB with chip-on-board technique, while a conductive-glass lid is glued to the chip to define the microchamber.

step is approximately two seconds.

In agreement with simulations, we observed that lateral forces acting on particles (hence speed), get stronger by increasing the lid voltage peak-to-peak amplitude. Since this voltage is provided through the PCB, it is not limited by the chip supply voltage, and can be set two to three times as large as the array phases V_{phip} , V_{phim} , i.e. 6.6 or 9.9V peak-to-peak. As explained before, simulations show that the higher the lid-voltage amplitude with respect to the array voltages, the lower the height of the DEP cage. Yet, this is difficult to verify from the microscope images. Thus the lid is typically set to 6.6Vpp.

Fig. 2.17 shows how, after applying a pattern implementing an array of DEP cages, the microbeads are arranged correspondingly, and how they can be detected with the embedded optical sensors.

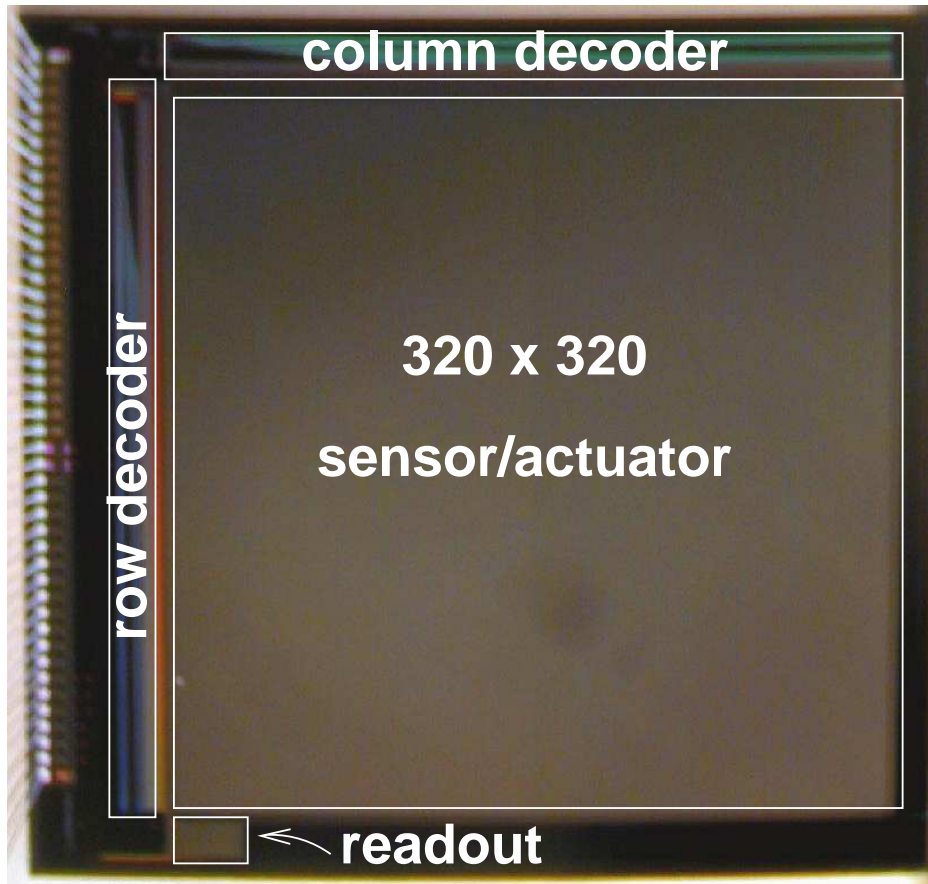


Figure 2.14: Chip photograph

Fig. 2.18 shows the mating and separation of two K562 tumor cells. Two cages trapping the selected cells (a) are first merged into a three electrode cage (b), which is then shrunk to a single electrode cage (c-d), forcing the two cells to get in contact. The cage is then enlarged (e) and the cells lose their contact, until they are finally separated again in two distinct cages (f).

Smaller particles can also be manipulated, although more than one is normally trapped in the same cage, as reported in Fig.2.19 which shows clusters of yeast.

Concerning preliminary results of capacitive detection of bioparticles, Fig. 2.20 and Fig. 2.21 show comparisons between sensors and optical microscope images. $50\mu\text{m}$ polystyrene beads are individually detected. Detection of $10\mu\text{m}$ beads, *Yarrowia lipolytica* yeasts and human erythro-

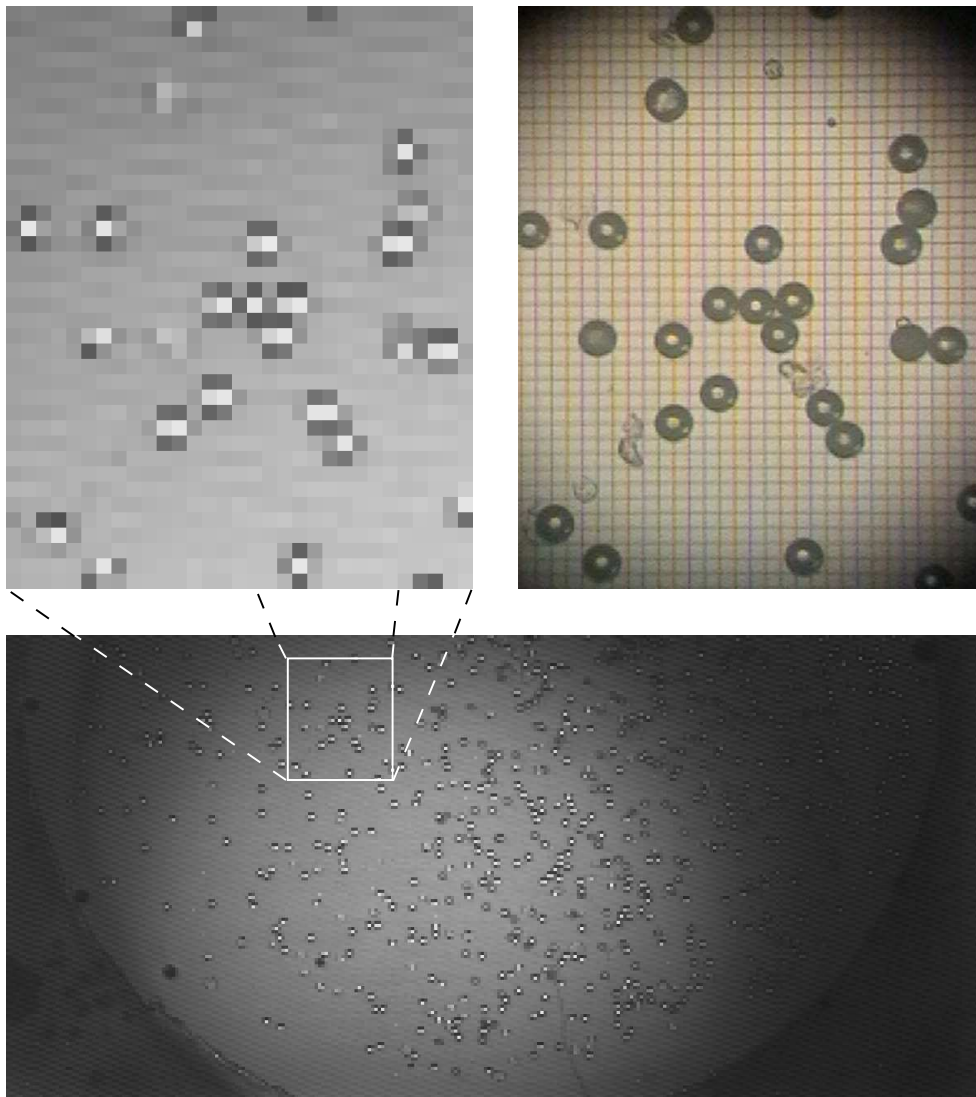


Figure 2.15: Comparison of embedded sensor (top left) and optical microscope (top right) images of $50\mu\text{m}$ polystyrene beads. In the bottom image the whole images from optical sensors is shown.

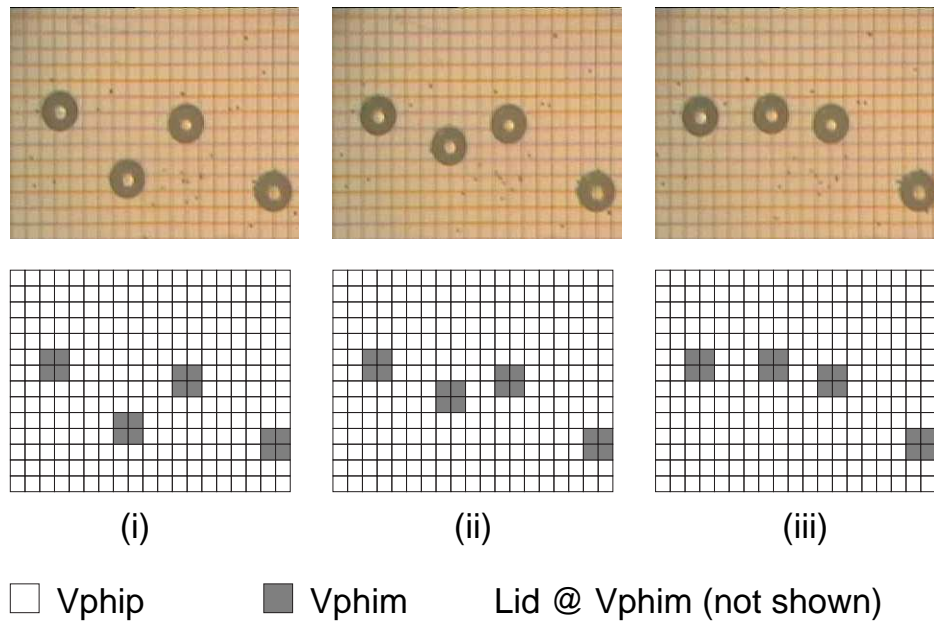


Figure 2.16: Individual manipulation of a $50\mu m$ polystyrene bead in water, $3.3V_{pp}@800kHz$ phases

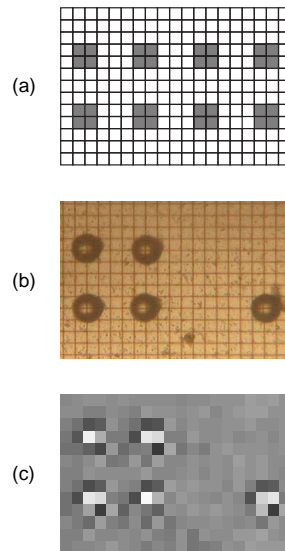


Figure 2.17: Manipulation and detection of $50\mu m$ polystyrene beads: actuation pattern (a), microscope image (b), embedded optical sensors image (c).

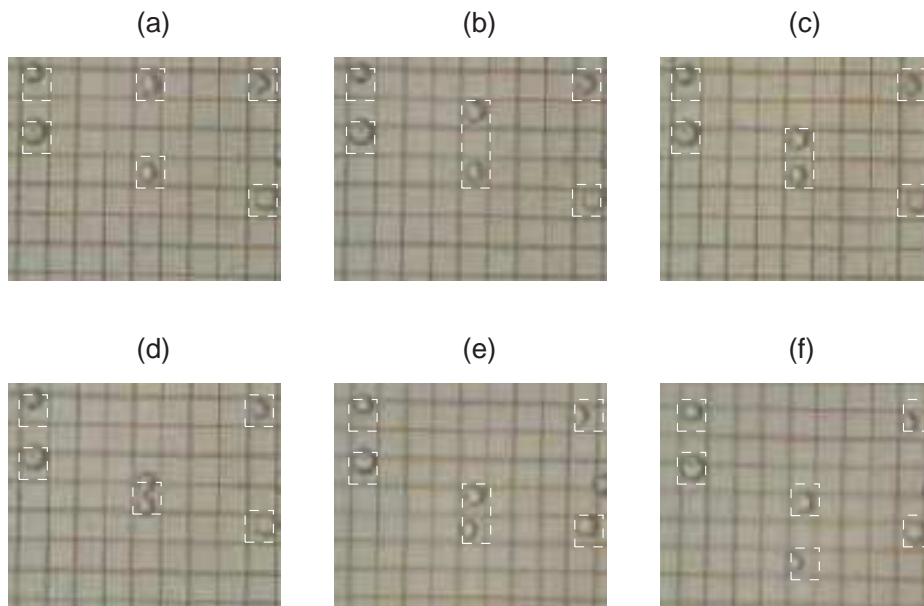


Figure 2.18: Mating (a-d) and separation (d-f) of K562 tumor cells in 280mM mannitol in water, $3.3V_{pp}@500kHz$ phases. For the sake of simplicity cage electrodes are enclosed by dashed lines.

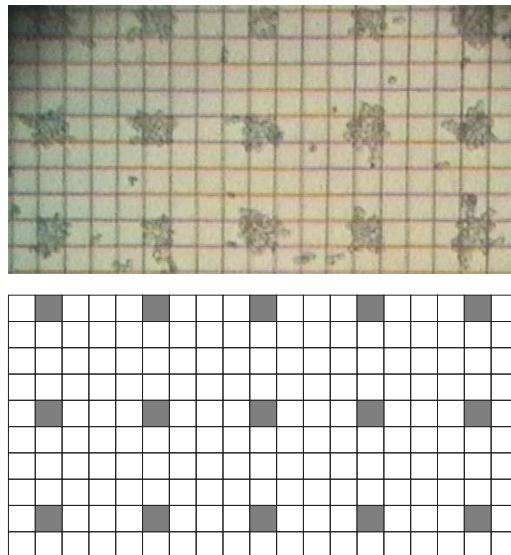


Figure 2.19: Manipulation of clusters of *Saccharomyces cerevisiae*: 280mM Mannitol buffer, $3.3V_{pp}@1MHz$ phases.

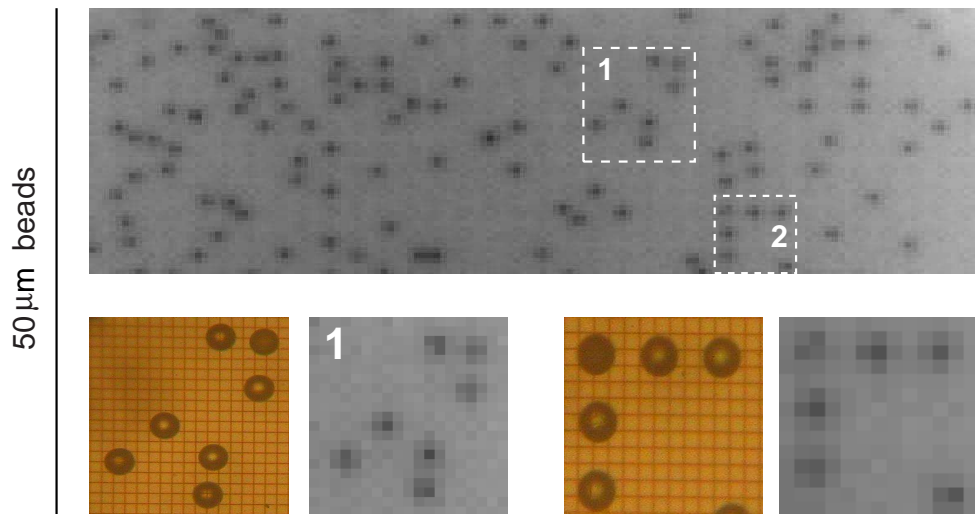


Figure 2.20: Sensor images of 50 μm polystyrene beads in a 280mM mannitol solution are compared with optical microscope images.

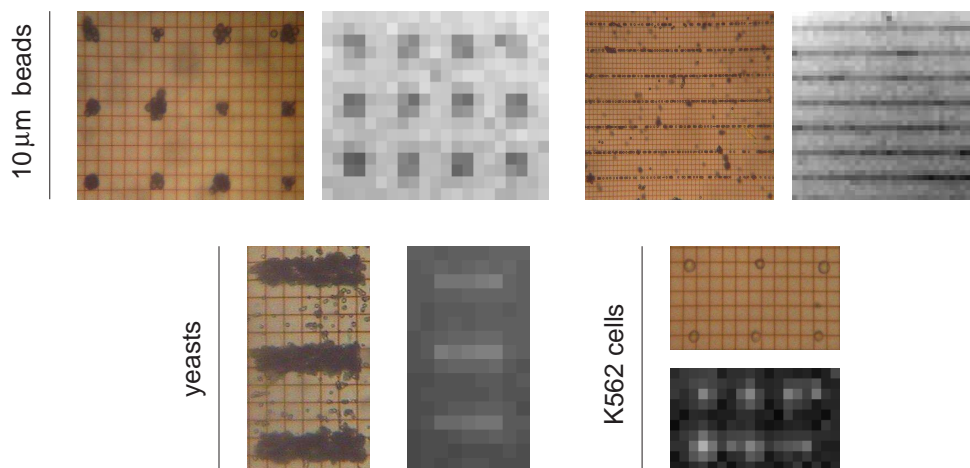


Figure 2.21: Sensor and microscope images of 10 μm polystyrene beads, *Yarrowia lipolytica* yeasts and human erythro-leukemia K562 cells in a 280mM mannitol solution. Particles brighter than the background have $\epsilon_{particle} > \epsilon_{medium}$ while darker particles have $\epsilon_{particle} < \epsilon_{medium}$.

leukaemia K562 cells is shown in Fig. 2.21. The worst case measured output voltage variation associated to particle presence is 145mV, corresponding to a SNR of 39dB and to a 0.42fF input capacitance variation. The overall circuit noise measured on the output voltage ($V_{outdiff}$) is below the 1.6mV resolution of the external 12-bit ADC, which is equivalent

to 15 electrons on the input of the charge amplifier. The feedback (C_f) and auxiliary capacitance (C_{aux}) are poly capacitors. V_{lid} is supplied externally and can range between +/- 9V. No further processing nor micromachining have been used.

Chip performance and specifications are summarized in Table 2.1.

Table 2.1: Chip specifications

Technology	CMOS 0.35 μ m 2P 3M
Die size	8 \times 8 mm ²
Array size	320 \times 320
Site pitch	20 μ m \times 20 μ m
Electrode gap	1.2 μ m
Photodiode area	2 μ m \times 17 μ m
Microchamber height	85 μ m
Microchamber volume	<3.5 μ l
Max no. of DEP cages	25600
Max no. of independent cages	12800
Power supply	3.3V
Actuation voltages	3.3V@100kHz-10MHz
Clock frequency	20MHz

2.7 Summary

The device described in this thesis holds the promise to be an enabling technology for the development of a range of innovative protocols in cell-biology, infeasible with existing analytical techniques, including:

1. Capacity of performing in parallel a large number of experiments on individual cells.
2. Possibility to detect and isolate rare-cells from a very small sample.
3. Possibility to selectively deliver controlled amounts of compounds to target cells

4. Possibility to investigate in real-time the dynamics of cell response to chemicals and to cell-cell interactions.

Some experimental results on the basic capabilities of individual manipulation and detection of particles have been presented. A more quantitative amount of data related to the experimental activity will be presented in chapter 4. The programmability of the system, afforded by the use of a microelectronic substrate, makes this device a flexible platform to create different analytical protocols just by changing software and reagents, while sharing the same hardware. In order to accomplish this, a flexible control system is needed, together with an expandable and programmable software layer. Designing such complex hardware-software system and all the related issues and constraints will be described in the following chapter.

Chapter 3

A Programmable Architecture for Lab-on-a-chip Control

As discussed in previous chapters, a new emerging field of application in electronics is the development of *lab-on-a-chip* (LOAC) devices, in order to implement programmable and automated instruments for biological and pharmaceutical analysis [68]. The important driving forces behind this revolution are the continuous advances in silicon technology. Geometry scaling makes it possible to design complex circuits the size of a cell, and thus capable of individual interactions with micro-particles. Moreover, the presence of a silicon substrate allows the functional integration of sensors, signal conditioning and processing circuits and the development of fully-electronic integrated LOACs.

Such kind of functional integration brings up many issues related to the design of control systems for these devices, which should handle the complex circuitry of the LOAC while permitting data transfers and processing. Programmable logic devices represent suitable platforms to implement control features in a flexible, scalable way.

In this chapter, the development of a flexible, expandable and programmable real-time control system for LOAC prototyping will be described. In the following sections the architectural choices regarding its design and details of the implementation on a programmable logic device will be presented. The lab-on-a-chip described in previous chapters will

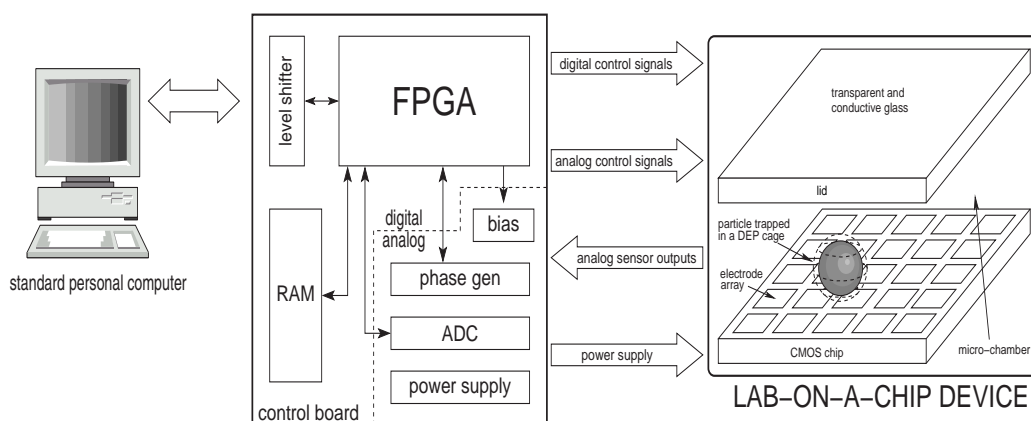


Figure 3.1: A block diagram of system architecture.

be taken into account as a case study, and some experimental results will be shown.

3.1 System specifications

Our system (Fig. 3.1) controls the silicon LOAC consisting of an array of more than 100,000 embedded sensors and actuators, based on dielectrophoresis (DEP) and able to detect and individually manipulate more than 10,000 particles, as described in chapter 2 and in [51]. The LOAC is a CMOS chip mounting on its top a microfabricated glass lid, forming a micro-chamber delimited on the other side by the chip surface. (Fig. 3.2). Cells and microorganisms in a suspending medium can be injected in the device through a microcapillary. By individually programming the voltages applied on a bidimensional array of electrodes, cells can be dragged along the chip surface with DEP forces. Embedded sensors may detect presence, position and even distinguish between different species of particles over the surface, relying also on their response to DEP forces.

We aim to design a generic hardware-software platform for real-time control and testing of LOACs in order to support tasks such as single cell sorting and detection, with possible applications in the screening of compounds and in cell-to-cell interaction studies.

The LOAC architecture is based on a bidimensional 320×320 array of micro-sites. Individual addressing and control of every single site is a key feature of the device and has to be supported. At this purpose, as each micro-site embeds both sensing and actuation circuitry, an appropriate set of analog and digital signals has to be provided in addition to addressing. Particle manipulation by means of DEP happens by writing the static RAM cell present in each micro-site, to switch the voltage applied to the corresponding electrode between two counter-phase sinusoidal waves.

Different kinds of sensors can be integrated in the LOAC and different sensing techniques are feasible. Our system must efficiently deal with them and with future implementations of the device.

Optical sensors such as CMOS photodiodes can be used to detect the “shadow” of particles lying on the chip surface or the emitted light e.g. by fluorescence or chemoluminescence [51]. In order to achieve the required degree of precision and noise reduction (e.g. due to jitter) very accurate and uniform timings are required while integrating optically generated charge. Impedance sensing is another suitable technique for particle detection [52]. Cells located on a micro-site will affect the value of the coupling capacitance between underneath electrodes and the lid. By applying a voltage pulse on the lid a charge amplifier will return a measurement of such capacitive coupling by detecting the integrated charge. Precise timings of such voltage pulses are required for physical reasons related to the LOAC. Impedance sensing may be also carried out with AC measurements. When sinusoidal signals are applied to the LOAC the integrated

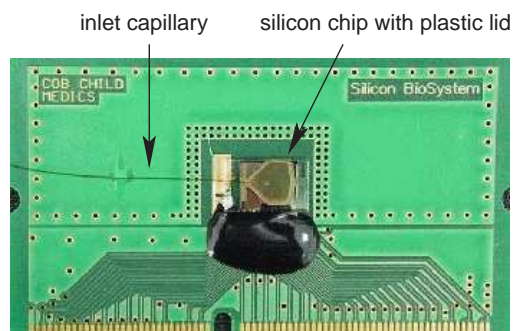


Figure 3.2: The lab-on-a-chip

amplifier will output a sine wave whose amplitude and phase are a function of the particle's impedance.

Data processing and continuous data acquisitions are general features which may also be required to extract significant parameters while these and other particular sensing schemes are in progress.

Timing constraints can be extracted from application specific requirements. Sensor arrays of up to 1024×1024 (=1M) elements should be supported. As particle motion time constants are in the order of seconds, a frame rate of about 1 frame/sec is sufficient to represent the evolution of the LOAC status. Hence addressing, readout and storage from any single sensing element must be carried out in no more than $1\mu s$. All the signals used to control the involved units (e.g. addressing, sensors and memory control) are required to switch in a given sequence and it may be assumed that about 10 sequential commutations of the control signals can drive the involved units. Therefore, the required timing resolution for digital control signals is about 100ns. Furthermore, being the maximum frequency of the AC signals used to deploy DEP forces in the order of 1MHz, the sampling of these signals is constrained according to Shannon's theorem. At least every 500ns an ADC should be driven and the output data stored in system memory. A 20MHz RISC microprocessor may execute about 10 instructions between two subsequent samples, which is enough to perform the required tasks.

In conclusion, the necessary timing resolution for digital control signals has to be equal to or less than 100ns.

3.2 Design approach

Given the above system specifications, the presence of a microprocessor core allows general purpose data processing, storage and transfers with a good degree of flexibility.

The choice of a RISC microcontroller results in a simpler hardware structure and allows for user-friendly software development environments based on the C language. The data-width of the microcontroller

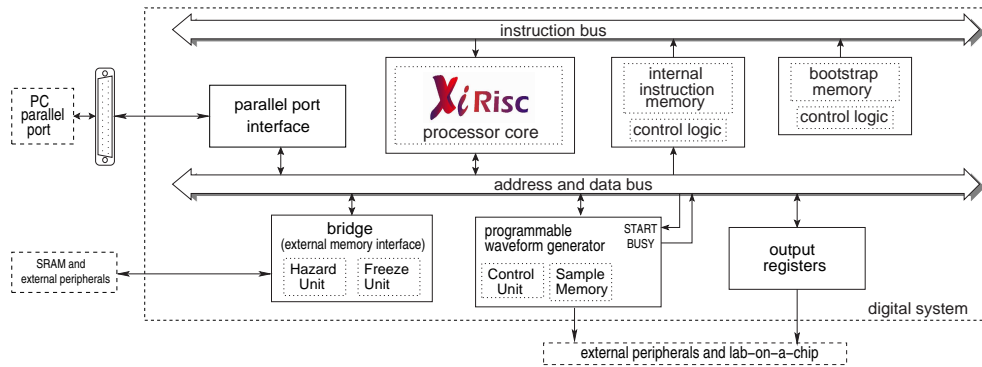


Figure 3.3: A block diagram of the digital part of the developed control system.

and memory hierarchy structure are important parameters affecting system architecture performance. The memory hierarchy of the whole system should be carefully tailored to system specifications. A cache for executable code, although increasing the overall performance, will not meet our timing requirements because of the unpredictability in the occurrence of cache misses. A very precise timing resolution is mandatory when sensors collect data from the microchamber. So on-chip memories become suitable candidates to store and efficiently access code. Nevertheless, being on-chip memories a limited resource, the system may deal with larger programs with code overlaying techniques.

Given the above real-time specifications, a standard microcontroller with an operating frequency compatible with the printed circuit board (PCB) design may not be able to generate the control signals at the required data rate. Each typical digital control waveform may be composed of up to hundreds of independent samples. The values of the samples that should feed the LOAC can neither be read fast enough from a memory nor computed by the ALU before being output.

An FPGA-based architecture was chosen for our intent instead. The main reason of this choice is that commercial FPGAs may embed application specific logic, the microprocessor core and the digital components of the system in a single chip.

The implementation of our control system as a *system-on-a-programmable-chip* (SOPC) offers consistent advantages in terms of

- synchronization
- reconfigurability
- reprogrammability

Synchronization is a critical factor for our LOAC control system. The strict timing requirements suggest a synchronous design, composed of different specific units, the microprocessor core and high-speed on-chip memories. In a multiple device context the problems related to clock distribution would be significant. Having all the design units collapsed in a single FPGA rather than in a collection of discrete components greatly simplifies the PCB design, decreases the board area and results in higher speeds in elaboration and communication. It also enables a completely asynchronous board design, sparing the concern for issues related to clock distribution over the PCB.

Reconfigurability is as a matter of fact the real key feature of our system. Hardware reconfigurability can easily make the system compliant with new needs in terms of device control and permits designers to keep all the control logic out of the silicon LOAC. Furthermore, different I/O interfaces (e.g. USB and IEEE1284) can also be implemented at the only cost of a hardware reconfiguration. The system is thus extremely flexible.

Reprogrammability extends the reconfigurability paradigm at a software level. The use of a microprocessor core rather than a specific hardware unit makes it possible to develop new control techniques just with different algorithms and to accomplish under software control all the tasks which are not subject to real-time specifications.

3.3 System architecture description

A block diagram of the digital part of the developed system is shown in Fig. 3.3. The core of the system is XiRisc, a parametric and configurable processor based on an extendible instruction set RISC architecture [70]. Separate address spaces are provided for instructions and data. Small amounts of memory have been allocated in the FPGA (as RAM and ROM)

to store and access data and code with zero wait states. A bidirectional parallel port interface compliant with the PS/2 standard was included to communicate with an attached PC when the system is not in time-critical phases of execution.

During system initialization the microprocessor runs a *Basic I/O System* (BIOS) program stored in the startup ROM. Its tasks are to perform the necessary hardware initializations, to provide some low-level communication routines and to download a user program from the parallel port interface into the code RAM. Since code address space is read-only, a dual port memory facing both instruction and data bus was used at this purpose. When the bootstrap sequence is complete the microprocessor begins the execution of the user program.

An FPGA-based solution was chosen in the early stages of the design and the whole system was described using a synthesizable VHDL model, without targetting the design to any specific technology. A parametric and general approach was maintained, so that by simply changing constant definitions in the HDL code the whole system can be configured in terms of data width, address space and properties of specific units.

Special care was used when partitioning system complexity between hardware and software. When the microprocessor performance proved to be insufficient application-specific hardware units were designed, such as a Programmable Waveform Generator (PWG) and a Bridge connecting our SOPC to the external peripherals. However external devices such as an array of fast static RAMs, a digital frequency synthesizer, DACs and ADCs have been required. DACs and ADCs interface the digital core of the system with the analog parts, handle data from sensors and bias external circuitry.

As a precisely timed communication with a PC through the I/O interface proved to be impossible due to the non-real-time nature of common PC operating systems, on-board external static RAMs are used to temporarily store the sensors outputs when acquiring data because of the limited size of on-chip FPGA memories.

manipulation, and other external components have to be mapped in our address space. The choice of 24 bits for address width was then considered optimal. Furthermore, we decided not to include in XiRisc processor configuration multipliers and hardware iterators, as they would not bring significant advantages, while occupying a relevant portion of FPGA resources. For the same reason the maximum shift amount was reduced to 16. Nevertheless, all the missing features are implemented with software emulations provided with extensions to the software compilation toolchain.

3.3.2 The Programmable Waveform Generator

The Programmable Waveform Generator (PWG) is a hardware unit which can output 16 independent digital signals during each clock cycle. Its main components are a Sample Memory, where up to 256 digital samples of each signal can be stored, and a Control Unit. The Control Unit may slow down the output data rate and define the number of samples composing the output waveforms. The PWG interacts with the XiRisc

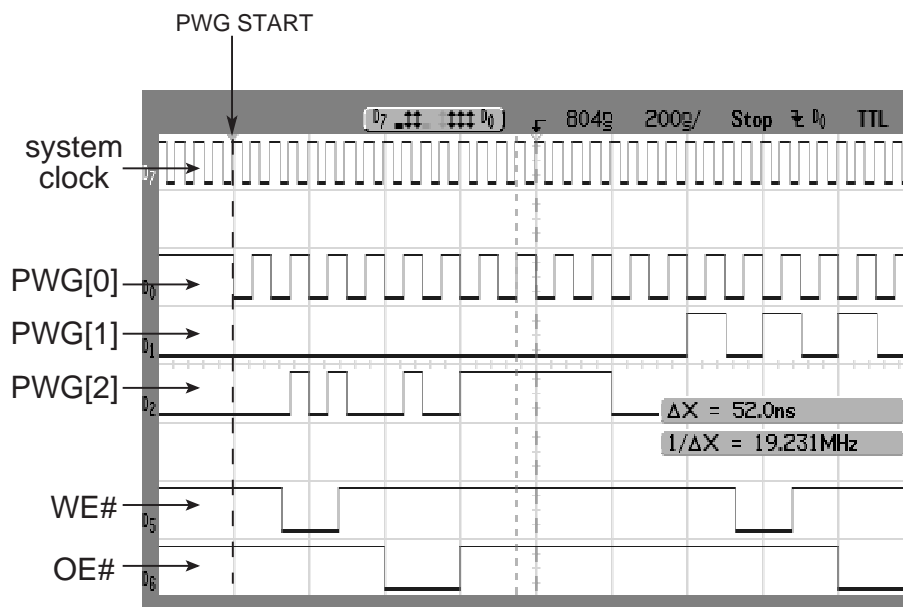


Figure 3.5: Acquired digital waveforms. Bus activity (OE#, WE#) shows that the processor is continuing program execution while the PWG is driving some control signals (PWG[0..2]).

processor mainly with the START and BUSY signals. The START signal begins the output of the digital waves. While the PWG is performing its task the microprocessor is able to carry out other jobs (Fig. 3.5) and may poll the BUSY signal to detect if the PWG output cycle is complete.

3.3.3 The Bridge

A Bridge was designed to interface the internal system bus to an external bus with asynchronous and significantly slower peripherals. Its main components are the Freeze Unit and the Hazard Unit. The Freeze Unit handles the necessary wait states for each external slower device. The Hazard Unit was designed to prevent possible conflicts during external bus access. The internal bus features two synchronous separate channels for input and output data. As the external bus has only one asynchronous bidirectional channel, if the microprocessor issues subsequent load and store instructions an electric conflict may occur, since external peripherals will drive data lines one bus cycle after the read request, while a following write instruction present in the pipeline may be trying to do the same. The Hazard Unit prevents such situations by freezing the microprocessor and serializing the involved bus cycles. In this control architecture, code memory is mapped onto dedicated banks internally to FPGA, and also on external memory, in banks shared with data memory. Internal memory (8kB) will be used for critical code, while the shared portion will be used for code which has no real-time constraint (e.g. controlling an LCD display for debugging).

3.3.4 Software

Many tasks of our system are completely software driven, such as individual programming of each micro-site of the LOAC for cell manipulation. Specific registers connected to the LOAC and to PCB components were mapped in the I/O space at this purpose. Micro-sites in the LOAC can be accessed for both actuation and sensing in a random access mode. This is done by first storing the value of the selected row or column in

3.3. System architecture description

specific output registers of the SOPC and by subsequently driving the corresponding control signals. The whole LOAC array can be programmed before particles have significantly changed their position, due to the relatively longer time constants involved in their motion. Communication with a PC is another task controlled by software, when no other critical tasks are in progress and the CPU can waste cycles polling the I/O interface.

Software development, simulation and profiling for the XiRisc instruction set are supported by a specific release of the open-source GNU Compiler Collection (GCC) toolchain [69]. Anyway, the compiler toolchain had to be extended in order to suit the specific configuration of our processor.

Besides this low-level software layer, a full set of tools and utilities was designed at PC level to allow the user to interact with the systems.

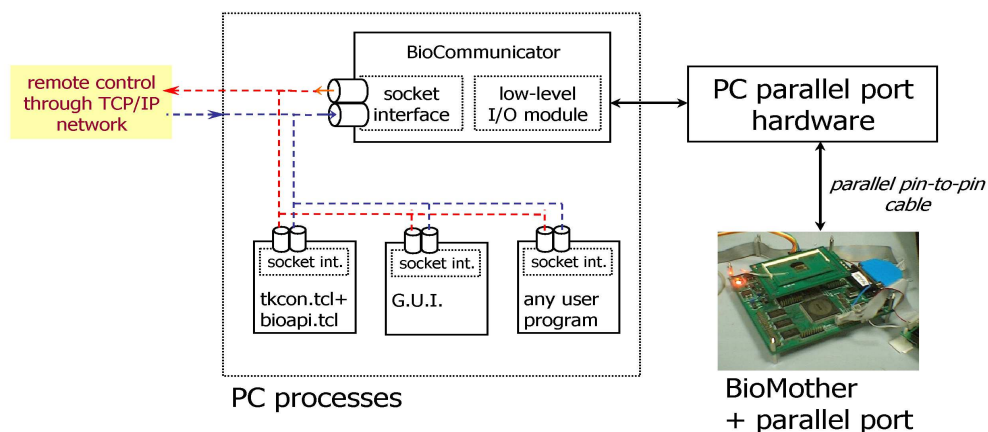


Figure 3.6: Software architecture block diagram

This suite of tools was named BioTools, and is based on open-source software. BioTools mainly implement an API (Application Programming Interface) which is made available to users through a Tcl/Tk environment. Complex protocols are built up by using Tcl language, while other functionalities ranging from low-level control of the device to established protocols are accessed through the command line or a graphical interface.

3.4 System implementation



Figure 3.7: The prototype board.

The presented system has been implemented on an Altera EPF10K200S device belonging to the Flex 10KE family. The operating frequency is 20MHz, fully compliant with the required timing resolution of 100ns or less in digital signal switching. No further speed optimizations were pursued being the constraints widely satisfied.

The SOPC VHDL description has been synthesized on the selected target device, taking advantage of peculiar architectural features of the FPGA such as embedded memory blocks, optimized carry chains and low-skew internal lines. Resource utilization statistics are shown in Table 3.1. Free device resources can be used for future system expansions just by means of hardware reconfiguration.

The high percentage of used memory blocks (*Embedded Array Blocks* (EABs) according to Altera Flex 10KE notation, whose size is 4096 bits) is mainly due to the need to have the largest possible internal instruction

memory. The EABs were used to store instructions (8Kb), data (2Kb), and the PWG samples (512 bytes). Code memory is also mapped on a 32kB external bank, shared with data.

An implementation of the register file on EABs requiring only 52 logic cells (LCs) and 4 EABs instead of the actual 2517 LCs and 744 flip-flops (FFs) was also evaluated, but the great availability of LCs and the need of the largest possible instruction memory suggested to keep the actual hardware configuration.

A prototype PCB mounting the Altera device, all the mentioned external peripherals and the needed circuitry has been created to test the experimental LOAC (Fig. 3.7). A flash configuration device (Altera EPC16QC100) was included in the board to automatically download the configuration bitstream into the FPGA at power-up. After the tests the system implementation resulted fully functional and compliant with the required specifications.

Successful experiments of manipulation and detection of human erythro-leukaemia K562 cells and polystyrene micro-beads have been carried out with the LOAC, as shown in Fig. 3.8. Biologists have been trained to use the developed SOPC-based system in order to perform micro-manipulation protocols with the described LOAC.

Table 3.1: Resource usage summary for the FPGA implementation

Unit	LCs	FFs
XiRisc Processor	4030	976
PWG*	132	80
Parallel Port	70	33
Bridge	235	90
Total SOPC Resources	4904	1298
*uses also 1 EAB resource		
Used pins: 150/182 (82%)		
Used EABs: 94208/98304 (95%)		
Altera EPF10K200S Logic Elements: 9984		

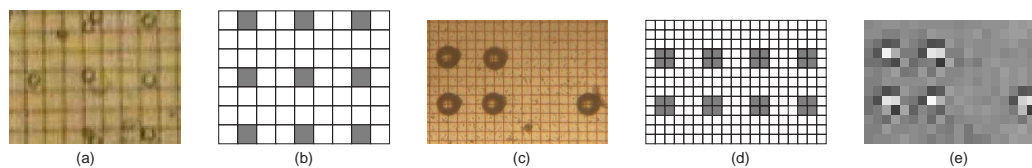


Figure 3.8: Manipulation of human erythroleukaemia cells (K562) and polystyrene beads by means of DEP. The positions of the trapped particles shown in microscope images (a), (c) and in the image acquired with embedded optical sensors (e) match the applied programming patterns (b), (d) consisting of DEP cages with extensions over 1×1 and 2×2 electrodes of the LOAC.

3.5 Summary

The design and the implementation of a SOPC to control an innovative LOAC for cell manipulation and detection have been illustrated. Emphasis has been put on system-level requirements and constraints in design imposed by the LOAC itself and the main architectural choices have been explained with greater detail. The implementation of such a system allowed to design an application independent LOAC, earning much in system flexibility and future expandability and allowing an easier design of the CMOS LOAC. The presented SOPC has been successfully implemented in a FPGA device, and tests have been performed with a prototype PCB and the LOAC. The working prototype allowed us to validate the technology of such innovative CMOS LOACs and to demonstrate the feasibility of flexible and expandable microprocessor-based digital control systems for this kind of devices.

Chapter 4

Experimental Results

In this chapter, the main results of the experimental activity performed on the prototypal CMOS devices will be described and discussed, in view of the realization of significant protocols for cell analysis, manipulation and recovery. This chapter will mainly focus on these main topics:

- cell manipulation and recovery
- optical detection of cells and bioparticles
- capacitive detection of bioparticles.

Concerning manipulation of cells, the more significant experiments will be described. The main topics will be the separation of different cell populations, manipulation and recovery of few selected cells, feasibility study of experiments of cellular interactions. These kinds of experiments were held jointly and with the support and activity of the partners of University of Bologna within the MeDICS project, CEA-DSV, CEA-LETI, INSERM (Grenoble, France) and Silicon Biosystems (Bologna, Italy).

In the area of optical sensors, results obtained in cellular imaging will be presented, together with the characterization of the spectral response of the detectors, in view of applications using fluorescent markers.

The discussion on capacitive detection of bioparticles will first describe a more accurate circuitual model due to presence of liquid solutions over the chip surface. Measurements validating the proposed equivalent circuit

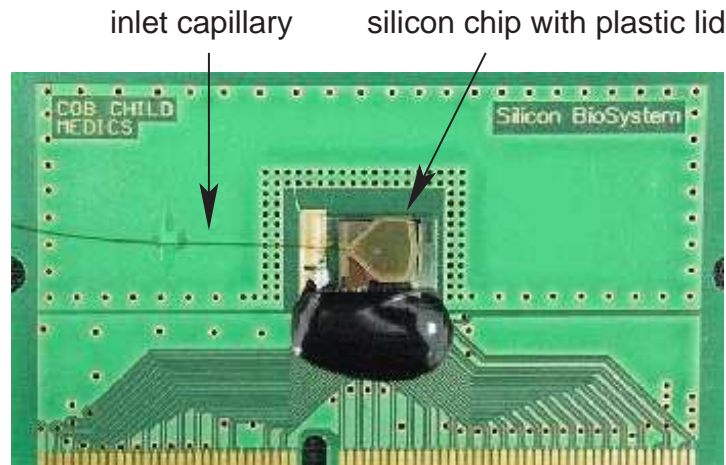


Figure 4.1: Microfabricated implementation of the microchamber containing samples on the CMOS device

model will be analyzed. Then results obtained in detection of living cells or other particles at microscopic scale will complete our analysis.

For both kinds of sensors the theoretical sensing limits will be analyzed and compared with experimental data from the prototypes.

A synthesis of all the results of the MeDICS project, from electronic and system design, packaging issues to biological validation, and scientific publications is included in the publicly available final report [1], addressed to the European Community.

4.1 Experimental setup

Two types of prototypes were developed. The first type of prototype was called MEDA (Fig. 4.1). The MEDA prototype is a completely packaged chip with a structured lid (ITO or SU8 on glass), glass capillary connections and a conductive glue electrical connection between PCB and the lid [71] [72].

The second type of chip was named *Bricolage* (BRIC), because of the relatively homemade packaging which can be mounted and unmounted (Fig. 4.2).

Besides, some prototypes were realized by processing the silicon dies with plasma etching techniques. The job was performed by our partners at LETI (Grenoble, France). The purpose of this kind of post-processing was to decrease the thickness of the silicon nitride passivation layer of the CMOS process. The passivation layer acts as a serie capacitance, which may significantly reduce the electric field in the sample, thus affecting effectiveness of DEP actuation. Two kinds of device were fabricated: the MEDTs, consisting in a device with a thinner passivation layer and the MEDUs, where the silicon nitride was completely etched away and the higher metal layer is directly in contact with the samples.

The packaging units comprise a double sided tape punctured with a hole to delimit the chamber, an ITO covered polycarbonate (or glass) planar lid with inlet holes and a copper braid to ensure electrical connection between PCB and lid. The mounting is made just before use and elements are changed if necessary during the course of the experiments. The second packaging technique proved to be more effective and was preferred during most of the experiments. A more detailed view of the complete device is shown in Fig. 4.2.

The size of the hole was determined by a standard paper perforator and resulted in a heavy loss of exploitable electrode surface. A prefabricated double sided tape cut by laser to our specifications was also used, by prepositioning it onto the glass lids. We simply had to manually position this assembly over the silicon surface.

4.2 Biological validation of the device

4.2.1 Description of the particles

The prototypal devices were tested with different types of particles, ranging from polystyrene micro-beads to living cells like for examples red blood cells. The experiments aimed to characterize the reliability of manipulation of different cells or particles, in different electric field configurations. The electric field can be mainly programmed in terms of am-

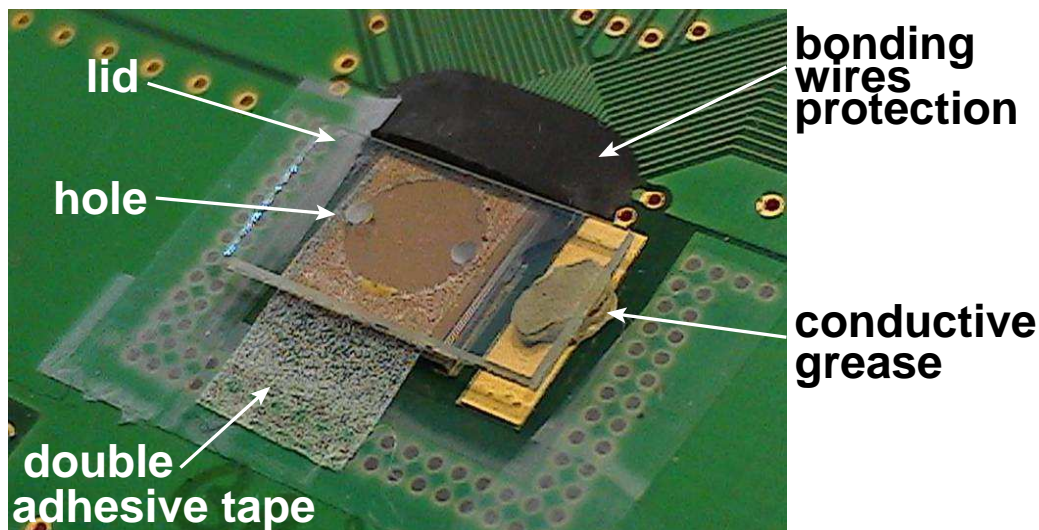


Figure 4.2: The microchamber containing the samples to be inspected is built with a pierced piece of double-adhesive tape acting as a gasket, and a conductive glass lid. Samples are injected through holes in the glass. The contact on the lid is made by depositing a small amount of conductive grease.

plitude and frequency. Micro-particles vary in terms of composition (e.g. polystyrene or organic). In relation to dielectrophoresis, each particle is characterized by a different volume, ϵ and σ . In addition, in the suspending medium ϵ and σ are far from being constant, because cell populations alter these values by releasing ions or their cellular contents in case of cell death. These issues make immediately understand how a characterization of the behaviour of particles can improve the design of specific analysis protocols.

Within the experiments two categories of bioparticles have mainly been used, and are described below.

Micro-beads. We worked with beads of various diameters. We mainly used $3\mu\text{m}$ diameter beads, while $15\mu\text{m}$ diameter fluorescent beads were used in separation experiments (e.g. sorting of fluorescent versus non fluorescent particles). Particles of $50\mu\text{m}$ diameter were also used.

Living cells. Most experiments were carried out with non adherent hu-

man cell lines such as T lymphocytes (Jurkat cell line) and K562 erythroleukaemia cells. For both types, we had tested their survival and proliferation rates in mannitol, and other buffers. Many experiments were also carried out with freshly collected blood on red blood cells (RBCs).

4.2.2 Manipulation of blood cells

Manipulation of blood cells is an application of interest in cell biology, which could benefit from lab-on-a-chip technology. For example separation of different cell populations is a useful task to perform for specific biological analyses that could be performed with nDEP in lab-on-a-chip devices [75, 82].

In this case, peripheral blood mononuclear cells (PBMCs) isolated from fresh blood were chosen as a clinically relevant model to validate the final MeDICS prototype as they consist of a mixture of lymphoid cells (Lymphocytes B and T, Monocytes, Macrophages, Dendritic Cells) that can be differentiated by their cell surface markers.

The following protocol was used:

- Cells were carefully washed and suspended in the buffer
- The MeDICS hardware was connected and before cell injection a pattern of DEP cages was applied to the chip.
- Lid voltage gain and frequency of the AC fields were set (these are the main variables in determining optimal levitation conditions).
- Cells were loaded into the chamber using a micropipette, through the holes in the lid.
- Individual cells were then isolated and moved.

All cell types (cell lines and primary cells) could be organized and manipulated, as shown in Fig. 4.3. Results were reproducible and experimental success was high.

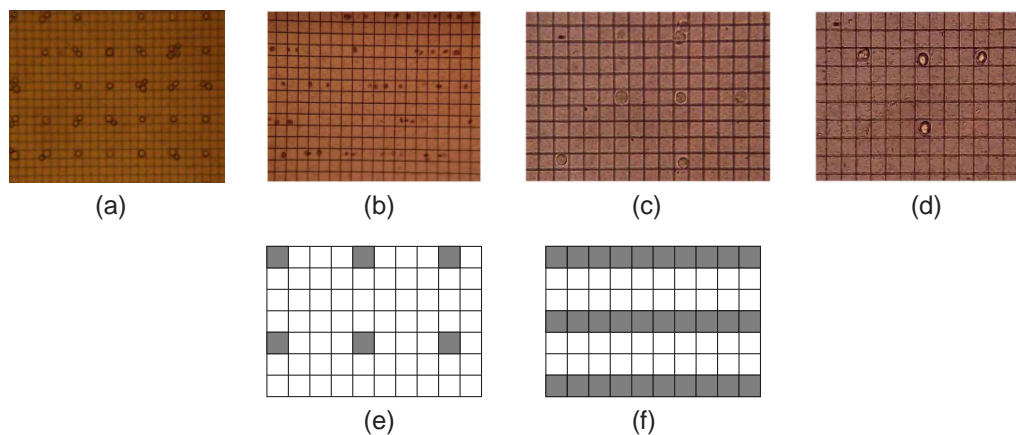


Figure 4.3: Organization and manipulation of different type of human cells. In (a) K562 cells are trapped in single electrode DEP cages, in (b) RBCs are aligned in a row pattern. Images in (c) and (d) show respectively individually trapped 221-G and RAJI cells. In (e) and (f) the patterns used to trap the cells above are indicated.

[cell images courtesy of M.Abonnenc, Silicon Biosystems]

At a frequency of 800kHz with a lid voltage gain equal to 0, cells may be reproducibly organized into the chosen grid pattern and individually moved but simulations and experiments confirmed that they are in positive DEP.

In positive DEP, cells are attracted towards regions with a higher electric field gradient. Thus, forces are stronger and push cells towards the surface, resulting in stressing conditions. Although positive DEP is not the optimum way to manipulate living cells, cell viability was evaluated under these harsher conditions.

Other experiments were performed with depassivated devices. The depassivated devices allow for negative dielectrophoresis at low field frequencies ($\simeq 50$ kHz), provided that the buffer has sufficient conductivity ($\simeq 800\mu\text{S}/\text{cm}$). A buffer with Mannitol 280mM + 6.25mM of KCl, at a frequency of 50KHz, allowed to obtain a nDEP organization with different lines of cells (K562, RBCs, WBCs), as shown in Fig. 4.3.

4.2.3 Effect of DEP on cell viability and proliferation

Different viability experiments were carried out by our partners at CEA-DSV (Grenoble, France) on K562 and PBMC cells, with field frequency of 800kHz and lid gain equal to 0. Viability was evaluated using the standard trypan blue assay, provided that a significant amount of cells could be recovered from the chip. In all cases, viability of the recovered cells was $> 80\%$ after 35 minutes of manipulation in harsh conditions.

With good viability, proliferation assays were also performed on K562 and Jurkat cells. After DEP manipulation on the chip, the recovered cells were put in a culture medium in a microplate well. Proliferation of these cells was compared to that of cells which had remained in mannitol for the same time without being submitted to DEP fields.

Proliferation and viability were also evaluated with different buffers. For each buffer, the following quantities were evaluated:

1. Cells injected inside an unconnected chip (MEDU) for a given time, in order to evaluate the intrinsic toxicity of the chip
2. Cells injected inside a connected chip (MEDU): cells were trapped in nDEP and kept in continuous motion for the same time, in order to evaluate the effects of nDEP manipulation on cell survival.

After the experiment, the sample was taken out of the chip and put in culture.

Results showed that there is no evident toxicity of the chip components and nDEP does not damage the cells. The cells could proliferate after the experiment, although the proliferation rate was slightly slower than that of cells left alone (A.Fuchs et al., 2005, submitted).

4.2.4 Characterization of motion

DEP actuation mainly depends on the electric field parameters, besides the physical properties of particles and suspending medium. Experiments were run in order to characterize the response of different cell types in

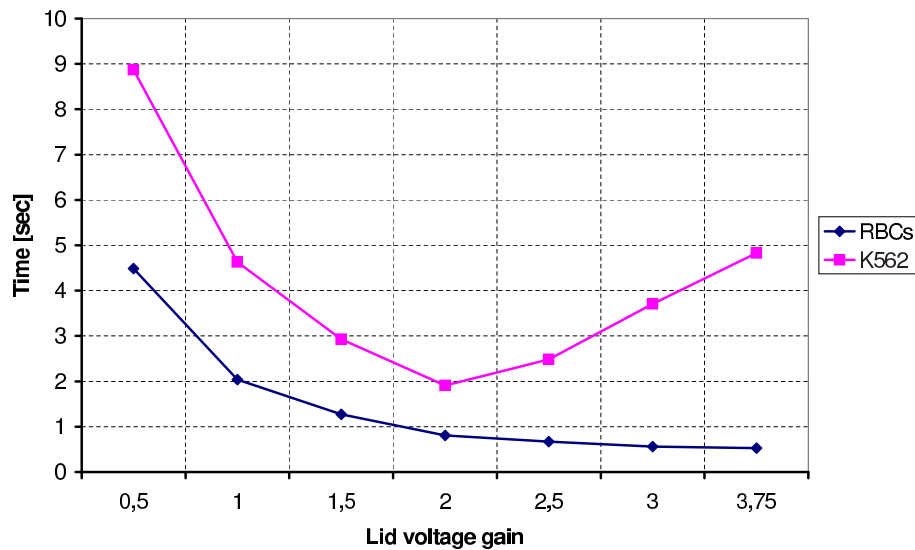


Figure 4.4: Time required for cells to move to an adjacent electrode. Data refer to individual K562 cells and a diluted suspension of RBCs. [Data courtesy of Silicon Biosystems]

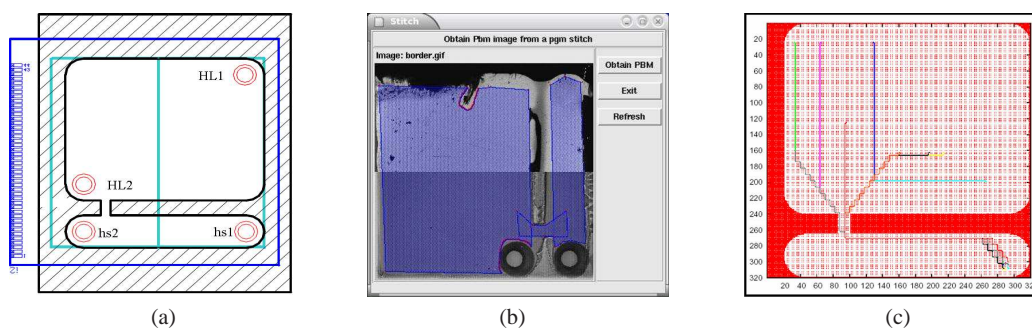


Figure 4.5: Technology for sorting and recovering specific cells. In (a) the double chamber design is shown. In (b) and (c) screenshots of the routing software are shown, respectively definition of the obstacles and definition of the route for particles.

different polarization conditions. With such characterization optimal conditions can be applied to specific cell types in order to improve reliability of protocols.

In this analysis, frequency and amplitude of the AC electric fields is fixed. The lid voltage gain is the parameter to analyze, in view of its effect on motion of particles. The experiments were performed with RBCs and K562 cells. The main results are shown in Fig. 4.4. RBCs are suspended

in Mannitol 280mM + EDTA 200 μ M. The dilution factor with respect to an initial volume of 10 μ l is 1/100. K562 are manipulated in Mannitol 280mM + KCl 6,25mM. If the lid voltage gain is excessively increased, cage height gets reduced, and K562 cells risk to get in touch with the surface and to move slower, although DEP force is stronger.

4.2.5 Routing of particles

A software algorithm for routing was developed in order to perform sorting of specific individual cells [89]. With a microfabricated design of a microchamber divided into two regions separated by a small channel, selected cells can be routed through the device in order to be recovered (Fig. 4.5). The algorithm computes the optimal path for each particle and schedules displacement steps in order to avoid collisions. Fig. 4.6 shows the router in action. Duration of the displacement of particles mainly depends on the distance between source and destination locations.

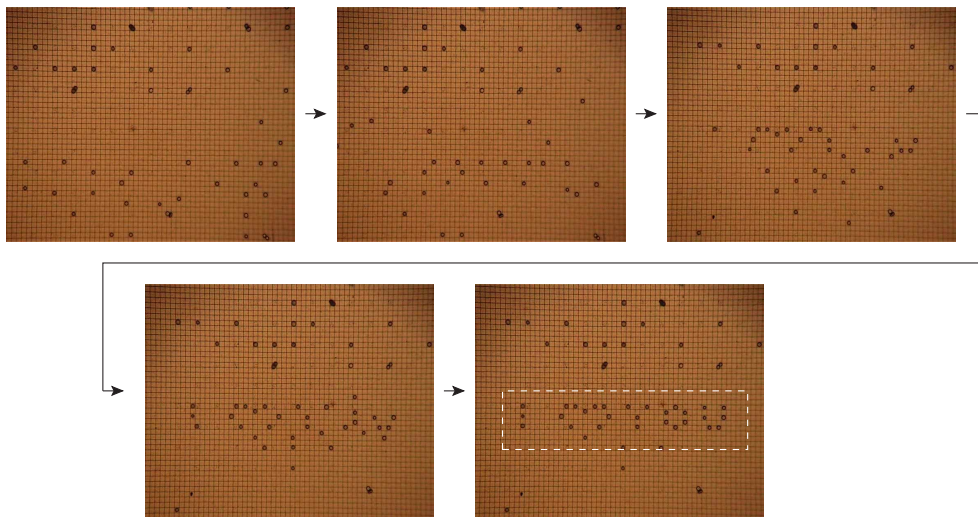


Figure 4.6: Selection and routing of few selected individual cells. Cells are routed to their final destination, composing the smallest Valentine ever.

4.3 Optical sensing

4.3.1 Optical detection of bioparticles

In this section the main results obtained in detection of microbeads or blood cells will be presented. The following images demonstrate the proof of concept of ideally software-automated analysis protocols: optical sensors can detect presence of particles and keep track of their positions (Figures 4.7, 4.8, 4.9, 4.10). In these experiments, particles at different concentrations were injected in the devices, manipulated by means of DEP forces, and images were acquired with the embedded photodetectors. Particles were either displaced or concentrated.

4.3.2 Spectral response of the photodiodes

The aim of the experiments was to characterize the photodiodes response when stimulated by light at specific wavelengths, spanning from infra-red up to ultra-violet. Characterizing the spectral response of the optical sensors may be useful for use with specific fluorescent markers. Each marker emits fluorescent light when it is stimulated by impinging radiation. Stimulation and emission wavelength are specific physical properties of each marker. Fluorescent markers can be bound to specific molecules, like for example antibodies. By exploiting the properties of the antigene-antibody binding, fluorescent markers can be applied to specific types of cells in order to distinguish among different populations. A favourable condition for detecting specific cell lines would be that of an attached fluorescent marker emitting light at best sensitivity wavelengths, upon stimulation at no-sensitivity wavelengths.

A spectrophotometer was used to characterize optical sensors. It can emit light at a specific given wavelength with an internal monochromator. The device with optical sensors was placed in front of the beam light. The setup of the whole thing is shown in Fig. 4.11

Acquisitions were performed in the 325nm-800nm range. Sensing parameters such as integration time, gain and offset in the readout stage have

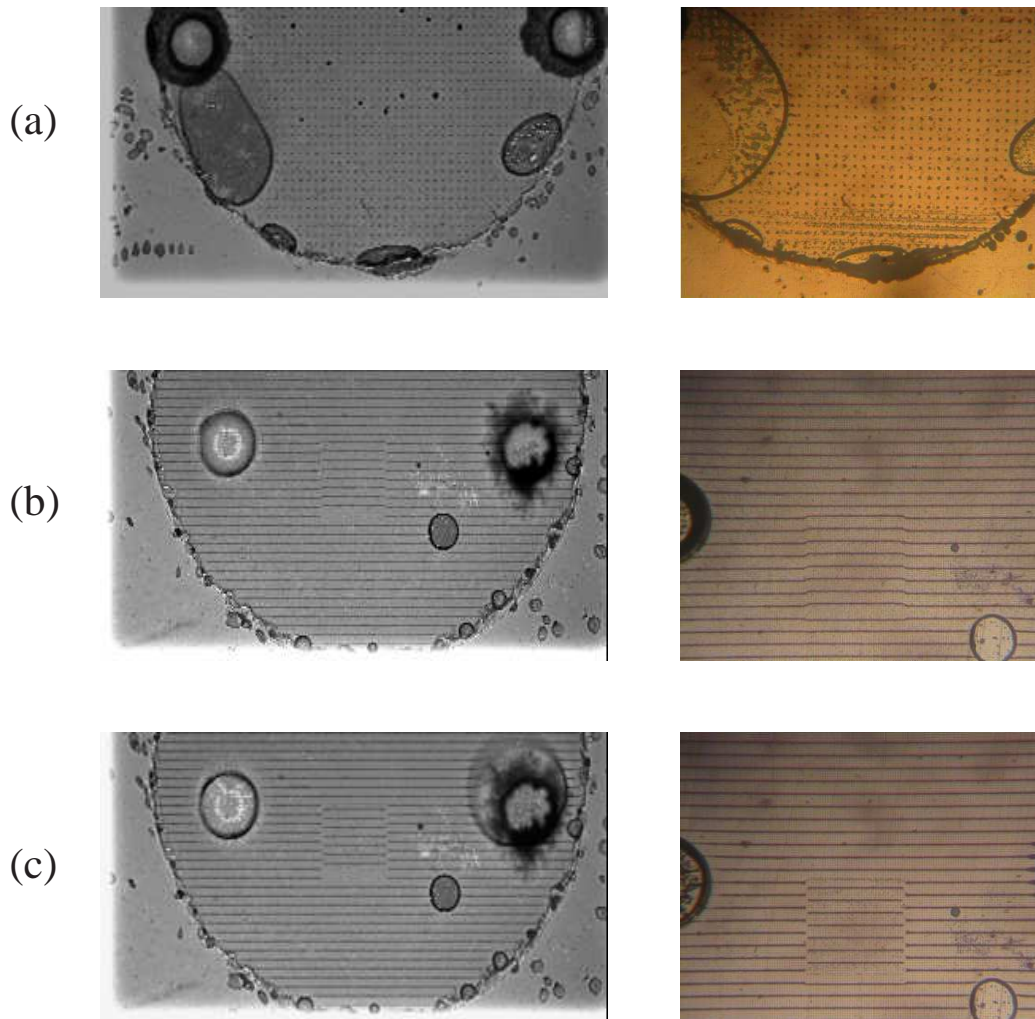


Figure 4.7: Comparison of optical microscope (on the right side) and embedded optical sensors (on the left) images of $3\mu\text{m}$ red beads suspended in Mannitol 280mM and organized in regular patterns at 500KHz, gain 2. Beads are displaced and detected at each step.

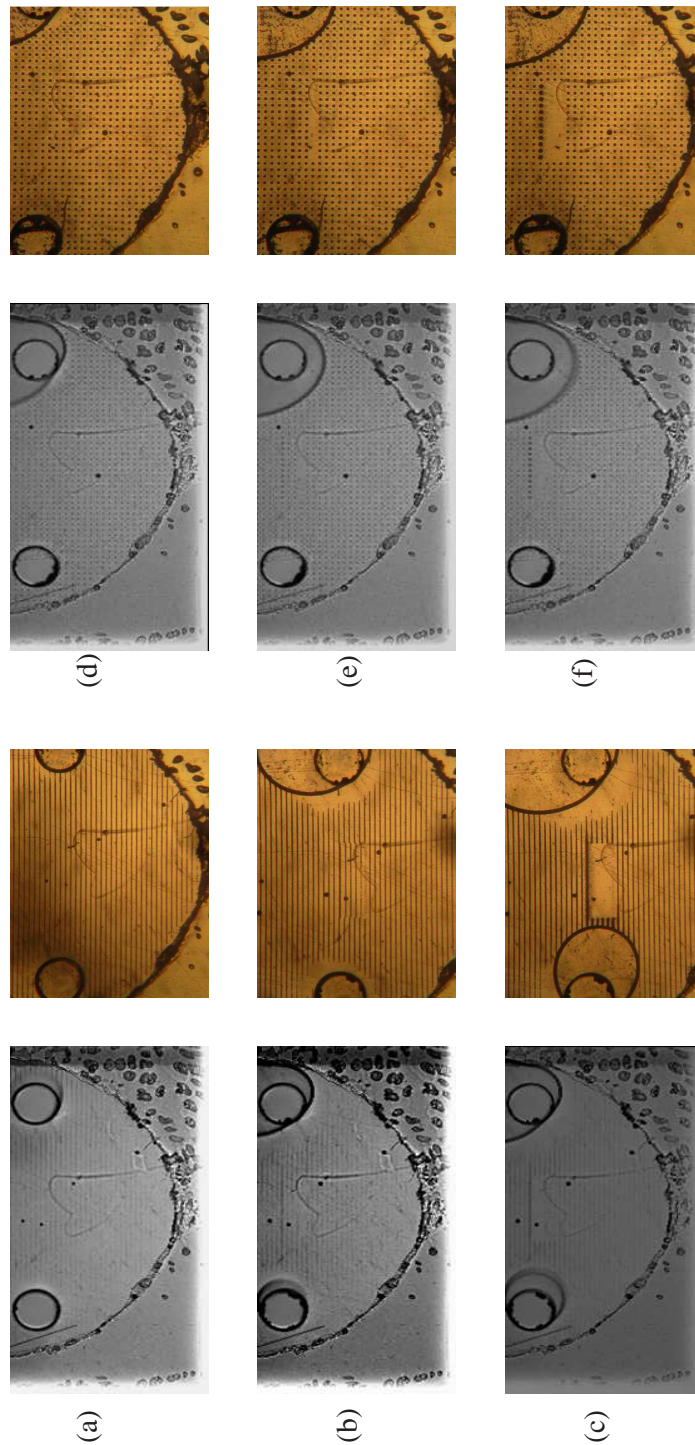


Figure 4.8: Comparison of optical microscope (right) and optical sensors images (left) of red blood cells in Mannitol 280mM + 200 μ M EDTA at the concentration of 10.106 cells/ml. Frequency 50kHz, gain2, MEDU device. Cells are trapped in regular patterns and manipulated. Photodetectors keep track of the positions of displaced cells.

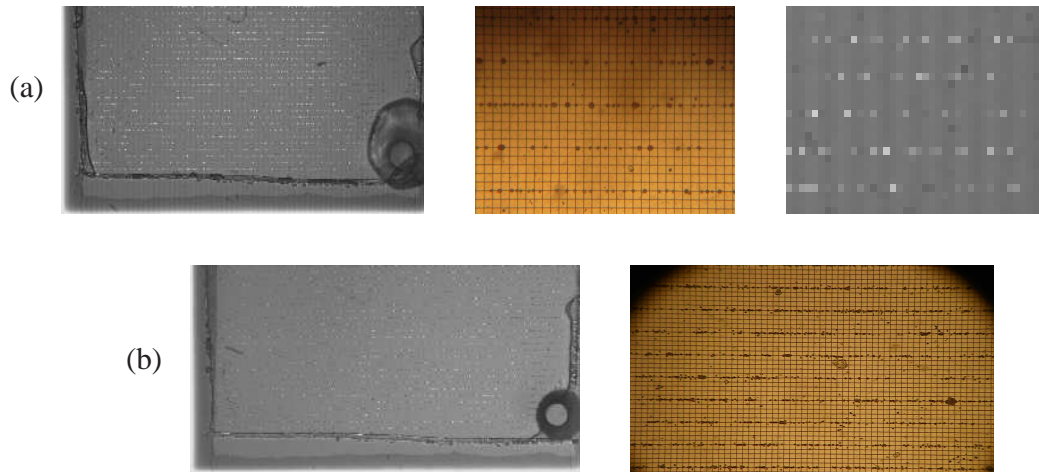


Figure 4.9: Comparison of optical microscope (center image in (a) and right image in (b)) and embedded optical sensors images of red blood cells suspended in Mannitol 280mM + 200 μ M EDTA at low concentrations. Frequency 50kHz, gain 2, MEDU device.

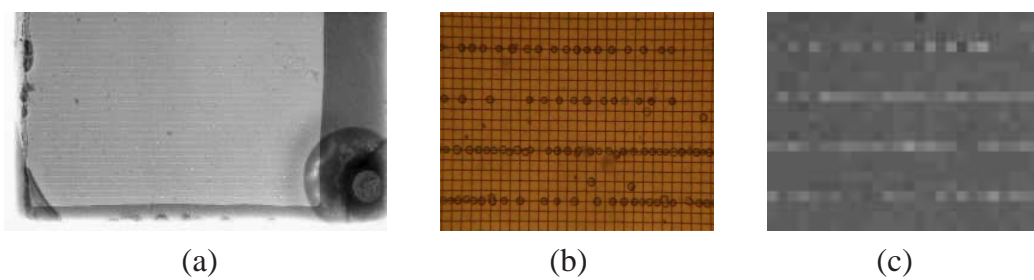


Figure 4.10: Comparison of optical microscope (in (b)) and embedded optical sensors (in (a) and (c)) of K562 cells suspended in Mannitol 280mM + 6,25mM KCl in a MEDU device at a frequency of 50kHz, gain 2.

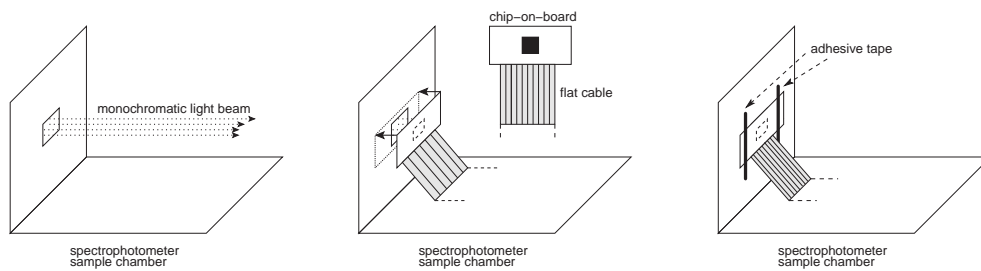


Figure 4.11: Schematic representation of the setup of the experiment.

been chosen so that the brightest pixel did not saturate any stage. The spectral response is shown in Fig. 4.12.

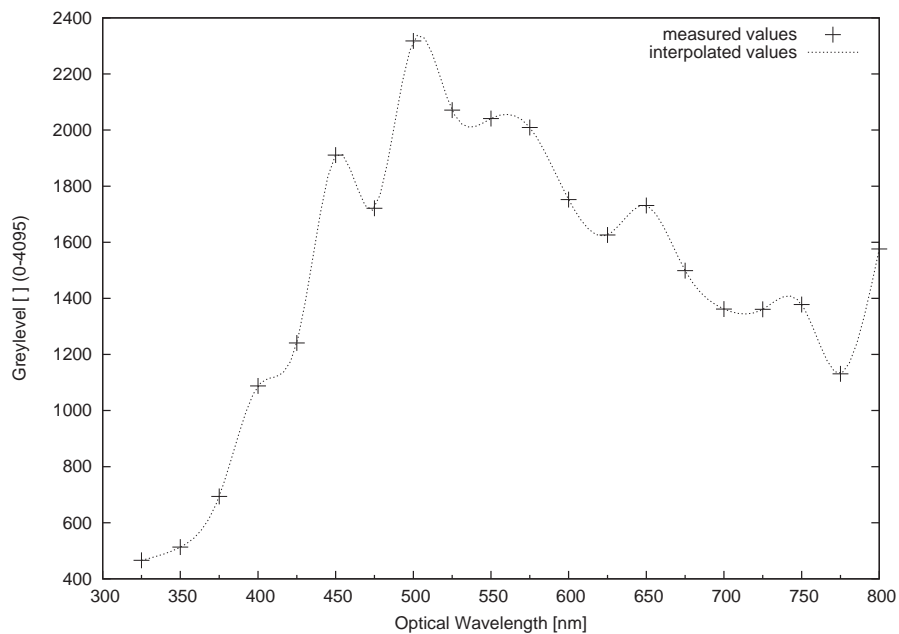


Figure 4.12: Measured spectral response of the photodiodes (range 325-800nm).

4.4 Capacitive Sensing

The capacitive sensing circuits allow for a fully-electronic detection of bioparticles with no need for any external, bulky or expensive equipment. The requirements are the same of DEP actuation, basically a conductive lid, which builds up a microchamber for the samples. The seals at the

borders of the chamber are realized with tape, glue or dry resist [73, 80, 74]. The main circuits for capacitive sensing have already been shown in Fig. 2.7.

4.4.1 Equivalent circuit model for capacitive sensing

Capacitive sensing allows to detect the presence of a particle over an electrode by measuring the variation of the capacitive coupling between the lid and the electrode itself.

The sensed capacitance, in an ideal world, would be composed of two series capacitances: the capacitance of the sample C_L (i.e. capacitance of the buffer, locally perturbed by presence of particles) and the capacitance of the passivation layer of the CMOS process C_P (i.e. silicon nitride Si_3N_4). The ideal situation is depicted in Fig. 4.13(a).

In a real world, as the suspending medium usually has a finite conductivity for physiological reasons, a more realistic model should take into

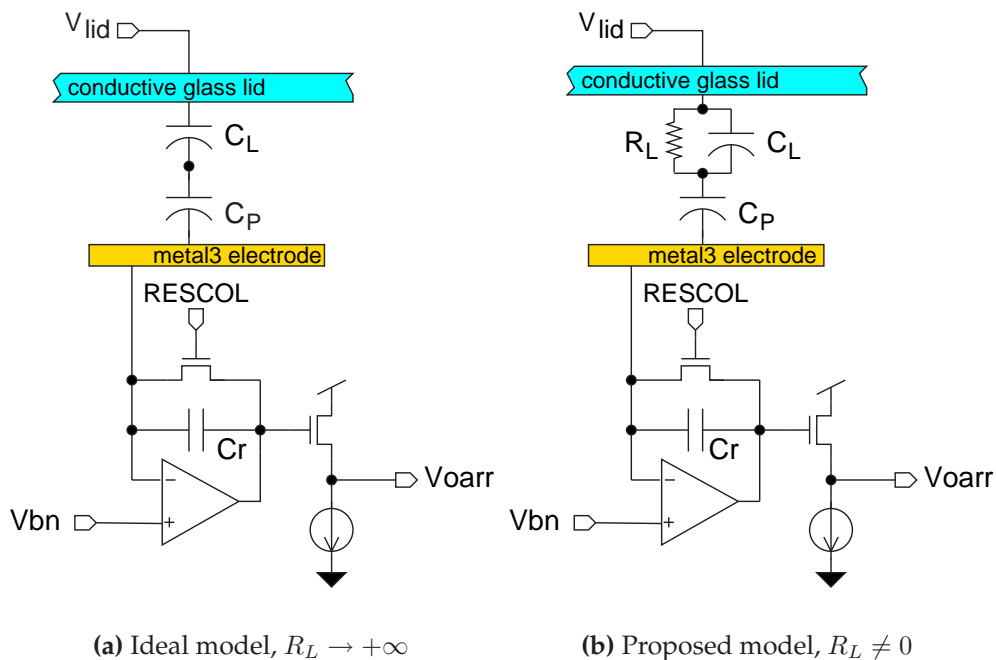


Figure 4.13: Comparison of two models for the sensed impedance.

account this contribution. Moreover, charge accumulation phenomena occur at the interface (e.g. formation of a double-layer of charge due to the presence of an electric field) [76, 77, 78] and should be considered as well, in order to understand capacitive sensing.

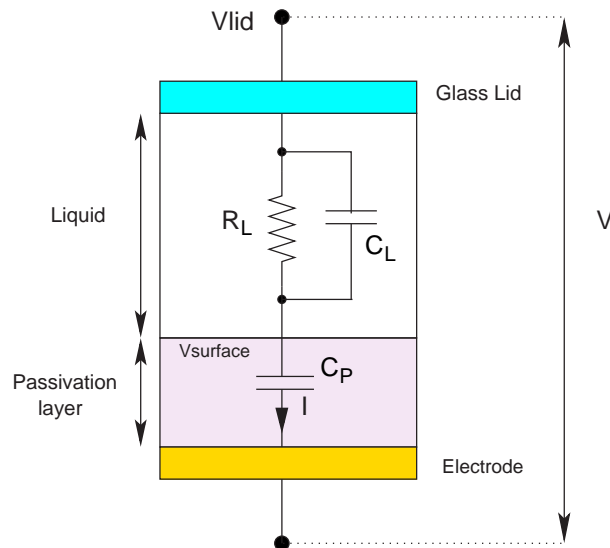


Figure 4.14: Model of the microchamber adopted for capacitive sensing.

The equivalent circuit we propose in order to take into account these relevant phenomena is shown Fig. 4.13(b). C_P represents the capacity of the passivation layer of the CMOS process and takes also into account any charge accumulation occurring at the interface (e.g. double-layer capacitance), C_L is the capacitance of the liquid injected in the microchamber, while R_L is its resistance.

In order to calculate the time constants of the circuits an analysis in Laplace domain is quite useful. Let us apply a sinusoidal voltage V to the circuit, and let us suppose the metal electrode virtually connected to ground. The applied stimulus is $V(t) = V_{lid}(t)$. This hypothesis is quite realistic, because the electrode is connected to the inverting input of the operational amplifier of the circuit, while the non-inverting input is tied to the constant voltage V_{bn} .

If we switch to Laplace domain, we obtain:

$$I(s) = \frac{V_{lid}(s)}{Z(s)} = \frac{sC_P(1 + sR_L C_L)}{1 + sR_L(C_P + C_L)} V_{lid}(s)$$

The transfer function is thus:

$$\frac{I(s)}{V_{lid}(s)} = \frac{1}{Z(s)} = \frac{sC_P(1 + sR_L C_L)}{1 + sR_L(C_P + C_L)} \quad (4.1)$$

This function has a pole in:

$$\omega_p = \frac{1}{R_L(C_L + C_P)},$$

a zero in the origin, and a zero in

$$\omega_z = R_L C_L.$$

The time constant of the circuit is thus:

$$\tau_p = R_L(C_P + C_L) \quad (4.2)$$

In the above equation it usually holds true that $C_P \gg C_L$. R_L is the resistance of the liquid between lid and electrode.

R_L is related to the conductivity of the medium σ_L mainly by two geometrical parameters: W , the width of the pixel, and h , the height of the microchamber, if we consider a parallelepiped model of the resistor:

$$R_L = \frac{1}{\sigma_L} \frac{h}{W^2}$$

Actually, the real course of the current in the liquid doesn't follow the parallelepiped model, but has a qualitative trend like the one shown in Fig. 4.15. Despite its simplicity, this model will provide good match with measured data.

Let us now suppose that a negative voltage step of amplitude V_{lid} is applied to the lid at time $t = t_0$. As shown in Fig. 4.16, we suppose that

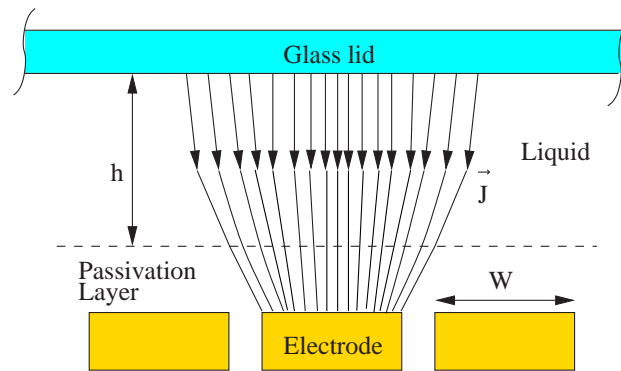


Figure 4.15: Qualitative trend for electric field between the lid and an energized electrode.

we have already deactivated RESET and sampled the reset value (which is affected by charge injection from the reset switch)

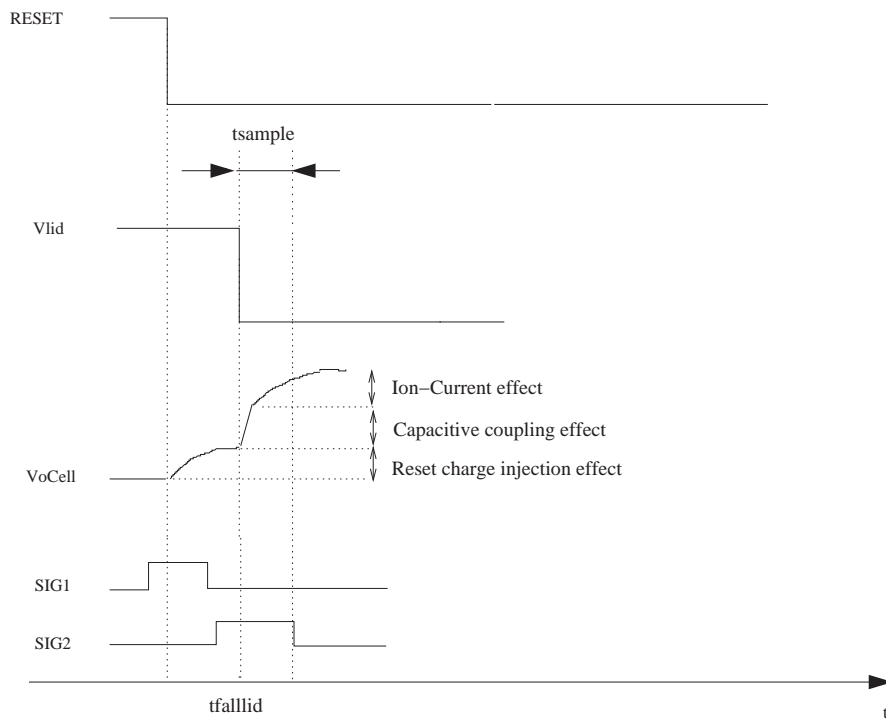


Figure 4.16: Control waveforms used to evaluate ionic current.

When $t = t_0^+$, we have, for the voltage at the interface V_s the following expression:

$$V_s = V_{lid} \frac{C_L}{C_L + C_P}$$

while the voltage on C_L is given by:

$$V_{C_L}(t) = V_{lid} \frac{C_L}{C_L + C_P} e^{-\frac{t}{\tau_P}} \quad \tau_P = R_L (C_L + C_P)$$

If we compute the derivative of that signal we obtain:

$$\frac{dV_{C_L}}{dt} = -\frac{V_{lid} C_P}{R_L (C_L + C_P)^2}$$

The current flowing through the microchamber at $t = t_0$ can now be evaluated:

$$I_{0+} = I_R + I_{C_L} = \frac{V_{lid} C_P}{R_L C_L + C_P} + C_L \frac{dV_{C_L}}{dt} = \frac{V_{lid}}{R_L} \left(\frac{C_P}{C_L + C_P} \right)^2$$

Once the voltage step has been applied to the lid, the output of the charge amplifier V_{oarr} will be sampled after a time interval t_{sample} .

At the end of the transient, when $V_S = V_{lid}$, the injected charge will be:

$$\int_{t_0^-}^{+\infty} I(t) dt = C_P V_{lid}$$

The transient can be divided in two intervals:

- $[t_0^-, t_0^+]$ where the negative edge on V_{lid} injects charge,
- $[t_0^+, +\infty]$ which takes into account the charge due to the ionic current.

The above quantities can be calculated:

$$Q(t = t_0^+) = \int_{t_0^-}^{t_0^+} I(t) dt = V_{lid} \frac{C_L C_P}{C_L + C_P}$$

$$Q(t = t_{sample}) = \int_{t_0^+}^{t_{sample}} I_0 e^{-\frac{t}{\tau_P}} dt$$

By using Eq. 4.4.1 and calculating the above integral, we finally get to

this expression:

$$Q_{t_{sample}} = V_{lid} \frac{C_P^2}{C_L + C_P} \left(1 - e^{-\frac{t_{sample}}{\tau_P}} \right) \quad (4.3)$$

The two expressions can now be summed together in order to calculate the total charge integrated during the transient as a function of sampling time t_{sample} of V_{oarr} .

$$Q_{chint} = Q(t_0^+) + Q(t_{sample}) = V_{lid} \frac{C_P}{C_L + C_P} \left[C_L + C_P \left(1 - e^{-\frac{t_{sample}}{\tau_P}} \right) \right] \quad (4.4)$$

We can define an equivalent sensed capacitance as a function of t_{sample} :

$$C_{ieq}(t_{sample}) = C_{sensed} = \frac{C_P}{C_L + C_P} \left[C_L + C_P \left(1 - e^{-\frac{t_{sample}}{\tau_P}} \right) \right] \quad (4.5)$$

Fig.4.17 shows a qualitative representation of C_{ieq} .

One can observe that, if we sample immediately after the voltage step

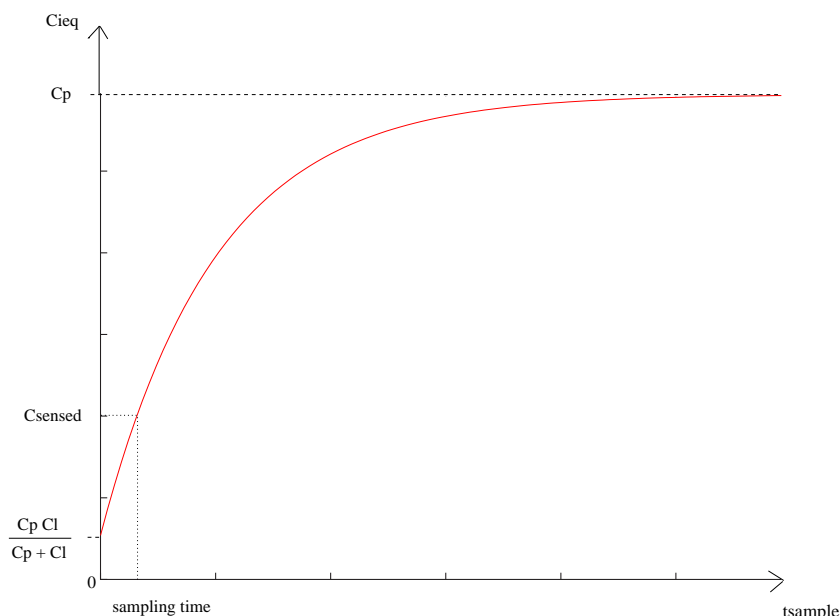


Figure 4.17: Representation of C_{ieq} as a function of sampling time, according to the proposed equivalent circuit model.

on the lid ($t_{sample} = 0$), we obtain:

$$C_{ieq}(t_0^+) = \frac{C_P C_L}{C_L + C_P}$$

As already mentioned before, it is usually true that $C_p \gg C_L$, so that

$$C_{ieq}(t_0^+) \approx C_L$$

On the contrary, if we choose a longer sampling time, what we can sense asymptotically is nothing more than the passivation capacitance C_P :

$$Q_{chint} \xrightarrow[t \rightarrow +\infty]{} C_P V_{lid}$$

Under this condition, no information can be extracted from the sample.

Finally, the measured capacitance is described by this exponential equation, which is also plotted in Fig. 4.17.

$$C_i(C_P, C_L, R_L, t) = \frac{C_P}{C_L + C_P} \left[C_L + C_P \left(1 - e^{-\frac{t}{\tau_P}} \right) \right] \quad (4.6)$$

4.4.2 Characterization of particles

In order to evaluate the variations in C_L and R_L due to the presence of particles, the sensor output V_{oarr} was sampled in two pixels, after injecting a mixture of $50\mu\text{m}$ polystyrene beads in distilled water. The first pixel had no overlying particles, while the second was covered by one of the beads. Fig. 4.18 plots the sensor outputs versus sampling time and confirms the impedance model introduced in Eq. 4.5.

Values for C_L , R_L and C_P can be extracted, and for a $50\mu\text{m}$ polystyrene bead it yields that:

$$C_L \simeq 2.2 \text{ fF}$$

$$R_L \simeq 240 \text{ M}\Omega$$

$$C_P \simeq 11.7 \text{ fF}$$

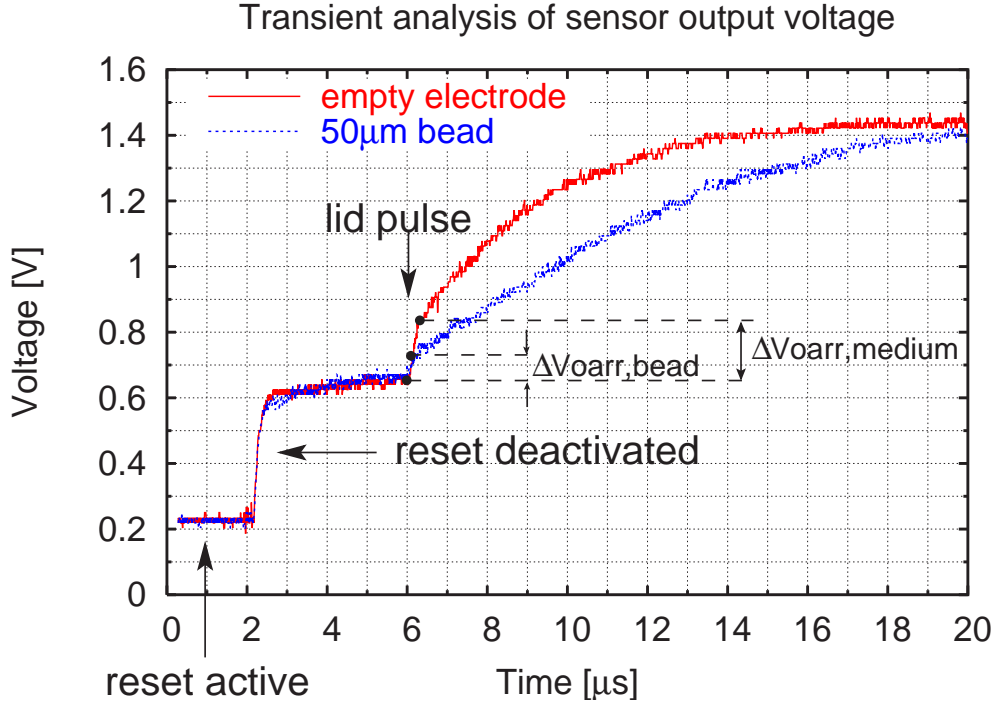


Figure 4.18: Comparison of the sensor output V_{oarr} for an electrode with a $50\mu\text{m}$ polystyrene bead and an electrode without particles. $\Delta V_{lid} = 300\text{mV}$

$$C_{L,bead} = 0.3 C_L$$

$$R_{L,bead} = 2.1 R_L$$

It can be observed that, if $t_0 < t_{sample} < +\infty$, the output voltage V_{oarr} also depends on R_L , which increases the signal range and thus the sensitivity. For example, in Fig. 4.18, when $t \simeq 10\mu\text{s}$, the difference in voltage between the pixels is maximum, so as to improve detection of presence of particles. This happens when R_L increases and C_L decreases or vice-versa.

Analog experiments were performed with *Yarrowia lipolytica* yeasts trapped in clusters by exploiting pDEP. Capacitive sensors detected them successfully, as shown in Fig. 4.19. Capacitance and resistance deviations were extracted from experimental data. Fluctuations in values among experiments are due to differences in double layer formation and to the chamber height imposed by the thickness of the tape gasket. Pixels with yeasts read a capacitance equal to about 90% of the nominal value, while

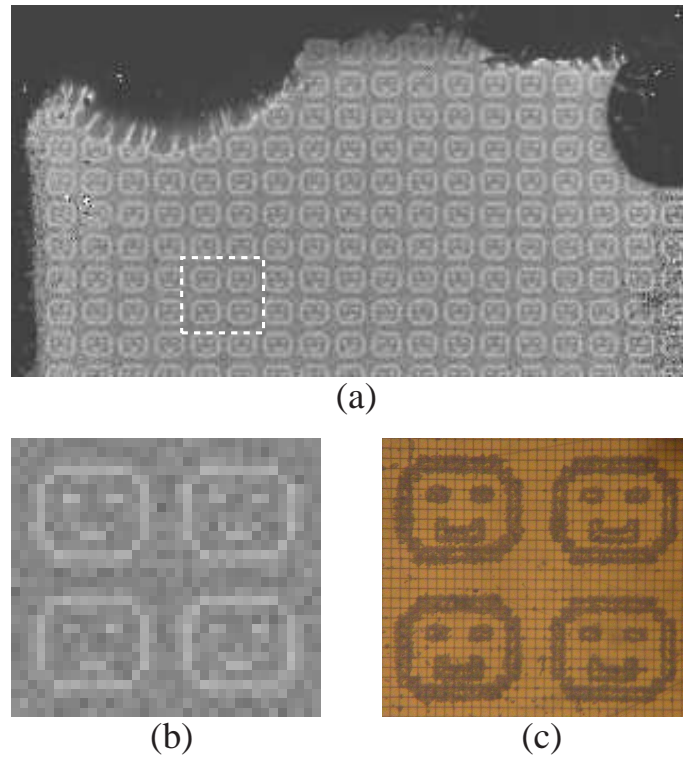


Figure 4.19: Successful detection of *Yarrowia lipolytica* yeasts. In (a) the whole image is shown, while (b) and (c) show respectively details of the capacitive and microscope images.

resistance is about 3 times its nominal value. According to this, in this case the successful detection of yeasts mainly relies upon a variation in resistance rather than in capacitance.

4.4.3 Effect of the sampling time

Upon application of a negative voltage step on the lid, Eq. 4.6 states that the effect of R_L consists in an asymptotic discharge of the capacitor C_L , so that the read-out circuit will be able to sense only C_P when $t \rightarrow \infty$. For $t = t_0^+$, the sensed capacitance will be that of the series of C_L and C_P . Fig. 4.21 shows how particles fade in the background by increasing the sampling time. The useful signal may also be increased by the presence of R_L . If both the perturbations on R_L and C_L had been negative or positive, the two curves would cross, and at a given time we wouldn't be able to

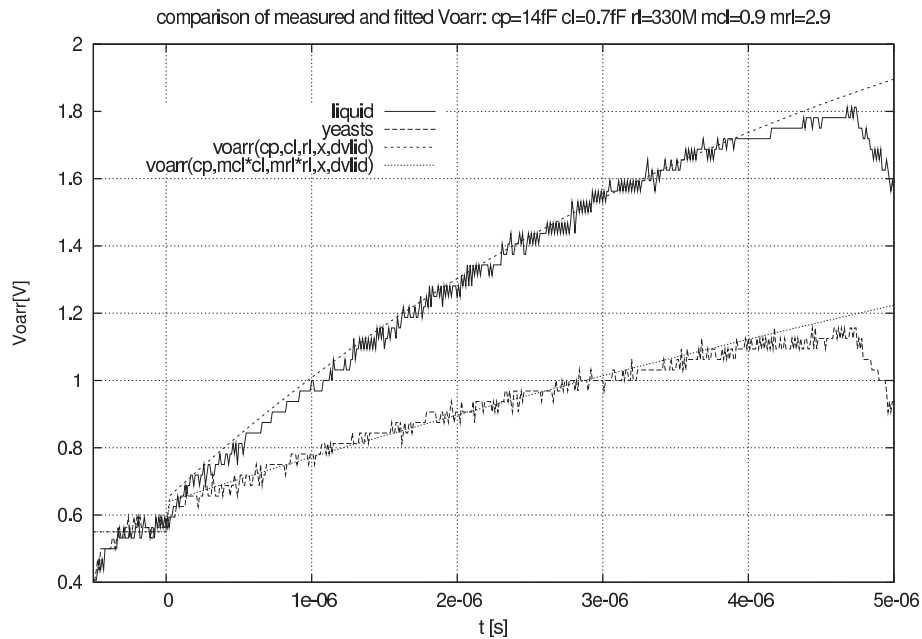


Figure 4.20: Characterization of clusters of yeasts as shown in Fig. 4.19

detect particles at all, as depicted in Fig. 4.22.

4.4.4 Fitting experimental data

The goal of these experiments is to fit the curves obtained with measured data with the estimated values of the parameters C_L , R_L , C_P . The values of C_P are extracted from the measures: in fact, according to Eq. 4.6, it holds that:

$$C_i(C_P, C_L, R_L, t) \xrightarrow[t \rightarrow +\infty]{} C_P$$

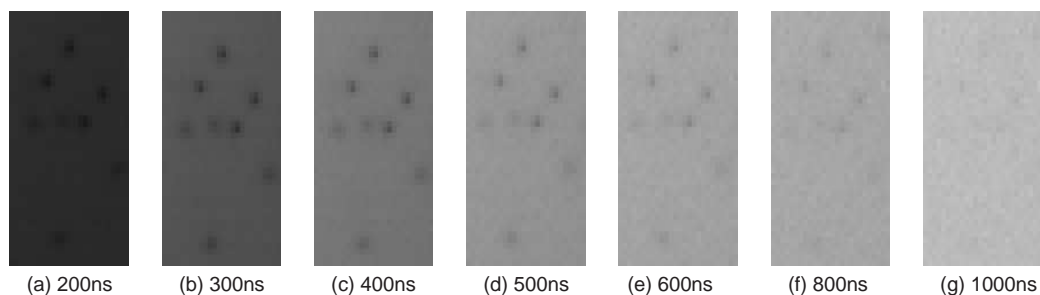


Figure 4.21: Dependence of the equivalent sensed capacitance on the sampling time. $50\mu\text{m}$ beads fade in the background as t_{sample} increases.

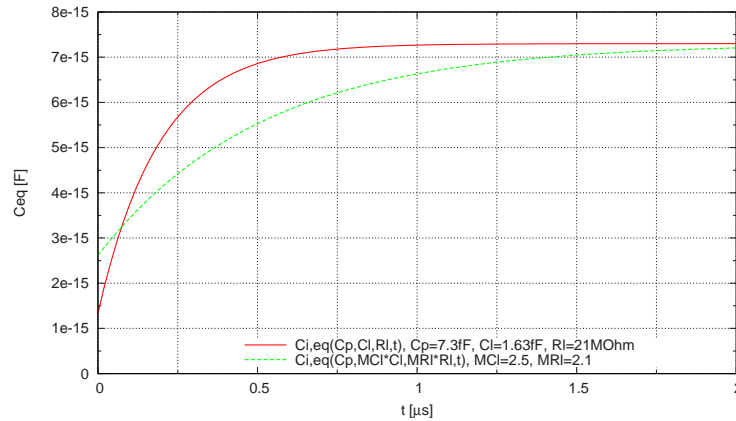


Figure 4.22: Trend of sensed capacitance with coherent deviations in C_L and R_L .

The values of C_L are extracted from the measures too. According to the model in (4.6):

$$C_i(C_P, C_L, R_L, 0) = \frac{C_P C_L}{C_P + C_L} \implies C_L = \frac{C_i(t=0)}{1 - \frac{C_i(t=0)}{C_P}}$$

R_L can be calculated as well from experimental data, by matching τ_P of the curves.

The values of R_L were determined by measuring σ_L with a laboratory conductimeter and by estimating the values of W and h , so that:

$$R_L = \frac{1}{\sigma_L} \frac{h}{W^2}$$

The values of capacitors have been approximated with a parallel plate model and using the values of dielectric permittivity of the involved materials.

$$C = \varepsilon \frac{S}{d}$$

where S is the area of the the plates and d is the distance between them.

4.4.5 Matching data and models

In Fig. 4.23 a comparison of the measured and estimated data for $C_i(t)$ is shown for a *Bricolage* chip. Data were obtained with $\sigma_L = 18.9 \mu S/cm$.

Thicker curves plot the values according to the theoretical model, where the parameters were estimated as discussed in previous section 4.4.4. It is possible to observe that deviations from the estimated curve are relatively small, while the transients are quite similar to the expected trends. This kind of measurements was then repeated for different values of σ_L , and even in these cases the fitting parameters matched the estimated ones with an error of about 15%.

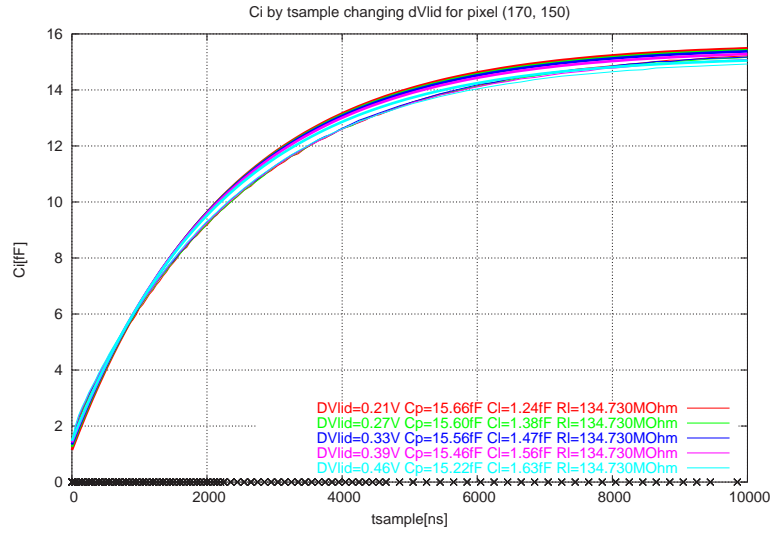


Figure 4.23: Trends of $C_i(t_{sample})$ for a *Bric* chip, $\sigma_L = 18.9 \mu S/cm$. The thickened curves represent the theoretical model with the estimated values of C_P, C_L .

In MEDT devices, by fitting data obtained at different buffer conductivities, it can be observed that a value of $C_P \simeq 78 fF$ is constant among all the considered cases. This value corresponds to an estimated thickness of the passivation layer of $300nm$, which is coherent with reports on fabrication of the devices. The trend of $C_i(t_{sample})$ can be observed in Fig. 4.24.

A good match was also found at low conductivities ($\sigma_L < 100 \mu S/cm$) between the measured σ_L and the values extracted from data for both *Bric* and MEDT devices.

A more relevant amount of data is included in an internal report from our group [79].

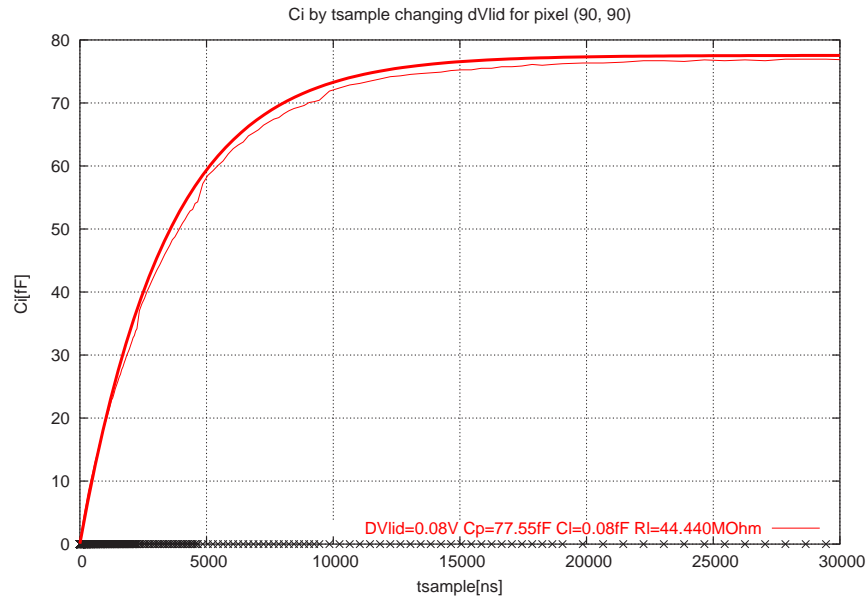


Figure 4.24: Trends of $C_i(t_{sample})$ for a MEDT device, $\sigma_L = 57.3 \mu S/cm$. The thickened curves represent the theoretical model with estimated values of C_P and C_L .

4.5 Quantitation of particles

An interesting important feature for integrated lab-on-a-chip devices is the capability of detecting and quantitating cells present in the sample. For example, it would be an application of interest for point-of-care diagnostics to count red or other blood cells present in a small drop of sample. DEP actuation allows us to trap and concentrate cells at specific and known positions along the sensor array. Given that, sensor response is measured and information concerning the samples are gathered.

A preliminary set of experiments was performed, with red blood cells. Cells were first trapped into a regular pattern, and then several steps of concentration (i.e. merging of two cages) were made. The steps of the protocol are shown in Fig. 4.25. At each step the sensor response in the concentrating cage and in the surrounding ones was measured. As photodetectors have a limited area, when concentration rises too much it is necessary to evaluate the neighbouring sensing sites (Fig. 4.26).

Basically, concentration is evaluated as a weighted average of the val-

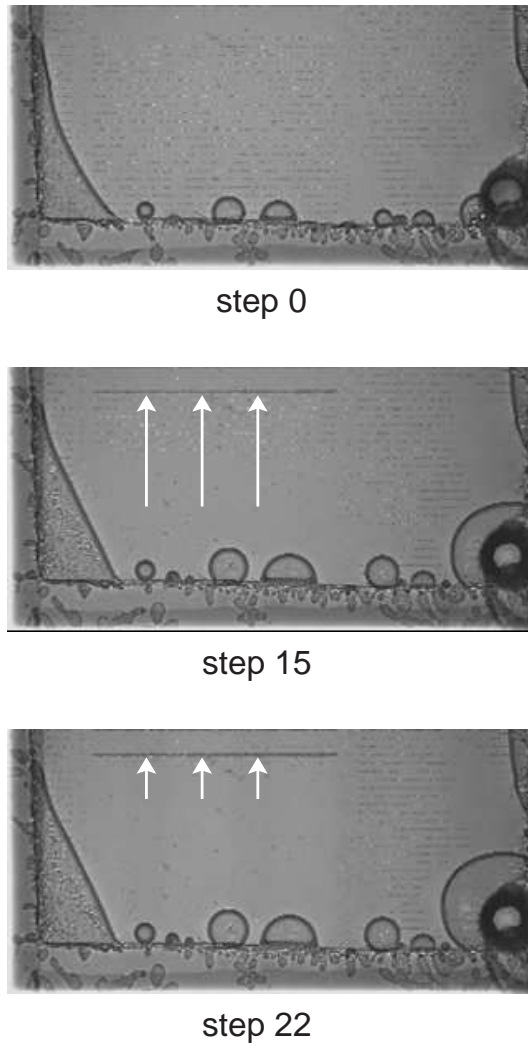


Figure 4.25: Some steps of the concentration protocol, applied to red blood cells.

ues of the concentrating cage and the neighbouring ones. If we define the measured signal as a function of coordinates $p(x, y)$, we may also define the local deviation from the average value μ as: $d(x, y) = |p(x, y) - \mu|$. For a row-organized pattern, we may evaluate the concentration $c(x, y)$ as:

$$c(x, y) = \frac{1}{2N + 1} \sum_{i=-N}^N w_i \cdot d(x, y + i)$$

where the terms w_i are the different weights for the surrounding pixels, $w_0 = 1$, and $w_i < w_0$ (when $i > 0$). Finally, this concentration can be

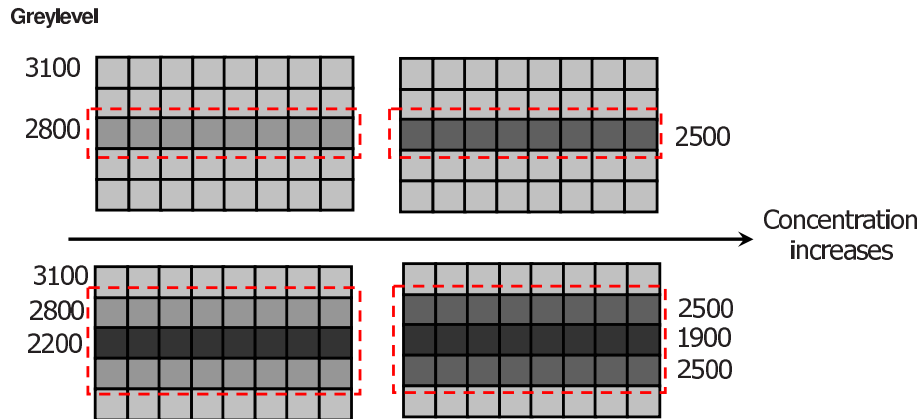


Figure 4.26: Qualitative trend of distribution of cells during the concentration protocol.

averaged over the line above which it was calculated:

$$C(y) = \frac{1}{x_2 - x_1 + 1} \cdot \sum_{x=x_1}^{x_2} c(x, y)$$

where x_1 and x_2 are the boundary x coordinates of the averaging operation.

The obtained results with $N = 1$ are plotted in Fig. 4.27 It can be observed that by choosing an appropriate weight the trend can be kept linear ($w_1 = w_{-1} = 0.25-0.50$ in this plot). In this case only adjacent pixels are considered, so that as soon as these get filled (and cells invade once again adjacent electrodes) the curve shows a saturation effect. By increasing N this effect can be limited.

4.6 Noise analysis

Besides circuital and analytical considerations on noise of the presented circuits in view of their SNR limit that will be presented in section 4.7, measurements were performed on the chips in order to evaluate the effective noise and to support the analytical models.

The output stage of the chip, as discussed in section 2.5.3, mainly con-

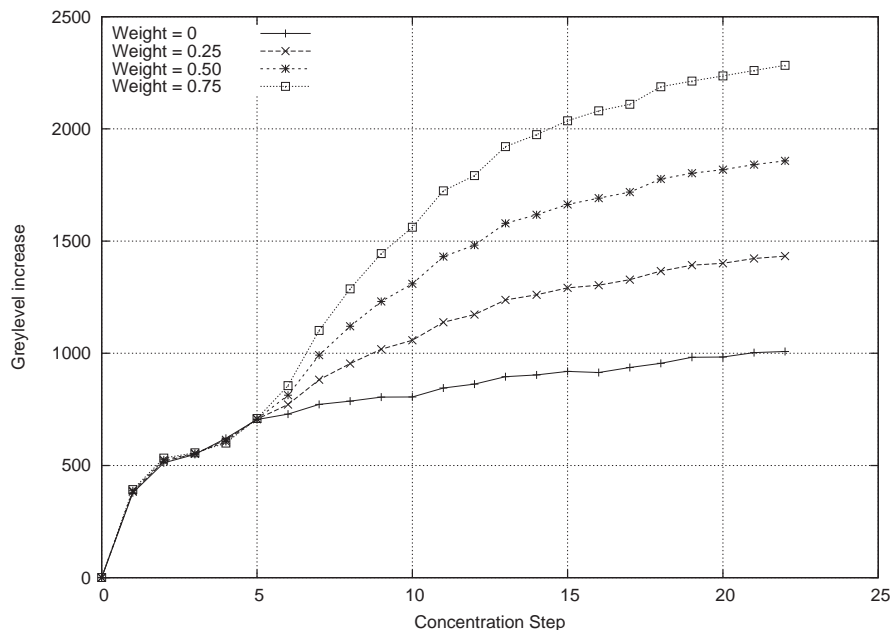


Figure 4.27: Deviations from the background value as a function of concentration step. Red blood cells are organized in a row pattern ($N = 1$, $w_1 = w_{-1}$). The same data set is analyzed with different weights for neighbouring pixels.

sists of a switched capacitors differential amplifier. Noise measurements were performed on a statistical base. Basically, each pixel of the array was repeatedly read up to 10,000 times. The collected data were analyzed at pixel level, and at array level. Data usually are indicated in the number of greylevels of the external ADC (1 LSB \simeq 1.61 mV).

The main analyses basically consisted on extracting the average values and the standard deviations of the sensor array output voltage $V_{outdiff}$, classically defined as:

$$\mu = \frac{1}{N} \cdot \sum_{i=0}^{N-1} x_i$$

$$\sigma = \sqrt{\frac{\sum_{i=0}^{N-1} (x_i - \mu)^2}{N}}$$

The measured values were then referred to equivalent input capacitances or particle transparencies.

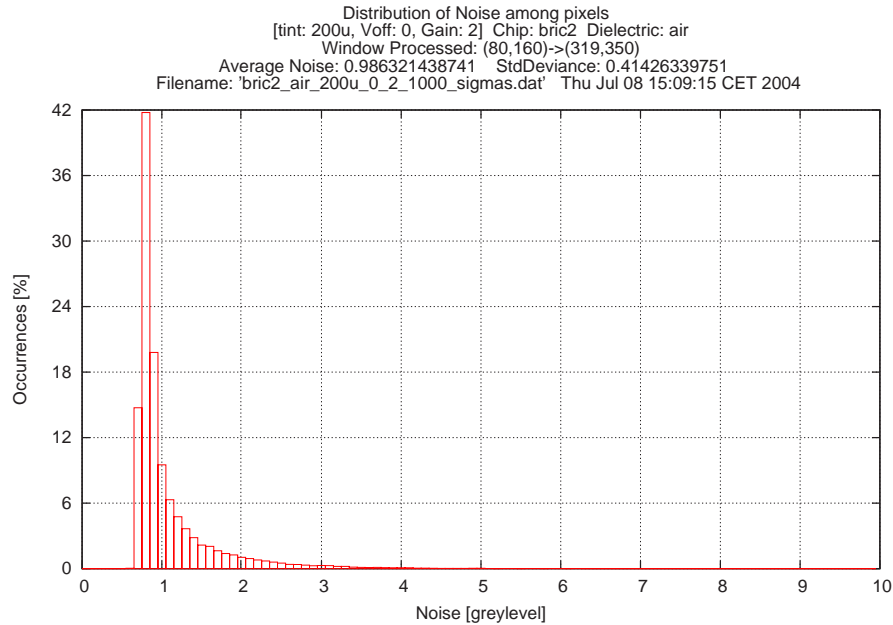


Figure 4.28: Distribution of noise among pixels of the optical array.

4.6.1 Noise on optical sensors

Noise on the optical array was evaluated by setting $V_{off} = 0$, gain of the readout stage to 2, and $t_{int} = 200\mu s$. The obtained results are plotted in Fig. 4.28.

Each pixel was characterized by a specific noise value, that could be repeatedly obtained in different experiments. Table 4.1 shows an analysis of the distribution of noise (σ) among all the pixels of the array. The 99% of the pixels is characterized by a $\sigma < 2$.

4.6.2 Noise on capacitive sensors

Noise of the capacitive array was measured in different operating conditions. A characterization of the intrinsic noise of the device, showed an average value of noise among pixels of $\sigma \simeq 1$ LSB, while the standard deviation on the distribution of noise among pixels was less than 1 bit of the external ADC, as depicted in Fig. 4.29.

Anyway, the most representative values refer to normal operating conditions, when a liquid sample is injected in the microchamber, and V_{lid}

Table 4.1: Analysis of the distribution of noise among optical pixels

$\sigma <$	Prob%
0.5	00.00 %
1.0	85.21 %
1.5	97.09 %
2.0	99.15 %
3.0	99.89 %
4.0	99.99 %
5.0	100 %

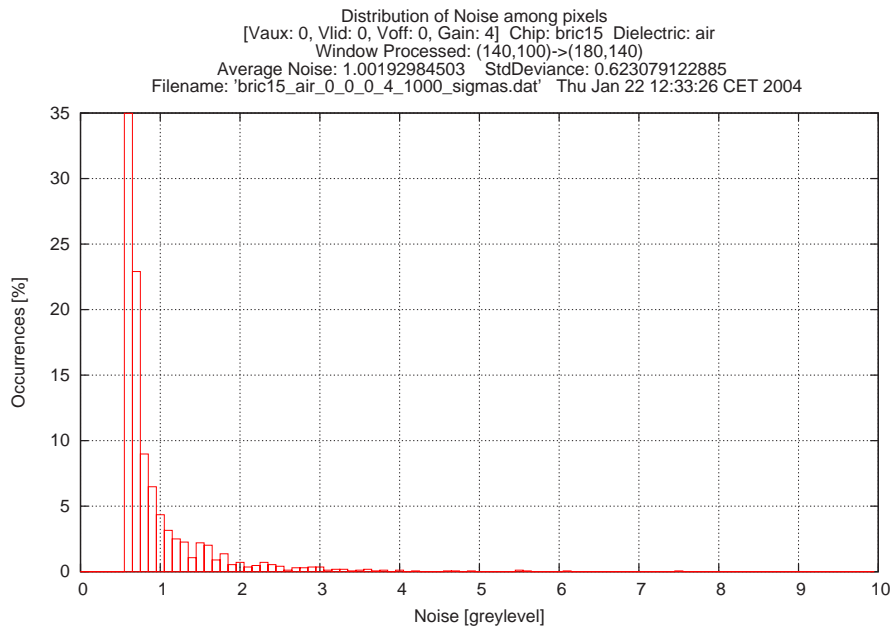


Figure 4.29: Distribution of noise among pixels of the capacitive array. $V_{lid} = 0$, $V_{aux} = 0$, empty microchamber.

and V_{aux} are externally supplied. In these conditions noise increases. Part of the increment is due to noise on the above external voltages which is directly fed into the sensing circuit. Fig. 4.30 reports the results in distribution of noise among pixels in typical operating conditions. The average noise on pixels is $\sigma \simeq 3$ LSB, with a standard deviation $\sigma_\sigma \simeq 1$ LSB.

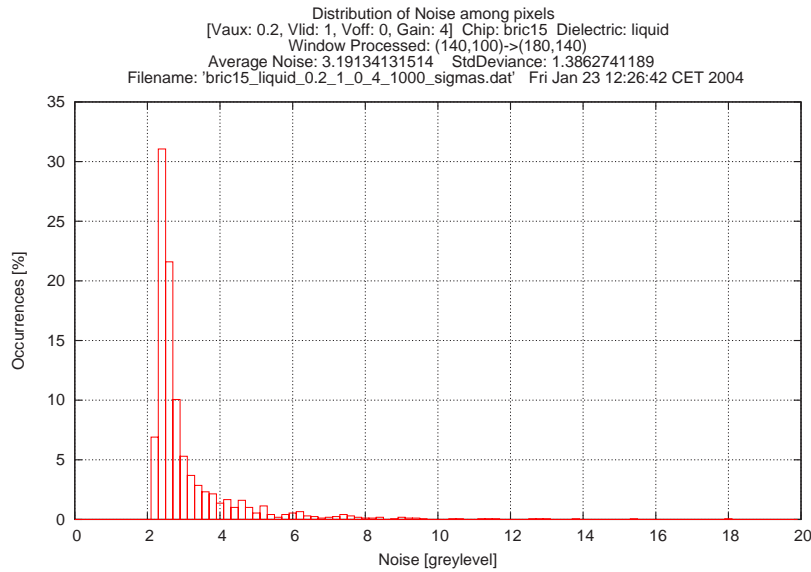


Figure 4.30: NoiseMatrixHistoSigma con dielettrico H_2O distillata e $V_{aux}=0.2$ V e $V_{lid}=1.0$ V

4.6.3 Fixed pattern noise

According to measurements on the device, fixed pattern noise is a relevant factor which limits the sensitivity of detection, and has a much greater influence than temporal noise. By using a CDS technique in the readout stage we have already cancelled the effects of constant fixed pattern noise sources. The gain component of fixed pattern noise has still to be compensated. A simple technique of compensation was implemented, based on computing gain corrections from a reference image.

Without compensation, typical values describing variability among pixels are:

$$\sigma_{FPN,opt} \simeq 98.2 \text{ LSB}$$

$$\sigma_{FPN,cap} \simeq 49.2 \text{ LSB}$$

The total noise on the image can be obtained by composing the two noise contributions:

$$\sigma = \sqrt{\sigma_n^2 + \sigma_{FPN}^2}$$

We can assume $\sigma_n^* = 3$ as a representative value for the temporal noise of

each pixel of the array, since in every tested device the 99% of pixels has $\sigma_n \leq 3$.

As $\{\sigma_{FPN,opt}, \sigma_{FPN,cap}\} \gg \sigma_n^*$, the total noise in optical and capacitive imaging can be expressed as:

$$\sigma_{CAP} = \sqrt{\sigma_n^{*2} + \sigma_{FPN,cap}^2} \approx \sigma_{FPN,cap}$$

$$\sigma_{OPT} = \sqrt{\sigma_n^{*2} + \sigma_{FPN,opt}^2} \approx \sigma_{FPN,opt}$$

These values correspond to a minimum detectable capacitance variation $\Delta C_i = 1.14 fF$, and to a maximum detectable transparency of particles $\alpha = 0.84$, as it will be explained in next section. α is defined as the ratio between transmitted and impinging optical power. The above expressions let clearly understand how any reduction of fixed pattern noise will greatly enhance detection sensitivity of the sensor arrays.

After compensation of FPN, the following results were obtained:

$$\sigma_{FPN,opt}^{(c)} = 6.76 \text{ LSB}$$

$$\sigma_{FPN,cap}^{(c)} = 19.9 \text{ LSB}$$

After applying the FPN compensation algorithm, the corresponding sensing boundaries move to $\Delta C_i = 0.28 fF$ and $\alpha = 0.91$, so that capacitance variations 4 times smaller and particles 10% more transparent can be detected.

4.7 Analysis of sensing limits

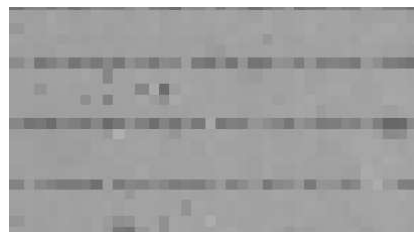
As the size of the sensed objects scales down to cell level, the perturbations in the measured physical quantities become lower, and the impact of circuit noise becomes a relevant limiting factor. For this purpose, different techniques and approaches can be adopted in order to improve the SNR. For example, differential sensing of output voltage variation after the reset of the cell, usually referred to as correlated double sampling (CDS)

[84], compensates for KTC and charge injection noise of reset transistor as well as for the variations of parameters within the array, called fixed pattern noise. Additionally, CDS techniques further improve the SNR of the readout process by greatly reducing low bandwidth noise such as the $1/f$ noise [85]. Another approach, used in the circuit shown in Fig. 2.5 and 2.10, is the subtraction of programmable offset charges or voltages. This approach allows to increase input stimuli (e.g. voltage pulse amplitude or integration time) and to keep the signal in the linear range of amplifier stages while, on the other hand, variations among pixels are boosted.

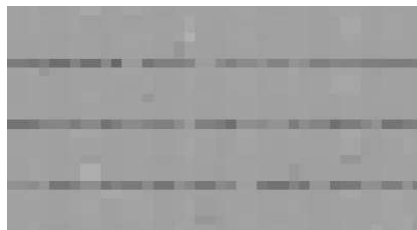
The final part of this section addresses some issues related to the impact of noise and of technological scaling on the detection of micro-particles, as published in [83, 48, 47]. As a case study, the detection limits of optical and impedance sensors of bioparticles, shown in Fig. 2.5 and Fig. 2.7, will



(a) Reference image for compensation. No particles are present in the device.



(b) Cells (RBCs) are injected in the device.



(c) The FPN compensation algorithm is applied.

Figure 4.31: Example of compensation of a portion of an optical image of trapped red blood cells.

be analyzed. In a noisy environment, if we assume gaussian distributions, the error probability P_e in detecting two levels of signal V_2 and V_1 (e.g. corresponding to the presence or absence of a particle above the sensing site) is given by:

$$P_e = \frac{1}{2} \operatorname{erfc} \left(\frac{V_1 - V_2}{2\sigma_n\sqrt{2}} \right) = \frac{1}{2} \operatorname{erfc} \left(\frac{\text{SNR}}{2\sqrt{2}} \right) \quad (4.7)$$

where σ_n is the root mean square value (RMS) of total equivalent noise and SNR the signal-to-noise ratio [86].

In a CMOS photodiode working in storage mode, the number of optically generated electrons is expressed by:

$$N_{opt} = \frac{A_j S P_0 T_i}{q}$$

where A_j is the area of the photojunction, S the sensitivity of the photodiode, P_0 the impinging optical power and T_i the integration time.

In order to detect a particle from the background with a given error probability, it turns out that:

$$\text{SNR} = \frac{N_{opt} (1 - \alpha)}{\sqrt{N_{shot}^2 + N_{NA}^2}} > \xi$$

where where $N_{shot} = \sqrt{N_{opt}}$ is the contribution of the shot noise, while N_{NA} takes into account contributions from other noise sources (e.g. KTC, dark current, read-out circuits, etc.). Both terms are expressed in electrons. We also define α as the optical transmittivity of the particle, defined as the ratio between the optical power transmitted through the particle and the total incident power on the particle, and ξ is the lower bound for SNR. For example, $\xi = 4.6$ for a P_e limited to 1% according to Eq. 4.7. In this discussion we assume $0 \leq \alpha \leq 1$ which corresponds to opaque particles. However similar considerations can be drawn with transparent particles which often concentrate impinging light on sensors (i.e. particles act like lenses) so that the equivalent transmittivity is $\alpha > 1$.

The integrated charge is also limited by an upper bound:

$$q N_{opt} \leq Q_{sat}$$

where Q_{sat} is the maximum optical charge allowed to operate in the photosite. These considerations, if we assume $N_{NA}(1 - \alpha) \gg \xi$, yield to the following expression:

$$q \left[\frac{\xi^2}{2(1 - \alpha)^2} + \frac{\xi N_{NA}}{1 - \alpha} \right] \leq P_0 T_i A_j S \leq Q_{sat} \quad (4.8)$$

which shows the physical limits of optical sensing for microparticles for a given optical transmittivity. An equivalent *optical operating charge* is defined by impinging optical power P_0 , integration time T_i , sensitivity S and area A_j of photojunction.

As indicated in Eq. 4.8, optical detection of particles may be successfully performed as long as the *optical operating charge* stays within the range given by the *floor detection charge* and *saturation charge*, and as long as these two boundaries differ, as illustrated in Fig. 4.32. Equation 4.8 is very useful to evaluate the effects of the scaling trend in CMOS technology. Reductions of S and variations of A_j can be compensated by modulating $P_0 T_i$ (i.e. light source and integration time). However, as described in [87] [88], Q_{sat} scales down linearly with process resolution (with a slope of about 100k electrons per μm), while N_{NA} scales up linearly (about 80k electrons per μm), so that technological scaling has a negative impact on the operating range.

As the presence of particles alters the electric field pattern in vicinity of sensing sites, an integrated charge amplifier may be used to detect input capacitance variations, as shown in Fig. 2.9. In this case similar considerations can be drawn. The following equation describes the above circuit:

$$\Delta V_o = -\frac{C_i - C_{aux}}{C_F} \Delta V_i$$

where ΔV_o is the voltage variation on the output node upon application

of counter-phase input pulses ΔV_i and $-\Delta V_i$ on the circuit inputs V_{in} and V_{aux} , C_i the input capacitance measured between an integrated electrode and a conductive lid, C_F the feedback capacitance, while C_{aux} is an auxiliary capacitor used for subtracting a programmable offset charge. The signal that allows distinguishing a particle from the background can be expressed as:

$$\Delta\Delta V_o = \frac{\Delta C_i \Delta V_i}{C_F}$$

where ΔC_i is the input capacitance variation due to the presence of a particle. This yields to the following expression of the SNR:

$$\text{SNR} = \frac{\Delta C_i \Delta V_i}{C_F \sqrt{\sum_k V_{no_k(rms)}^2}} > \xi$$

where the $V_{no_k(rms)}$ are the output-referred noise powers of different noise sources. This analysis will focus on the intrinsic circuit noise and thus will assume noiseless inputs and power supplies. If we assume a single-pole model, and $C_F \gg (C_i + C_{aux} + C_L)/A_0$, (where A_0 is the DC gain of the amplifier stage), the read-out noise introduced by the operational amplifier may be expressed as follows:

$$V_{no_{rout}(rms)} = \sqrt{\frac{4}{3} \frac{kT}{C_{out}} \frac{C_i + C_{aux} + C_L + C_F}{C_F}} \quad (4.9)$$

where C_L and C_{out} are the capacitances on the input and output nodes of the operational amplifier, as indicated in Fig. 2.7.

In this circuit the limit imposed by circuit saturation is overcome by the subtraction of an offset charge $C_{aux} \Delta V_i$. As a consequence, a higher ΔV_i can increase the $\Delta\Delta V_o$ signal while keeping ΔV_o in the linear range. Anyway, as in an integrated device it is likely to be $\Delta V_i \leq V_{DD}$, the intrinsic boundaries for capacitive sensing of particles are thus given by the following expression:

$$\Delta C_i \geq \frac{\xi}{V_{DD}} C_F \sqrt{\frac{4}{3} \frac{kT}{C_{out}} \frac{C_i + C_{aux} + C_L + C_F}{C_F} + V_{no(rms)}^2} \quad (4.10)$$

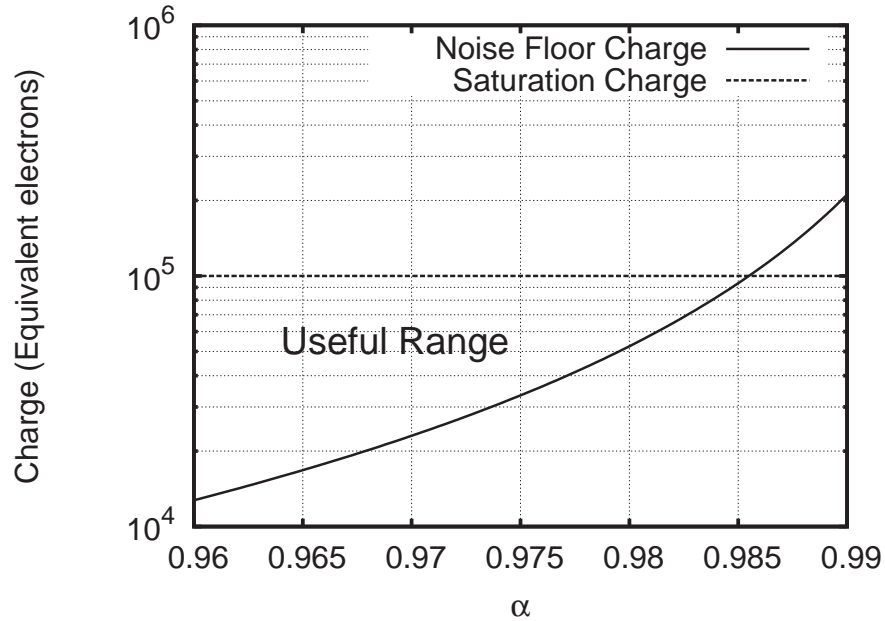


Figure 4.32: The useful range of detection for optical sensing versus particle transmittivity α as described in (4.8) is shown. As illustrated, only particles with $\alpha < 0.986$ (α_{max}) may be detected. The curves were obtained by using the geometries of the photodiode in [51] and the technological parameters of the $0.35\mu\text{m}$ CMOS process used to fabricate the chip.

where we assume that all other noise sources (e.g. contributions from external circuits or following stages) are taken into account by $V_{no(rms)}$. The reduction of the supply voltage has a negative effect on the minimum detectable capacitance, which is also affected by external noise, by design parameters (e.g. C_F) or by the shape and height of the microfluidic chamber containing the samples, which directly determine C_i .

Multiple acquisitions were performed by acquiring 1024 samples for each pixel of the array in order to extract statistical parameters such as the standard deviation, as previously discussed in section 4.6.

According to Eq. 4.7 and to data presented in section 4.6, in order to detect presence or absence of particles with an error probability $P_e = 1\%$, if we assume a worst-case value of $\sigma_n \simeq 4.83$ mV (3 LSB of an ADC) it turns

out that the difference between the voltage levels for decision should be:

$$D = V_2 - V_1 = \Delta\Delta V_o \simeq 6.71 \text{ mV}$$

This quantity can be converted in an equivalent input capacitance variation:

$$\Delta C_i = C_F \frac{\Delta\Delta V_o}{\Delta V_{lid}} \xrightarrow[\Delta V_{lid}=1V, C_F=4.88 \text{ fF}]{\Delta\Delta V_o=D} \Delta C_i = 0.033 \text{ fF}$$

With optical sensors the useful signal for detecting particles of transparency α can be expressed as:

$$\Delta\Delta V_o = (1 - \alpha)\Delta V_{o_{back}} \xrightarrow{\Delta\Delta V_o=D} \alpha = 1 - \frac{D}{\Delta V_{o_{back}}} = 0.98$$

where $\Delta V_{o_{back}}$ is the signal amplitude of the background. The maximum signal range is obtained on the boundary of saturation of the circuits ($\Delta V_{o_{best}} \simeq 0.3V$ in our case).

By referring the data to an equivalent input noise, this process showed that optical sensors, with a 99% degree of confidence, can detect particles with transmittivity $\alpha \leq 98\%$, which is close to the estimated value illustrated in Fig. 4.32. Moreover, experimental results showed, with the same degree of confidence, a minimum detectable capacitance variation given by $\Delta C_{i,min} \simeq 30aF$.

A comparison of the two implemented sensing schemes showed that each one can be best exploited for specific types of particles. For example, while polystyrene micro-beads yield good detection results with both kinds of sensors, the optical sensing scheme showed to be more effective with blood cells (e.g. K562 or red blood cells), while *Yarrowia lipolytica* yeasts, generally containing storage lipides, are more accurately detected with capacitive sensors.

Conclusions

This project demonstrated that microelectronics can be leveraged to achieve highly integrated systems with actuation and sensing of individual cells. The approach pursued within the project showed to have a great potential for cell analysis, for research, for diagnostic and therapeutic applications.

In the research field, with the technology of the presented *lab-on-a-chip* device, biologists may be able to study unprecedented applications in cell biology, for example cell-cell interactions with a precise control on timings, use of the chip for isolation of fluorescently labelled cells from a small cell-load, or programmable complex interactions which might involve, for instance, beads, liposomes, cells.

In the diagnostic field, the system might be used to isolate rare-cells from pre-processed samples, in particular it might afford the possibility to isolate 10-100 cells (too many for manual operation) from a population of 10,000-100,000 (too small for Fluorescent Activated Cell Sorters). Besides, due to the integration of sensors, MeDICS technology could implement a low-cost device for *point-of-care* blood cells analysis.

The development of cell-based CMOS microsystems demonstrates the benefits and possibilities of CMOS-based approaches for handling, stimulating, and detecting living cells. All approaches exploit the large-scale integration offered by CMOS processing and by specifically adapted CMOS circuitry, as actual technologies allow to design complex circuits the size of a cell.

From a scientific point of view, the presented project has produced until now more than 20 scientific publications, in international conferences

Conclusions

and journals. In 2004 the IEEE Solid-State Circuits Society awarded our research group with the Jan Van Vessel Award for presentation of the technical paper [57] concerning the lab-on-a-chip device presented in this thesis.

The experimental validation of the presented device within this project has offered a substantial proof of the viability of this approach. Some of the main future applications of single cell manipulation that can be foreseen are:

Isolation of fetal cells from maternal blood. These rare cells can today be enriched and labelled but a reliable technology for the final isolation of the few cells existing in the original blood sample is required to replace more invasive techniques (e.g. amniocentesis).

Application to cancer therapy. Isolating the natural killer cells which are able to combat tumors, could open up the possibility of culturing them for reinfusion into the patient.

Point-of-care blood analysis. With the integration of actuation and sensing the chip could be used for cell-counting at the point-of-care.

In conclusion, the *lab-on-a-chip* device and technology for individual cell biology presented in this thesis face the challenge of introducing CMOS devices into the biological world and thus may pave the way for use of CMOS chips that host living cells for drug discovery and life science applications. Microelectronic technology has the chance of being at the core of these exciting developments, as it was at the core of the computer industry revolution.

List of Figures

1.1	Lab-on-a-chip: a parallel with computer systems evolution	4
1.2	The lab-on-a-chip performance cube	7
1.3	Comparison of microelectronics minimum feature sizes and biological characteristic dimensions	9
1.4	Programmable cell-handling device.	13
1.5	Schematic plot of a DNA-microarray chip.	18
1.6	Schematic consideration of two test sites.	18
1.7	Schematic plot of the electrode configuration and of the redox-cycling process.	20
1.8	Schematic representation of a cell-based sensor	21
1.9	Contact model of extracellular recording. The intracellular voltage V_M is represented as voltage V_J in the cleft between cell membrane and substrate.	22
1.10	Devices for extracellular recording. (a) Metal electrode. (b) Open field-effect transistor.	23
1.11	Snail neurons cultured on chip surface.	25
1.12	Sensor principle, based on the modulation of the drain current of a MOS transistor	26
1.13	Metal electrode array with active CMOS circuitry for stimulation and recording. (a) Schematic of the chip architecture. (b) Photograph of an active pixel with a shifted metal electrode. (c) Photograph of the entire chip featuring a 4×4 pixels and peripheral circuitry.	26
1.14	Structure of the designed cellular micro-manipulator	28

List of Figures

2.1	Positive and negative dielectrophoresis.	33
2.2	The moving DEP cages approach for cell manipulation. Electromagnetic simulations show how closed cages can be dragged along the chip surface just by changing polarization of the electrode array.	34
2.3	Sketch of the biochip section	38
2.4	Chip Architecture	42
2.5	Micro-site circuit schematic	44
2.6	Representation of the waveforms used to control actuation and optical sensing	45
2.7	Schematic of the micro-site with embedded capacitive detectors	47
2.8	Operation of the device during actuation and capacitive sensing.	48
2.9	Capacitive sensing scheme and principle.	49
2.10	Readout circuit schematic	50
2.11	Correlated double sampling scheme (CDS). The waveforms are referred to the optical sensing scheme.	51
2.12	Signal boosting technique. Subtraction of an offset charge or voltage allows for a higher signal dynamic range.	52
2.13	Chip in microfluidic packaging: the die is mounted directly on the PCB with chip-on-board technique, while a conductive-glass lid is glued to the chip to define the microchamber.	54
2.14	Chip photograph	55
2.15	Comparison of embedded sensor (top left) and optical microscope (top right) images of $50\mu m$ polystyrene beads. In the bottom image the whole images from optical sensors is shown.	56
2.16	Individual manipulation of a $50\mu m$ polystyrene bead in water, $3.3V_{pp}@800kHz$ phases	57
2.17	Manipulation and detection of $50\mu m$ polystyrene beads: actuation pattern (a), microscope image (b), embedded optical sensors image (c).	57

2.18	Mating (a-d) and separation (d-f) of K562 tumor cells in 280mM mannitol in water, $3.3V_{pp}@500kHz$ phases. For the sake of simplicity cage electrodes are enclosed by dashed lines.	58
2.19	Manipulation of clusters of <i>Saccharomyces cerevisiae</i> : 280mM Mannitol buffer, $3.3V_{pp}@1MHz$ phases.	58
2.20	Sensor images of $50\mu m$ polystyrene beads in a 280mM mannitol solution are compared with optical microscope images.	59
2.21	Sensor and microscope images of $10\mu m$ polystyrene beads, <i>Yarrowia lipolytica</i> yeasts and human erythro-leukemia K562 cells in a 280mM mannitol solution Particles brighter than the background have $\epsilon_{particle} > \epsilon_{medium}$ while darker particles have $\epsilon_{particle} < \epsilon_{medium}$	59
3.1	A block diagram of system architecture.	64
3.2	The lab-on-a-chip	65
3.3	A block diagram of the digital part of the developed control system.	67
3.4	XiRisc processor block diagram	70
3.5	Acquired digital waveforms. Bus activity (OE#, WE#) shows that the processor is continuing program execution while the PWG is driving some control signals (PWG[0..2]).	71
3.6	Software architecture block diagram	73
3.7	The prototype board.	74
3.8	Manipulation of human erythroleukaemia cells (K562) and polystyrene beads by means of DEP. The positions of the trapped particles shown in microscope images (a), (c) and in the image acquired with embedded optical sensors (e) match the applied programming patterns (b), (d) consisting of DEP cages with extensions over 1×1 and 2×2 electrodes of the LOAC.	76
4.1	Microfabricated implementation of the microchamber containing samples on the CMOS device	78

List of Figures

- 4.2 The microchamber containing the samples to be inspected is built with a pierced piece of double-adhesive tape acting as a gasket, and a conductive glass lid. Samples are injected through holes in the glass. The contact on the lid is made by depositing a small amount of conductive grease. 80
- 4.3 Organization and manipulation of different type of human cells. In (a) K562 cells are trapped in single electrode DEP cages, in (b) RBCs are aligned in a row pattern. Images in (c) and (d) show respectively individually trapped 221-G and RAJI cells. In (e) and (f) the patterns used to trap the cells above are indicated.
[cell images courtesy of M.Abonnenc, Silicon Biosystems] 82
- 4.4 Time required for cells to move to an adjacent electrode. Data refer to individual K562 cells and a diluted suspension of RBCs.
[Data courtesy of Silicon Biosystems] 84
- 4.5 Technology for sorting and recovering specific cells. In (a) the double chamber design is shown. In (b) and (c) screenshots of the routing software are shown, respectively definition of the obstacles and definition of the route for particles. 84
- 4.6 Selection and routing of few selected individual cells. Cells are routed to their final destination, composing the smallest Valentine ever. 85
- 4.7 Comparison of optical microscope (on the right side) and embedded optical sensors (on the left) images of $3\mu\text{m}$ red beads suspended in Mannitol 280mM and organized in regular patterns at 500KHz, gain 2. Beads are displaced and detected at each step. 87

4.8	Comparison of optical microscope (right) and optical sensors images (left) of red blood cells in Mannitol 280mM + 200 μ M EDTA at the concentration of 10.106 cells/ml. Frequency 50kHz, gain2, MEDU device. Cells are trapped in regular patterns and manipulated. Photodetectors keep track of the positions of displaced cells.	88
4.9	Comparison of optical microscope (center image in (a) and right image in (b)) and embedded optical sensors images of red blood cells suspended in Mannitol 280mM + 200 μ M EDTA at low concentrations. Frequency 50kHz, gain 2, MEDU device.	89
4.10	Comparison of optical microscope (in (b)) and embedded optical sensors (in (a) and (c)) of K562 cells suspended in Mannitol 280mM + 6,25mM KCl in a MEDU device at a frequency of 50kHz, gain 2.	89
4.11	Schematic representation of the setup of the experiment. . .	90
4.12	Measured spectral response of the photodiodes (range 325-800nm).	90
4.13	Comparison of two models for the sensed impedance.	91
4.14	Model of the microchamber adopted for capacitive sensing.	92
4.15	Qualitative trend for electric field between the lid and an energized electrode.	94
4.16	Control waveforms used to evaluate ionic current.	94
4.17	Representation of C'_{ieq} as a function of sampling time, according to the proposed equivalent circuit model.	96
4.18	Comparison of the sensor output V_{oarr} for an electrode with a 50 μ m polystyrene bead and an electrode without particles. $\Delta V_{lid} = 300mV$	98
4.19	Successful detection of <i>Yarrowia lipolytica</i> yeasts. In (a) the whole image is shown, while (b) and (c) show respectively details of the capacitive and microscope images.	99
4.20	Characterization of clusters of yeasts as shown in Fig. 4.19	100

List of Figures

4.21	Dependence of the equivalent sensed capacitance on the sampling time. $50\mu\text{m}$ beads fade in the background as t_{sample} increases.	100
4.22	Trend of sensed capacitance with coherent deviations in C_L and R_L	101
4.23	Trends of $C_i(t_{\text{sample}})$ for a <i>Bric</i> chip, $\sigma_L = 18.9\mu\text{S}/\text{cm}$. The thickened curves represent the theoretical model with the estimated values of C_P, C_L	102
4.24	Trends of $C_i(t_{\text{sample}})$ for a MEDT device, $\sigma_L = 57.3\mu\text{S}/\text{cm}$. The thickened curves represent the theoretical model with estimated values of C_P and C_L	103
4.25	Some steps of the concentration protocol, applied to red blood cells.	104
4.26	Qualitative trend of distribution of cells during the concentration protocol.	105
4.27	Deviations from the background value as a function of concentration step. Red blood cells are organized in a row pattern ($N = 1, w_1 = w_{-1}$). The same data set is analyzed with different weights for neighbouring pixels.	106
4.28	Distribution of noise among pixels of the optical array.	107
4.29	Distribution of noise among pixels of the capacitive array. $V_{lid} = 0, V_{aux} = 0$, empty microchamber.	108
4.30	NoiseMatrixHistoSigma con dielettrico H_2O distillata e $V_{aux} = 0.2\text{ V}$ e $V_{lid} = 1.0\text{ V}$	109
4.31	Example of compensation of a portion of an optical image of trapped red blood cells.	111
4.32	The useful range of detection for optical sensing versus particle transmittivity α as described in (4.8) is shown. As illustrated, only particles with $\alpha < 0.986$ (α_{max}) may be detected. The curves were obtained by using the geometries of the photodiode in [51] and the technological parameters of the $0.35\mu\text{m}$ CMOS process used to fabricate the chip.	115

List of Tables

2.1	Chip specifications	60
3.1	Resource usage summary for the FPGA implementation . .	75
4.1	Analysis of the distribution of noise among optical pixels . .	108

List of Tables

Bibliography

- [1] Silicon Biosystems, University of Bologna, CEA-DSV, CEA-LETI, INSERM, *MeDICS Project: Final Report covering period 1st November 2001 to 31st July 2004*, IST-2001-32437, September 2004
- [2] N. Manaresi, A. Fuchs, D. Freida, L. Altomare, C. L. Villiers, G. Medoro, A. Romani, A. Leonardi, I. Chartier, N. Sarrut, M. Tartagni, P. N. Marche, F. Chatelain, R. Guerrieri, *Biochips and Cell Manipulation: the MeDICS Project*, in Proc. of International Meeting on Micro and Nanotechnologies (MINATEC), September 2003, Grenoble (France).
- [3] A. Manz, J. C. Fetting, E. Verpoorte, H. Ludi, H. M. Widmer, D. J. Harrison, *Micromachining of monocrystalline silicon and glass for chemical analysis systems. A look into next century's technology or just a fashionable craze?*, Trends Anal. Chem., Elsevier Science, vol. 10, pp. 144-149, 1991
- [4] S. P. A. Fodor, R. P. Rava, X. C. Huang, A. C. Pease, C. P. Holmes, C. L. Adams, *Multiplexed Biochemical Assays with Biological Chips*, Nature, vol. 364, pp. 555-556, 1993.
- [5] K. Mullis, F. Falcomer, S. Scharf, R. Snikl, G. Horn, H. Erlich, *Cold Spring Harbor Symp. Quant. Biol.*, 1986, vol. 51, p. 260.
- [6] F. Pourahmadi, K. Lloyd, G. A. Kovacs, K. Petersen, W. A. McMillan, M. A. Northrup, *An Integrated and Automated Sample Processing, Reagent Handling and Nucleic Acid Analysis System for Pathogen Detec-*

Bibliography

- tion and Identification*, in Proc. of the 1998 ERDEC Scientific Conference on Chemical and Biological Defense Research, 1998, pp. 253-258.
- [7] K. Krabchi, F. Gros-Louis, J. Yan, M. Bronsard, J. Masse, J. C. Forest, R. Drouin, *Quantification of all fetal nucleated cells in maternal blood between the 18th and 22nd weeks of pregnancy using molecular cytogenetic techniques*, Clin. Genet., vol. 60, no. 2, pp.145-150, August 2001
- [8] M. A. Burns, C. H. Mastrangelo, T. S. Sammarco, F. P. Man, J. R. Webster, B. N. Johnson, B. Foerster, D. Jones, Y. Fields, A. R. Kaiser, D. T. Burke, *Microfabricated structures for integrated DNA analysis*, Proc. Natl. Acad. Sci. USA, 1996, vol. 93, pp. 5556-5561.
- [9] G. Fuhr, R. Hagedorn, T. Muller, W. Benecke, B. Wagner *Microfabricated Electrohydrodynamic (EHD) Pumps for Liquids of Higher Conductivity*, IEEE Journal of Microelectromechanical Systems, 1992, vol. 1, no. 3, pp. 141-146.
- [10] J. R. Melcher, U. S. Firebaugh, *Traveling wave bulk electroconvection induced across temperature gradient*, Physics of Fluids, 1967, vol. 10, pp. 1178-1185.
- [11] M. A. Unger, H. P. Chou, T. Thorsen, A. Scherer, S. R. Quake, *Monolithic Microfabricated Valves and Pumps by Multilayer Soft Lithography*, Science, 2000, vol. 288, pp. 113-116.
- [12] A. Y. Fu, C. S. Pence, A. Scherer, F. H. Arnold, S. R. Quake, *A microfabricated fluorescence-activated cell sorter*, Nature biotechnology, vol. 17, pp. 1109-1111, November 1999.
- [13] H. A. Pohl, *The motion and precipitation of suspensoids in divergent electric fields*, J. Appl. Phys, vol. 22, pp. 869- 871, 1951.
- [14] J. Sueheiro, R. Pethig, *The dielectrophoretic movement and positioning of a biological cell using a three-dimensional grid electrode system*, J. Phys. D: Appl. Phys, vol. 31, pp. 3298-3305, 1998.

- [15] T. Schnelle R. Hagedorn, G. Fuhr, S. Fiedler, T. Muller, *Three-dimensional electric field traps for manipulation of cells - calculation and experimental verification*, *Biochimica et Biophysica Acta*, 1993, vol. 1157, pp.127-140
- [16] T. Muller, G. Gradl, S. Howitz, S. Shirley, Th. Schnelle, G. Fuhr, *A 3-D microelectrode system for handling and caging single cells and particles*, *Biosensors and Bioelectronics*, vol. 14, pp. 247-256, 1999.
- [17] J. Cheng et al., *Isolation of Cultured Cervical Carcinoma Cells Mixed with Peripheral Blood Cells on a Bioelectronic Chip*, *Anal. Chem.*, vol. 70, pp.2321-2326, 1998
- [18] T. B. Jones, *Electromechanics of Particles*, Cambridge University Press, 1998
- [19] G. Fuhr et al., *Levitation, Holding and Rotation of Cells Within Traps Made by High-Frequency Fields*, *Biochimica et Biophysica Acta*, vol. 1108, pp. 215-223, 1992
- [20] X.-B. Wang, Y. Huang, P. R. C. Gascoyne, F. F. Becker, *Dielectrophoretic Manipulation of Particles*, *IEEE Trans. on Industry Applications*, vol. 30, pp. 660-669, 1994
- [21] M. Washizu, *Precise Calculation of Dielectrophoretic Force in Arbitrary Field*, *J. of Electrostatics*, vol. 29, pp. 177-188, 1992
- [22] M. Washizu, T. B. Jones, *Multipolar Dielectrophoretic Force Calculation*, *J. of Electrostatics*, vol. 33, pp. 187-198, 1994
- [23] T. Schnelle, T. Muller, S. Fiedler, G. Fuhr, *The influence of higher moments on particle behaviour in dielectrophoretic field cages*, *J. of Electrostatics*, vol. 46, pp. 13-28, 1999
- [24] G. Medoro, N. Manaresi, M. Tartagni, R. Guerrieri, *CMOS-only sensors and manipulators for microorganisms*, *IEEE International Electron Devices Meeting (IEDM) Technical Digest*, 2000, pp. 415-418

Bibliography

- [25] G. Medoro, N. Manaresi, A. Leonardi, L. Altomare, M. Tartagni, R. Guerrieri, *A Lab-on-a-chip For Cell Detection And Manipulation*, in Proc. of IEEE Sensors Conference, 2002.
- [26] A. Leonardi, G. Medoro, N. Manaresi, M. Taratagni, R. Guerrieri, *Simulation Methodology for Dielectrophoresis in Microelectronic Lab-on-a-chip*, in Proc. of Modeling and Simulation of Microsystems 2002, Computational Publications, 2002, pp. 96-99.
- [27] A. Leonardi, *Modellistica e progettazione di sistemi elettronici per la manipolazione di elementi biologici*, PhD Thesis, University of Bologna (I), 2004
- [28] A. Fuchs, H. Jeanson, P. Claustre, J. A. Gruss, F. Revol-Cavalier, P. Cailat, U. Mastromatteo, M. Scurati, F. Villa, G. Barlocchi, P. Corona, B. Grieco, *A Silicon Lab-on-a-chip for Integrated Sample Preparation by PCR and DNA Analysis by Hybridization*, in Proc. of IEEE-EMBS Special Topic Conference on Microtechnologies in Medicine & Biology, IEEE, 2002, pp. 227-231.
- [29] P. Cailat, M. Belleville, F. Clerc, C. Massit, *Active CMOS biochips: an electro-addressed DNA probe*, IEEE International Solid-State Circuits Conference Digest of Technical Papers, 1998, pp. 272-273.
- [30] P. Swanson, R. Gelbart, E. Atlas, L. Yang, T. Grogan, W. F. Butler, D. E. Ackley, E. Sheldon, *A fully multiplexed CMOS biochip for DNA analysis*, Sensors and Actuators B, 2000, vol. 64, pp.22-30
- [31] F. K. Perkins, S. J. Fertig, K. A. Brown, D. McCarty, L. M. Tender, M. C. Peckerar, *An active microelectronic transducer for enabling label-free miniaturized chemical sensors*, IEEE International Electron Devices Meeting (IEDM) Technical Digest, 2000, pp.407-410.
- [32] R. Thewes, F. Hofmann, A. Frey, B. Holzapfl, M. Schienle, C. Paulus, P. Schindler, G. Eckstein, C. Kassel, M. Stanzel, R. Hintsche, E. Nebling, J. Albers, J. Hassman, J. Schulein, W. Goemann,

- W. Gumbrecht, *Sensor arrays for fully-electronic DNA detection on CMOS*, IEEE ISSCC Dig. Tech. Papers, 2002, pp. 350-351
- [33] P. R. C. Gascoyne, J. V. Vykoukal, J. A. Schwartz, T. J. Anderson, D. M. Vykoukal, K. Wayne Current, C. McConaghy, F. F. Becker, C. Andrews, *Dielectrophoresis-based programmable fluidic processors, Lab on a chip*, 2004, vol. 4, pp. 299-309
- [34] J. R. Keilman, G. A. Julien, K.V.I.S. Kaler, *A SoC Bio-analysis platform for real-time biological cell analysis-on-a-chip* in Proc. of the 3rd IEEE International Workshop on System-on-Chip for Real-Time Applications, 2003, pp. 362-367
- [35] M. Jenkner, M. Tartagni, A. Hierlemann, R. Thewes, *Cell-based CMOS Sensor and Actuator Arrays*, IEEE Journal of Solid-State Circuits, vol. 39, no. 12, December 2004, pp. 2431-2437
- [36] P. Hegde, R. Qi, K. Abernathy, C. Gay, S. Dharap, R. Gaspard, J. E. Hughes, E. Snestrud, N. Lee, J. Quackenbush, *A concise guide to cDNA microarray analysis*, Biotechniques, vol. 29, no. 3, pp. 548-556, 2000.
- [37] M. Xu, J. Li, Z. Lu, C. Feng, Z. Zhang, P. K. Ko, M. Chan, *A high density conduction based micro-DNA-identification array fabricated in a CMOS compatible process*, IEEE ISSCC Dig. Tech. Papers, vol. 46, no. 1, pp. 198-199, February 2003
- [38] F. Hofmann, A. Frey, B. Holzapfl, M. Schienle, C. Paulus, P. Schindler-Bauer, D. Kuhlmeier, J. Krause, R. Hintsche, E. Nebling, J. Albers, W. Gumbrecht, K. Plehnert, G. Eckstein, R. Thewes, *Fully electronic DNA detection on a CMOS chip: device and process issues*, IEEE International Electron Devices Meeting (IEDM) Technical Digest, pp. 488-491, 2002
- [39] R. Hintsche, M. Paeschke, A. Uhlig, R. Seitz, *Microbiosensors using electrodes made in Si-technology*, Frontiers in Biosensorics, F. Schubert,

Bibliography

- F. W. Scheller, J. Fedrowitz, Eds. Basel, Switzerland: Birkhäuser Verlag, 1997, p. 267.
- [40] F. Heer, W. Franks, A. Blau, S. Taschini, C. Ziegler, A. Hierlemann, H. Baltes, *CMOS microelectrode array for the monitoring of electrogenic cells*, *Biosens. Bioelectron.* vol. 20, no. 2, September 2004, pp. 358-366
- [41] B. Eversmann, M. Jenkner, F. Hofmann, C. Paulus, R. Brederlow, B. Holzapfl, P. Fromherz, M. Merz, M. Brenner, M. Schreiter, R. Gabl, K. Plehnert, M. Steinhauser, G. Eckstein, D. Schmitt-Landsiedel, R. Thewes, *A 128×128 CMOS biosensor for extracellular recording of neural activity*, *IEEE Journal of Solid-State Circuits*, vol. 38, no. 12, December 2003, pp. 2306-2317
- [42] M. Schienle, C. Paulus, A. Frey, F. Hofmann, B. Holzapfl, P. Schindler-Bauer, R. Thewes, *A fully electronic DNA sensor with 128 positions and in-pixel A/D conversion*, *IEEE Journal of Solid-State Circuits*, vol. 39, no. 12, December 2004, pp. 2438-2445
- [43] A. L. Hodgkin, A. F. Huxley, *A quantitative description of membrane current and its application to conduction and excitation in nerve*, *J. Physiol.*, vol. 117, pp. 500-544, 1952
- [44] L. L. Sohn et al., *Capacitance cytometry: measuring biological cells one by one*, *Proc. Nat. Acad. Sci. USA*, vol. 97, pp. 10867-10690, 2000
- [45] S. Gawad, L. Schild, P. Renaud, *Micromachined Impedance Spectroscopy Flow Cytometer for Cell Analysis and Particle Sizing*, *Lab on a Chip*, vol. 1, pp. 76-82, 2001
- [46] C. K. Fuller, *Microfabricated multi-frequency particle impedance characterization system*, *Micro Total Analysis Systems*, pp. 265-268, 2000
- [47] M. Abonnenc, L. Altomare, M. Baruffa, V. Ferrarini, R. Guerrieri, B. Iafelice, A. Leonardi, N. Maresi, G. Medoro, M. Tartagni, P. Vulto, *Teaching cells to dance: the impact of transistor miniaturization*

- on the manipulation of populations of living cells*, Solid-State Electronics, In press, available online 9 February 2005
- [48] M. Abonnenc, L. Altomare, M. Baruffa, V. Ferrarini, R. Guerrieri, B. Iafelice, A. Leonardi, N. Manaresi, G. Medoro, M. Tartagni, P. Vulto, *Teaching cells to dance: the impact of transistor miniaturization on the manipulation of populations of living cells*, in Proc. of the 3rd Workshop on Ultimate Integration of Silicon, March 2004.
- [49] A. Romani, N. Manaresi, L. Marzocchi, G. Medoro, A. Leonardi, L. Altomare, M. Tartagni, R. Guerrieri, *Capacitive Sensor Array for Localization of Bioparticles in CMOS Lab-on-a-Chip*, IEEE ISSCC Dig. Tech. Papers, Feb 2004, vol. 47 pp. 224-225.
- [50] A. Romani, F. Campi, S. Ronconi, G. Medoro, M. Tartagni, N. Manaresi, *A System-on-a-Programmable-Chip for Real-Time Control of Massively Parallel arrays of Biosensors and Actuators*, in Proc. of the 3rd IEEE International Workshop on System-on-Chip for Real-Time Applications (IWSOC), June, 2003, pp. 236-241.
- [51] N. Manaresi, A. Romani, G. Medoro, L. Altomare, A. Leonardi, M. Tartagni, R. Guerrieri, *A CMOS Chip for Individual Cell Manipulation and Detection*, IEEE Journal of Solid-State Circuits, vol. 38, n. 12, December 2003, pp.2297-2305.
- [52] G. Medoro, N. Manaresi, A. Leonardi, L. Altomare, M. Tartagni, R. Guerrieri, *A Lab-on-a-Chip for Cell Detection and Manipulation*, IEEE Sensors Journal, vol. 3, no. 3, June , 2003.
- [53] Y. Ghallab, W. Badawy, *Sensing methods for dielectrophoresis phenomenon: from bulky instruments to lab-on-a-chip*, IEEE Circuits and Systems Magazine, vol. 4, no. 3, pp. 5-15, 2004
- [54] X-B. Wang, Y. Huang, F. F. Becker, P. R. C. Gascoyne, *A unified theory of dielectrophoresis and travelling wave dielectrophoresis*, J. Phys. D: Appl. Phys., vol. 27, pp. 1571-1574, 1994.

Bibliography

- [55] Y. Huang, X-B. Wang, J. A. Tame, R. Pethig, *Electrokinetic behaviour of colloidal particles in travelling electric fields: studies using yeast cells*, J. Phys. D: Appl. Phys., vol. 26, pp. 1528-1535, 1993.
- [56] M. S. Talary, R. Pethig, *Optical technique for measuring the positive and negative dielectrophoretic behaviour of cells and colloidal suspensions*, IEE Proc.-Sci. Meas. Technol., vol. 14, 5, Sept. 1994.
- [57] N. Manaresi, A. Romani, G. Medoro, L. Altomare, A. Leonardi, M. Tartagni, R. Guerrieri, *A CMOS Chip for Individual Cell Manipulation and Detection*, IEEE ISSCC Dig. Tech. Papers, vol. 46, no. 1, pp. 192-193, 487, Feb. 2003.
- [58] A. Fuchs, N. Manaresi, D. Freida, L. Altomare, C. L. Villiers, G. Medoro, A. Romani, I. Chartier, C. Bory, M. Tartagni, P. N. Marche, F. Chatelain, *A microelectronic chip opens new fields in rare cell population analysis and individual cell biology*, in Proc. of the 7th Int. Conf. on Miniaturized Chemical and Biochemical Analysis Systems (Micro-TAS), October 2003
- [59] G. Medoro, N. Manaresi, A. Romani, M. Tartagni, R. Guerrieri, *A Programmable lab-on-a-chip for individual cell manipulation and detection*, VIII Congresso Nazionale su Sensori e Microsistemi (AISEM), Trento (I), 2003.
- [60] M. Tartagni, A. Romani, G. Medoro, A. Leonardi, L. Altomare, N. Manaresi, R. Guerrieri, *A microelectronic approach for single cell manipulation* VII Congresso Nazionale su Sensori e Microsistemi (AISEM), Bologna (I), 2002
- [61] A. Fuchs, D. Freida, I. Chartier, C. Villiers, G. Medoro, N. Manaresi, A. Romani, L. Altomare, R. Guerrieri, M. Tartagni, *MeDICS: a lab-on-a-chip for cell separation based on dielectrophoresis*, Nanotech 2002, November 2002

- [62] G. Medoro, N. Manaresi, M. Tartagni, L. Altomare, A. Leonardi, R. Guerrieri, *A Lab-on-a-chip for Cell Separation Based on the Moving-Cages Approach*, in Proc. of Eurosensors XVI, Prague, September, 2002.
- [63] G. Medoro, A. Leonardi, L. Altomare, N. Manaresi, M. Tartagni, R. Guerrieri, *A Lab-on-a-chip For Cell Detection And Manipulation*, in Proc. of IEEE Sensors Conference, Jun. 2002.
- [64] S. Mendis, S. Kemeny, B. Pain, C. Staller, Q. Kim, E. Fossum, *CMOS active pixel image sensors for highly integrated imaging systems*, IEEE Journal of Solid State Circuits, vol. 32, pp. 187–197, Feb. 1997.
- [65] S. Mendis, S. Kemeny, E. Fossum, *A 128×128 CMOS active pixel image sensor for highly integrated imaging systems*, in Proc. Electron Devices Meeting, pp: 583-586, 1993.
- [66] M. Rabarot, J. Bablet, M. Ruty, I. Chartier, C. Dubarry, *Thick SU8 Lithography for BioMEMS*, Photonics West, Micromachining and Microfabrication, SPIE conference, San Jose, CA, Jan 2003.
- [67] M. Washitzu, T. B. Jones, K.V.I.S. Kaler, *Higher order dielectrophoretic effects: levitation at field null*, Biochimica et Biophysica Acta, vol. 1158, pp. 40-46, 1993
- [68] N. Manaresi, G. Medoro, M. Tartagni, R. Guerrieri, *Microelectronics meets biology: challenges and opportunities for functional integration in lab-on-a-chip* European Solid State Devices Research Conference - European Solid State Circuits Conference (ESSDERC-ESSCIRC, September 2002, pp. 31-36
- [69] A. La Rosa, L. Lavagno, C. Passerone, *A software development tool-chain for a reconfigurable processor*, in Proc. of the 2002 Int. Conf. on Compilers, Architecture and Synthesis for Embedded Systems, 2002
- [70] F. Campi, R. Canegallo, R. Guerrieri, *IP-reusable 32-bit VLIW Risc Core*, in Proc. of European Solid State Circuits Conference (ESSCIRC), September 2001, pp. 456-459

Bibliography

- [71] M. Rabarot, J. Bablet, M. Ruty, I. Chartier, C. Dubarry, *Thick SU8 lithography for BioMEMS*, in Proc. of SPIE, vol. 4979, pp. 382-393, Micromachining and Microfabrication Process Technology VIII, San Jose, CA, Jan. 2003.
- [72] I. Chartier, C. Bory, A. Fuchs, D. Freida, N. Manaresi, M. Ruty, J. Bablet, K. Gilbert, N. Sarrut, F. Baleras, C. Villiers, L. Fulbert, *Fabrication of hybrid plastic-silicon microfluidic devices for individual cell manipulation by dielectrophoresis*, in Proc. of SPIE, Microfluidics, BioMEMS, and Medical Microsystems II, vol. 5345, pp. 7-16, Dec. 2003
- [73] P. Vulto, N. Glade, L. Altomare, J. Bablet, G. Medoro, A. Leonardi, A. Romani, I. Chartier, N. Manaresi, M. Tartagni, R. Guerrieri, *Dry film resist for fast fluidic prototyping* in Proc. of the 8th Int. Conf. on Miniaturized Chemical and Biochemical Analysis Systems (MicroTAS), October 2004
- [74] N. Manaresi, G. Medoro, M. Abonnenc, V. Auger, P. Vulto, A. Romani, L. Altomare, M. Tartagni, R. Guerrieri, *New perspectives from the wild West of microelectronic biochips*, in Proc. of Design, Automation and Test in Europe, March 2005
- [75] M. Borgatti, L. Altomare, M. Baruffa, E. Fabbri, G. Breveglieri, G. Feriotto, N. Manaresi, G. Medoro, A. Romani, M. Tartagni, R. Gambari, R. Guerrieri, *Separation of white blood cells from erythrocytes on a dielectrophoresis (DEP) based lab-on-a-chip device*, International Journal of Molecular Medicine, vol. 14, 2004, In press
- [76] D. C. Grahame, *The electrical double layer and the theory of electrocapilarity*, Chem. Rev., vol. 41, pp. 441-501, 1947
- [77] A. Hamelin, *Double layer properties at metal electrodes in modern electrochemistry*, vol. 16, Plenum Press, New York, 1985
- [78] I. M. Ritchie, S. Bailey, R. Woods, *The metal-solution interface*, Advances in Colloid and Interface Science, Elsevier, vol. 80, pp. 183-231, 1999

- [79] R. Ricci, *Report on Capacitive Sensing on the MeDICS chip*, ARCES, University of Bologna, 2004
- [80] P. Vulto, N. Glade, L. Altomare, J. Bablet, L. Del Tin, G. Medoro, N. Manaresi, M. Tartagni, R. Guerrieri, *Microfluidic channel fabrication in dry film resist for production and prototyping of hybrid chips*, Lab on a Chip, 2005, pp. 156-162
- [81] D. Derouich-Guergour, C. Villiers, G. Medoro, A. Romani, I. Chartier, C. Bory, M. Tartagni, P. N. Marche, F. Chatelain, R. Guerrieri, *A lab-on-a-chip for cell sorting and manipulation based on dielectrophoresis: effect of beads on cell levitation*, in Proc. of International Meeting on Micro and Nanotechnologies (MINATEC), Sep. 2003
- [82] P. N. Marche, A. Fuchs, D. Freida, I. Chartier, N. Sarrut, C. L. Villiers, D. Derouich-Guergour, G. Medoro, A. Romani, L. Altomare, R. Guerrieri, M. Tartagni, N. Manaresi, *A cell-on-a-chip for cell separation by dielectrophoresis*, Micro et Nanobiotechnologies pour la Médecine et la Chirurgie, May 2004
- [83] A. Romani, N. Manaresi, G. Medoro, R. Guerrieri, M. Tartagni, *Beyond the microscope: embedded detectors for cell biology applications*, to appear in Proc. of International Symposium on Circuits and Systems (ISCAS), 2005
- [84] C. C. Enz, G. Temes, *Circuit techniques for reducing the effects of op-amp imperfections: autozeroing, correlated double sampling and chopper stabilization*, Proc. IEEE, vol.84, no. 11, pp.1584-1614, 1996
- [85] R. Gregorian, G. Temes, *Analog MOS Integrated Circuits for Signal Processing*, John Wiley & Sons, 1986
- [86] J. G. Proakis, *Digital Communications*, McGraw-Hill, 2001
- [87] H.-S. Wong, *Technology and device scaling considerations for CMOS imagers*, IEEE Trans. Electron Devices, vol. 43, no. 12, pp. 2131-2141

Bibliography

- [88] M. J. Madou, R. Cubicciotti, *Scaling issues in chemical and biological sensors*, Proc. IEEE, vol. 91, no. 6, pp. 830-838, June 2003
- [89] M. Rubboli, *Progettazione di un ambiente software per l'isolamento di cellule in un lab-on-a-chip*, MD Thesis, University of Bologna, 2004
- [90] R. Ricci, *Caratterizzazione sperimentale di schiere di sensori per il rilevamento di particelle biologiche*, MD Thesis, University of Bologna, 2004
- [91] L. Marzocchi, *Sviluppo e validazione sperimentale di algoritmi per schiere di biosensori*, MD Thesis, University of Bologna, October 2003.
- [92] S. Ronconi, *Progetto di una scheda di test per dispositivo lab-on-a-chip*, MD Thesis, University of Bologna, July 2002.